

The Thermodynamic Limit of Indoor Photovoltaics



Swansea University
Prifysgol Abertawe

Maura Eileen Fitzsimons

Department of Physics

Swansea University

Submitted to Swansea University in fulfilment of the
requirements for the degree of

Master of Science by Research

2023

Abstract

Indoor Photovoltaic development stands between low-power devices such as the Internet of Things and their potential widespread roll out. Semiconductor material choice, of the active layer, has the potential to enhance indoor photovoltaic performance. To begin the early-stage research of indoor photovoltaic material choice, the thermodynamic compatibility of the material systems with the incident illumination spectrum was evaluated. While organic semiconductors present many advantages in the photovoltaic industry due to their low di-electric constants and cheap processibility over their respective inorganic counterparts, a standout advantage for use of organic semiconductors in indoor photovoltaic applications is their wider effective energy gaps. By adopting the principle of detailed balance and applying Shockley-Queisser limit calculations to pre-existing external quantum efficiency data and two chosen indoor lighting spectra, promising material systems were identified prior to fabrication and optimisation. As a result, predictions of two high-efficiency material systems were made and, in addition to a model system, were characterised in the remainder of this Thesis.


In addition to the Shockley-Queisser analysis of existing material systems for characterisation under simulated indoor illumination conditions, theoretical limits, including radiative (Shockley-Queisser) and non-radiative (empirical models produced from the literature), were calculated for the two chosen light emitting diode radiation sources. From this analysis, it was evident that the optimal energy gap for an indoor photovoltaic system under these conditions was much wider than originally calculated for the scenario subject to solar illumination (1.14 eV). The optimal bandgap for the chosen light emitting diode source of 4000 K was equivalent to an effective energy gap of 1.89 eV, significantly higher than the energy gap that devices have been optimised towards historically, potentially capable of approximately 40% power conversion efficiency including non-radiative loss simulations at illuminances as low as 50 lux. Finally leading onto answering one of the aims of this Thesis; what is more important, thermodynamic compatibility or outperforming charge transport properties? Firstly, it can be considered that the EH-IDTBR and BTP-eC9 based devices are thermodynamically compatible and of above average charge transport properties. Therefore, with improvements to the short-circuit current, the thermodynamic compatibility could carry more weight in the optimisation of indoor organic photovoltaic devices.

An additional investigation carried out through this Thesis is into the effect of shunt resistance on indoor organic photovoltaics. When observing both EH-IDTBR based systems, their varying shunt resistances (recorded via a dark characterisation process) present themselves significantly in the open-circuit voltage and fill factor dependence on light intensity. By performing these measurements, the incident illuminance at which the devices began to quickly deplete in performance was evaluated, therefore implying their importance.

In summary, considering both the radiative and empirical non-radiative limits, the work presented in this Thesis provides valuable insight into the optimal effective energy gap for photovoltaic devices under two chosen model indoor illumination spectra. In addition, important evidence of the significant effect of shunt resistance on indoor photovoltaic device performance at low light intensities is presented, with conclusions that could make device selection more efficient for test under indoor characterisation. Finally, the importance of thermodynamic compatibility was emphasised. In combination, all of the aforementioned conclusions could potentially be used to aid the development of indoor organic photovoltaics.


Declarations

This work has not previously been accepted in substance for any degree and is not being concurrently submitted in candidature for any degree.

Signed..... 


Date.....03/07/2023.....

This thesis is the result of my own investigations, except where otherwise stated. Other sources are acknowledged by footnotes giving explicit references. A bibliography is appended.

Signed..... 


Date...03/07/2023.....

I hereby give consent for my thesis, if accepted, to be available for photocopying and for inter-library loan, and for the title and summary to be made available to outside organisations.

Signed..... 

Date.....03/07/2023.....

The University's ethical procedures have been followed and, where appropriate, that ethical approval has been granted.

Signed..... 

Date..... 03/07/2023.....

Table of Contents

| | |
|--|------------|
| List of Figures | vii |
| List of Tables | xi |
| List of Acronyms and Symbols | xii |
| 1 Introduction | 1 |
| 1.1 Solid State Semiconductor Fundamentals..... | 8 |
| 1.2 Organic Photovoltaic Cells: The Working Principle..... | 13 |
| 1.2.1 Photocurrent Generation | 14 |
| 1.2.2 Organic Photovoltaic Cells: Structure..... | 17 |
| 1.2.3 Power Conversion Efficiency: A Figure of Merit..... | 21 |
| 1.3 Characterisation of Solar Cells..... | 22 |
| 1.3.1 Current Voltage Characteristics | 22 |
| 1.4 PV Cells: From Outdoor to Indoor..... | 25 |
| 1.4.1 IPV Characterisation Challenges | 25 |
| 1.4.2 Indoor Material Development | 27 |
| 1.4.3 Advantages of Organic Indoor Photovoltaics | 27 |
| 1.4.4 Importance of Indoor Photovoltaic Development..... | 29 |
| 1.5 Summary | 32 |
| 1.6 Aims of this Thesis | 32 |
| 2 Theoretical Thermodynamic Limit of Solar Cells | 34 |
| 2.1 Introduction..... | 34 |
| 2.2 The Principle of Detailed Balance | 38 |
| 2.3 The Shockley-Queisser Limit | 38 |
| 2.3.1 Conditions | 40 |
| 2.3.2 AM1.5 G Solar Standard..... | 43 |
| 2.4 Shockley-Queisser Limit Calculation | 46 |
| 2.4.1 Theoretical Upper Limit: Power Conversion Efficiency | 50 |
| 2.4.2 Theoretically Optimal Energy Bandgap..... | 52 |
| 2.4.3 Current High-Performance Organic Materials | 54 |
| 2.5 Non-Radiative Recombination Contributions..... | 55 |

TABLE OF CONTENTS

| | |
|---|------------|
| 2.6 Summary | 59 |
| 3 Indoor Photovoltaic Thermodynamic Theoretical Limit | 61 |
| 3.1 Introduction..... | 61 |
| 3.2 Indoor Light Sources..... | 63 |
| 3.2.1 Indoor Light Source Standard | 64 |
| 3.2.2 Indoor Light Source Metrics | 67 |
| 3.3 Intensity dependence on Leakage Current | 70 |
| 3.4 Shockley-Queisser Limit: Indoors | 73 |
| 3.4.1 Indoor Theoretical Upper Limit: Power Conversion Efficiency | 73 |
| 3.4.2 Indoor Theoretical Optimal Energy Bandgap | 76 |
| 3.4.3 Chosen Indoor Organic Active Layers..... | 78 |
| 3.5 Summary | 81 |
| 4 Experimental Methodology and Results | 83 |
| 4.1 Solar Cell Characterisation | 83 |
| 4.1.1 Solar Cell Characterisation Set-up..... | 84 |
| 4.1.2 Shunt Resistance Results..... | 84 |
| 4.2 Indoor Photovoltaic Characterisation..... | 86 |
| 4.2.1 Chosen Light Source | 86 |
| 4.2.2 Indoor Photovoltaic Characterisation Set-up | 87 |
| 4.2.3 Intensity Dependence Results and Discussion | 88 |
| 5 Conclusion..... | 98 |
| References..... | 107 |
| Appendix..... | 102 |
| Device Fabrication | 102 |
| A.1 Materials..... | 102 |
| A.2 Substrate Preparation..... | 104 |
| A.3 Electron/Hole Transport Layer Deposition | 104 |
| A.4 Active Layer and Top Electrode Deposition..... | 104 |

Acknowledgements

The past 18 months of my life have tested me more than I previously thought I could ever endure. The people in my life who have helped me reach where I am today despite this have proven to be invaluable assets to not only my career but my life. Therefore, in honour of their contributions, I would like to acknowledge them personally.

I would firstly like to take the opportunity to thank my supervisors, Prof. Paul Meredith, and Dr Ardalan Armin. Without their support for the SêrSAM research group and my admittance onto this course, I would never have achieved what I have across this course. In addition to this, I would like to place a special emphasis on the way Dr Ardalan Armin has supported me over the course of my masters. My life has taken a few turns I never expected prior to applying for this course and you have been there to acknowledge my hardship and difficulty in a way that I did not expect, and in a way I could never fully pay back. Without your support I categorically would not have felt comfortable in an academic environment the way that I have, so thank you.

Secondly, I would like to thank all of the researchers and PhD students who have helped me through the experimental process and editing of my thesis. Dr Nasim Zarrabi and Dr Stefan Zeiske, your help in the optoelectronics laboratory will forever be appreciated. In addition to this, Dr Nasim Zarrabi and Dr Yong Ryun Kim, I acknowledge that without your help in the cleanroom I would never have learned how to produce my own OPV device samples – which turned out to be the most enjoyable part of my masters degree. Dr Oskar Sandberg, I thank you for your consistently important help with my theoretical understanding. Finally, I would like to thank Dr Nasim Zarrabi, Dr Stefan Zeiske, Dr Greg Burwell and Dr Oskar Sandberg as a collective, your constructive criticism of my thesis has been priceless.

Rhian Jones and Heather Evans, thank you for welcoming me into the group and the help you continue to provide me with. You create fun moments for the research group which I will not forget.

Lastly, I would like to thank my friends and family. To my closest friend Kathryn, you have been an amazing emotional support to me over the past decade that we have known each other but especially in the past 18 months. You have comforted the confidence I have in my capabilities when it felt like an impossible task, you are one of the reasons I have produced the work I have today, and I am adamant that we will have great lives alongside one and other. My most profound gratitude, however, goes to my parents, sister, and brother-in-law. In a world where I didn't have your support, I am genuinely not sure what I would be doing as you have all kept me grounded and focused, which in the case at hand, where you have zero physics knowledge to provide me with, was an irreplaceable contribution. Finally, to my nephew Leoch, I know you are only 19 months old, but your smile has made me feel at home even on the other end of the phone 225 miles away.

List of Figures

| | | |
|------------|--|----|
| 1.1 | Comparative diagram of the band structure in insulators, semiconductors, and conductors at a temperature of 1000 K | 8 |
| 1.2 | A schematic of the four operational mechanisms of photocurrent generation in a bulk heterojunction OSC where: 1. Exciton generation – a photon is absorbed, exciting an electron from the HOMO to the LUMO 2. Exciton diffusion – the exciton travels to the donor/acceptor interface 3. Exciton dissociation – the electron moves to the acceptor’s LUMO and into a charge transfer (CT) state 4. Free charge collection at the electrodes. | 14 |
| 1.3 | Schematic of four different OSC active layer morphologies, where blue and red indicate donor and acceptor respectively in (a) A singular donor layer (b) A donor-acceptor bilayer (c) The optimal morphology of the active layer (comb structure) and (d) The bulk heterojunction (BHJ) structure. | 17 |
| 1.4 | A schematic of an organic photovoltaic device with a BHJ structure. Orientation is implied by light source positioning. | 18 |
| 1.5 | A typical J-V characteristic of a PM6:Y6 device. The solid black line is representative of the data measured under AM1.5 G illumination conditions and the red symbol line is data measured in dark conditions. The blue dashed line shows the maximum power output curve. Important parameters J_{SC} , V_{OC} , FF and PCE are listed also. | 21 |
| 1.6 | A circuit schematic of a typical PV cell, showing direction of current flow and applicable resistances described in equation 1.31. | 22 |
| 1.7 | Schematic examples of semiconducting donor and acceptor molecules (a) PBDB-T (PCE-12) an electron donor (b) PBDB-T-2F (PM6) an electron donor (c) EH-IDTBR an electron non-fullerene acceptor (NFA) and (d) BTP-eC9 an electron NFA. | 25 |
| 1.8 | Power consumption scale of varying IoT communication protocols. Power consumption ranges are indicated by red boxes and red lines are exact values. The translucent green box highlights approximate indoor energy harvesting capabilities. | 28 |

LIST OF FIGURES

- 2.1** PCE timeline of novel solar cells from 2007 through to 2021 compared to the SQ limit (dashed line) of 33.7% at $E_g=1.14$ eV. Material systems are presented with the line and scatter graph key with crystalline silicon (c-Si), perovskite and organic in grey, red, and blue respectively. Data was collected from solar cell efficiency tables from 2001-2023. 33
- 2.2** AM1.5 G solar spectrum as a function of photon energy. The top panel displays the ratio of photon flux with energy high enough ($E \geq E_g$) to be absorbed by silicon (Si) and the following respective panels present the same ratio for organic semiconducting material systems PM6:BTP-eC9 and PM6:EH-IDTBR. 41
- 2.3** SQ upper limit of **(a)** J_{SC} and V_{OC} and **(b)** dark saturation current density considering only radiative recombination (J_0^{Rad}) as a function of energy bandgap. 46
- 2.4** SQ PCE as a function of photon energy. Different simulated values of EQE_{PV} are identifiable by varying coloured solid lines. Three materials systems' bandgaps are labelled on the plot showing their upper theoretical limit; vertical dashed lines therefore represent material energy gaps for reference. 48
- 2.5** Light intensity dependence on photocurrent density. The different coloured solid lines represent varying values of ζ displayed in the key. Generation rate is proportional to light intensity and is normalised to the generation rate at AM1.5 G; therefore, $G = 1$ is the generation rate at AM1.5 G. Dashed coloured lines correspond to an estimation of the G at which photocurrent density is affected by ζ 55
- 3.1** The comparison of three normalised emission photon flux spectra as a function of photon energy, including: AM1.5 G (left axis, black), 2700 K (right axis, light blue) and 4000 K LED (right axis, dark blue). 62
- 3.2** A circuit schematic of a typical PV cell, showing direction of current flow and applicable resistances. 67
- 3.3** Intensity dependence with varying R_{sh} on **(a)** V_{OC} and **(b)** FF . The dashed lines from left to right indicate irradiance values of a 4000 K LED at 50 lux and 1000 lux as well as the irradiance

LIST OF FIGURES

value of AM1.5 G. Varying R_{sh} is differentiated by the colour of the solid lines described in the key. 68

3.4 Non-radiative voltage losses as a function of bandgap energy. The two dashed lines, black and blue, are representative of two non-radiative models referenced in this Thesis, an optimistic and lower limit model respectively. The translucent, red pentagons are collated literature data reported by *Ullbrich et al.*, while the red circle scatter and line data represents the lower limit empirical model created for this Thesis from the *Ullbrich et al.* reported data. 71

3.5 Simulated open circuit voltage as a function of bandgap energy for four models: radiative, optimistic, lower limit and the empirical fit from Benduhn et al. [1] represented by black, red, blue, and green solid lines respectively. Simulated using the LED spectra of (a) 2700 K and (b) 4000 K. 72

3.6 Simulated PCE as a function of optical energy bandgap for LEDs of (a) 2700 K and (b) 4000 K. 73

3.7 An analysis of three main parameters in OPV using a 2700 K LED 500 lux spectrum. The first three panels in order analyse J_{sc} , V_{oc} and PCE respectively. The final panel is a key for the data presented in the other three panels. 75

3.8 A schematic representation of the energy levels (eV) of three OPV material systems chosen for this work. From left to right: PBDB-T:EH-IDTBR, PM6:EH-IDTBR and PM6:BTP-eC9. The energy bandgap of all three materials systems are 1.40 eV, 1.60 eV and 1.40 eV respectively. . . 77

4.1 J - V characteristic (with no excess illumination) of PBDB-T:EH-IDTBR device of cell area 0.9482cm^2 . Experimental data and a linear fit are represented by the black circles and red solid line respectively. 81

4.2 Intensity-dependent data of the PM6:EH-IDTBR material system PV device sample, with varying sizes pixels of 0.04, 0.1416, 0.3894, and 0.9482cm^2 depicted by grey squares, pink triangles, blue stars and green diamonds respectively. Solid orange circles show the optimistic radiative detailed balance limit and the hollow orange circles show the Bendhur lower theoretical limit. The intensity axis is log scaled and the vertical dashed lines from left to right respectively showcase illuminance values of 50, 500, 1000, and 2000 lux. Various parameters are displayed (a)

LIST OF FIGURES

J_{sc} (b) V_{oc} (c) FF and (d) PCE. In panel (b), two dashed lines, black and blue, signify slopes of ideality factor (n) 1 and 2 respectively. 85

4.3 Intensity-dependent data of the PBDB-T:EH-IDTBR material system PV device sample, with varying sizes pixels of 0.04, 0.1416, 0.3894, and 0.9482 cm² depicted by grey squares, pink triangles, blue stars and green diamonds respectively. Solid orange circles show the optimistic radiative detailed balance limit and the hollow orange circles show the Bendhur lower theoretical limit. The intensity axis is log scaled and the vertical dashed lines from left to right respectively showcase illuminance values of 50, 500, 1000, and 2000 lux. Various parameters are displayed (a) J_{sc} (b) V_{oc} (c) FF and (d) PCE. In panel (b), two dashed lines, black and blue, signify slopes of ideality factor (n) 1 and 2 respectively. 89

4.4 Intensity-dependent data of the PM6:BTP-eC9 material system PV device, pixel size 0.04 cm² depicted by grey squares. Solid orange circles show the optimistic radiative detailed balance limit and the hollow orange circles show the Bendhur lower theoretical limit. The intensity axis is log scaled and the vertical dashed lines from left to right respectively showcase illuminance values of 50, 500, 1000, and 2000 lux. Various parameters are displayed (a) J_{sc} (b) V_{oc} (c) FF and (d) PCE. 92

List of Tables

| | | |
|----------|---|----|
| 1 | The illuminance values of the three light spectra used in the focus of this research to 3 significant figures. | 64 |
| 1 | The required illuminances of different indoor working situations as determined by the European Union (NEN-EN 12464-1:2011 en). | 65 |
| 3 | The shunt resistances of two material systems, PBDB-T:EH-IDTBR and PM6:EH-IDTBR, with device sizes 0.04, 0.1416, 0.3894 and 0.9482 cm ² | 81 |

List of Acronyms and Symbols

| | |
|---------------------|---|
| α | Shockley-Read-Hall recombination constant |
| AM0 | Air mass zero |
| AM1.5 D | Air mass 1.5 direct |
| AM1.5 G | Air mass 1.5 global |
| β | Bi-molecular recombination constant |
| β_L | Langevin recombination constant |
| BHJ | Bulk heterojunction |
| c-Si | Crystalline Silicon |
| CIE | International commission on illumination |
| CO ₂ | Carbon dioxide |
| CO _{2e} | Equivalent carbon dioxide |
| CS | Charge separated |
| CT | Charge transfer |
| DUT | Device under test |
| δ | Auger recombination constant |
| E | Electronic State |
| E _c | Conduction band electronic state |
| E _F | Fermi energy |
| E _g | Bandgap energy |
| E _v | Valence band electronic state |
| ϵ | Semiconductor material permittivity |
| ϵ_0 | Free space permittivity |
| EQE _{pv} | Photovoltaic external quantum efficiency |
| η_{abs} | Absorption efficiency |
| FF | Fill factor |
| $f(E)$ | Fermi-Dirac distribution |
| G | Generation rate |
| γ_{abs} | Number of photons absorbed |
| γ_{em} | Number of photons emitted |
| $\gamma_{incident}$ | Number of photons incident |
| $\gamma_{reflect}$ | Number of photons reflected |
| γ_{trans} | Number of photons transmitted |
| $g(E)$ | Density of states |
| $g_c(E)$ | Density of states in conduction band |

LIST OF ACRONYMS AND SYMBOLS

| | |
|-------------|--|
| $g_v(E)$ | Density of states in valence band |
| HOMO | Highest occupied molecular orbital |
| I_{SC} | Short-circuit current |
| I_{Total} | Total current |
| ∞ | Infinity |
| IoT | Internet of Things |
| IOPV | Indoor organic photovoltaic |
| IPV | Indoor photovoltaic |
| IQE_{PV} | Photovoltaic internal quantum efficiency |
| ITO | Indium tin oxide |
| I-V | Current-voltage |
| J_d | Diode current density |
| $J_{G,L}$ | Total light generated current density |
| J_{MP} | Maximum power point current density |
| J_{ph} | Photocurrent density |
| J_R^{Rad} | Radiative recombination current density |
| J_{SC} | Short-circuit current density |
| J_{sh} | Shunt current density |
| J_{Total} | Total current density |
| J_0 | Dark saturation current density |
| J_0^{rad} | Radiative dark saturation current density |
| J-V | Current density-voltage |
| k_B | Boltzmann's constant |
| L_0 | Maximum spectral luminous efficacy |
| λ | Wavelength |
| LED | Light emitting diode |
| LUMO | Lowest unoccupied molecular orbital |
| m_e^* | Effective mass of electron |
| m_h^* | Effective mass of hole |
| μ_n | Electron mobility |
| μ_p | Hole mobility |
| n | Ideality factor |
| N_c | Conduction band edge effective density of states |
| n_e | Number of electrons |
| n_h | Number of holes |
| N_v | Valence band edge effective density of states |
| NFA | Non-fullerene acceptor |

LIST OF ACRONYMS AND SYMBOLS

| | |
|------------------------------|--|
| NIR | Near infrared region |
| NPL | National Physics Laboratory |
| OPV | Organic Photovoltaic |
| OSC | Organic solar cell |
| P_{input} | Incident light power |
| P_{MAX} | Maximum power |
| P_{output} | Maximal operational electrical power output |
| $P_{\text{source}}(\lambda)$ | Radiation output power spectrum |
| Φ_{Ph} | Light source photon flux density |
| Φ_{BB} | Blackbody photon flux density |
| PCE | Power conversion efficiency |
| π | Pi |
| PV | Photovoltaic |
| q | Elementary charge |
| R | Recombination rate |
| R_{bi} | Bi-molecular recombination rate |
| R_{S} | Series resistance |
| R_{sh} | Shunt resistance |
| $R_{\text{sh,critical}}$ | Critical shunt resistance |
| Si | Silicon |
| SI | International system of units |
| SQ | Shockley-Queisser |
| T | Temperature |
| t_{ext} | Extraction time |
| TCE | Transparent conductive electrode |
| \hbar | Reduced Planck's constant |
| V_{MP} | Maximum power point voltage |
| V_{OC} | Open-circuit voltage |
| $V_{\text{OC,loss}}$ | Open-circuit voltage loss |
| $V_{\text{OC,rad}}$ | Radiative open-circuit voltage |
| $V_{\text{OC,nr}}$ | Non-radiative open-circuit voltage |
| V_{S} | Series resistance voltage |
| $V(\lambda)$ | Standard relative eye sensitivity |
| XSC | Excitonic solar cell |
| ζ | Langevin recombination constant reduction factor |
| ζ_{CT} | Charge transfer state bi-molecular recombination |
| ζ_{geo} | Interface bi-molecular recombination |

Chapter 1

Introduction

Decelerating the effects of global warming is one of the most critical challenges of the 21st century [2]. For that reason, an ideal future would see a reduction in human contribution of carbon emissions to net zero with improved environmental stability and security. Challenging the move toward sustainability, global energy demand is increasing every day due to the nature of our societal needs; therefore, moving toward a reliance on renewable energy resources versus fossil fuels has promisingly positive socio-economic benefits [3, 4, 5]. Presently, the global energy demand vastly outweighs its sustainable supply [6], causing significant energy instability. Many countries in the first world rely on importing their energy sources, which are both expensive and non-renewable. The development of local sustainable energy production will not only improve affordability, but also energy security within these nations. The introduction of increased sustainable energy resources will reduce fossil fuel consumption, leading to cleaner air and an improved quality of life with a reduction in health-related issues [3, 4, 5]. Therefore, increasing the efficiency of our energy harvesting capabilities is paramount to matching the energy consumption demand around the world in addition to moving towards reducing our dependence on non-renewable resources.

Typically, the building sector is responsible for half of all energy consumption. This is partly due to inefficiencies in both the glass windows (which affect lighting levels) and

1. INTRODUCTION

temperature control [7, 8, 9]. Poor efficiency in these two environmentally impacting factors result in a need for supplementation, which has a high energetic cost. If the architecture considered natural lighting and climate as a priority, energy efficient buildings would result in a significant reduction in energy consumption. However, even improving the energy efficiency of our existing architecture with the addition of renewable energy resources, such as solar cells, introduces a convenient solution.

Worldwide energy demands have increased considerably from 8.6 to 13.1 billion tonnes of oil equivalent from 1995-2015 [10]. The sustainability of current human society rests on several fundamental supports, one of which being renewable energy production. With the significant energy demand increase, there have been continuous attempts to subsidise via renewable resources, with solar energy sitting at the forefront [4]. No moving parts, no emissions, silent in operation, not visually intrusive to architecture [11], powerful, and an accessible energy source, solar energy has been termed the most efficient route to increasing the move towards a renewable energy future [7, 8]. Adopting harvesting of light energy using photovoltaics on an industrial scale is already in early integration, however due to the start-up cost of this form of energy harvesting, not all of society can afford to implement these systems (solar panels) into their homes. High costs can often be associated with the costly purifying process of silicon, often accounting for 50% of the overall cost [12]. Energy classed as clean and married with a rigorous development history; solar cell manufacturing is consistently declining in cost as well as improving in efficiency. These improvements can often be borne out of increased material research.

1. INTRODUCTION

Expense and efficiency are important contributors to the rollout of sustainable energy resources; however, environmental cost is an equally pressing issue. To decrease the human contribution to global warming, the reduction of greenhouse gas emissions is a necessity. Therefore, determining the environmental impact of varying renewable resources is just as crucial as making the switch out from non-renewables. With fossil energy sources producing equivalent carbon dioxide (CO₂e) emissions upwards of 400-500 gCO₂e/kWh, renewable values are significantly lower while simultaneously not negligible. Silicon modules vary largely dependent on location and technology however, their emissions sit roughly around 80 gCO₂e/kWh. A recent study found organic photovoltaics (OPV) on the range of 3-15 gCO₂e/kWh [13], strongly competing with wind and hydro energy and an impressively low emission compared to that of current commercial solar harvesting systems [2]. Evaluating the PV industry further, when considering the growth of the industry, the energy production and carbon savings made can become outweighed from the equivalent used in the production process. To analyse this, one must consider both the growth rate and embodied energy (carbon increases), when the embodied energy increases, so does the cannibalisation of the energy and carbon compensation. Logically, the solar PV system must grow at a rate slower than the inverse of its CO₂ payback time. For Si-based solar cells, energy savings are negated by the fabrication of the subsequent wave of solar PV systems; although contributing in a similar fashion, OPVs do this at a significantly reduced rate and so can afford a much needed faster growing industry. Conclusions above support OPV as a considerable improvement on the environmental impact of other energy sources even when compared with current widely commercialised photovoltaic systems.

1. INTRODUCTION

In addition to their relatively low embodied energy, in an extensive life cycle analysis of PV cells, *Krebs-Moberg et al.* [14] systematically examined the environmental performance of the primary materials: Si, OPV, and perovskite. Utilising a comprehensive 30-year model that accounted for the entire lifecycle, including efficiency and degradation considerations, the study observed that monocrystalline silicon (m-Si) devices resulted in endpoint impacts (human health, ecosystem damage, and resource availability) ten times larger than those associated with thin-film panels in landfilling scenarios. Findings revealed that m-Si panels exhibited a considerable environmental impact compared to the other two PV material types, with OPVs routinely demonstrating the lowest impact across all assessment categories and averaging less than 40% of the impact corresponding to m-Si panels. Within the m-Si panel category, the production of silicon wafers to electrical-grade standards emerged as the leading contributor to environmental degradation due to energy-intensive and moderately toxic processes. The indispensability of Si wafers in the design of Si PV systems complicates the mitigation of environmental impact associated with their production. When considering environmental impact mitigation through recycling scenarios, m-Si modules showed the most significant benefit from waste recycling, with an average reduction of 15% in each impact category. However, the most substantial reductions across all three photovoltaic module types were achieved through the recovery and reuse of panel materials. Therefore, even when m-Si panels underwent recycling, both thin-film panels consistently demonstrated lower environmental burdens when compared. This analysis emphasises the importance of considering, not only the immediate impact, but also the long-term consequences when evaluating the sustainability of PV technologies.

1. INTRODUCTION

Over and above their impressive life cycle analysis scores, OPV cells present several advantages over their presently out-performing inorganic semiconducting counterparts. Advantages of OPVs can be characterised under three main categories: financial cost, ease and environmental impact of the manufacturing process and application suitability.

Financially, OPV demonstrates a significant advantage with low initial cost; organic solar cells are being developed to produce comparable efficiencies to their inorganic counterparts while simultaneously employing their innate low manufacturing costs; costs as a prediction for mass production which is not currently the case at research and development level fabrication. This comes in addition to the dramatically shorter payback times for industry as well as the individual consumer. Energy payback time is defined as the time passed for the cell to produce equal energy to what was used to produce the cell originally. It has been reported that the energy payback time comparison between crystalline silicon and OPV shows OPV cells have an energy payback time 83.3% shorter than crystalline silicon cells [15]. Therefore, directly influencing their environmental impact. In addition to the low environmental impact of OPV manufacturing and operations, the use of state-of-the-art tools allows the continuous processing of OPV modules through the primary mechanisms of vacuum coating and solution processing. This facilitates the rapid coating of large areas inexpensively [16], creating the potential to class OPV as the most cost-effective source of electricity in the world [2]. Due to the affordability of OPVs, they have the promise to create affordable opportunities for new applications away from solar energy harvesting.

1. INTRODUCTION

When also considering their bandgap tunability, a wide range of light energy harvesting applications to be explored. Finally, their semitransparency, low weight and flexibility make them attractive for new-market application opportunities (e.g., wearable photovoltaics) allowing for easy integration into pre-existing products on the market. Despite their many promising advantages, OPVs have remained undesirable compared to their inorganic counterparts for solar energy harvesting due to presently inferior stability and scalability. Complimenting the existing implementation of Si PVs in the solar energy harvesting market, OPVs have the opportunity to dominate new markets with different requirements. One example is the promise of OPV bandgap tunability utilisation in the developing indoor photovoltaic market.

The integration of photovoltaics harvesting ambient light energy of the indoor environment to produce energy for low power devices presents an intuitive solution to an issue of maintenance and costly battery power where energy requirements can impede the progress and rollout of life improving technology. For example, originating in 1999, the Internet of Things (IoT) was developed where Kevin Ashton used it in the context of supply chain management. In the present day, live devices exist in the billions. IoT is described as computer sensing information without human intervention; appliances are connected by a network and work together to provide ideal service as opposed to separate entities working in conjunction [6]. The power required to sustain and run billions of embedded IoT devices is the biggest hurdle that IoT currently faces. Battery power relies on recharging or replacement, causing either power outage or a costly maintenance routine. For healthcare

1. INTRODUCTION

applications, this could be vital to someone's safety; therefore, device energy supply needs to be stable and consistent. In buildings such as hospitals, airports, factories, offices, etc., it is common for lighting – usually light emitting diode (LED) – to be powered for 24 hours per day. These are ideal environments for the harvesting of ambient light by indoor photovoltaic (IPV) devices to be converted into electrical energy. Utilising this form of energy recycling, IoT has the potential to become partially or wholly self-sustaining [17]. The implementation of IPV devices integrated into daily life would aim to solve issues of inconvenience surrounding battery expense and maintenance. Therefore, IPV will likely not alleviate global warming to a large extent. Despite indoor LEDs having a photon flux on at least 2-3 orders of magnitude smaller than that provided by the sun, IPVs can produce microwatt to milliwatt-class power [18]. This is sufficient to supply energy to background devices such as fire alarms, sensors, or the rapidly growing IoT [19, 20]. Therefore, photovoltaic support and optimisation in this area is required to prevent threats to the future development of IoT [21]. Despite their relatively lacking efficiencies in solar energy harvesting, OPV presents possible advantages over its inorganic counterparts in IPV development. IPVs harvest energy from indoor lighting; these are often light emitting diodes (LEDs) in modern buildings. In consideration of the typical indoor environment where these harvesters may operate, examples of applicable LED spectra temperatures are 2700 K and 4500 K, a warmer and cooler white light respectively. Characteristically these LEDs have narrower peaks in intensity at the shorter wavelength region of the spectrum; therefore, their inability to absorb broadly across the solar spectrum – such as the NIR region due to their wider energy gaps – does not create an obstacle for indoor applications.

1. INTRODUCTION

Wider energy gap organic materials, once ignored for their incompatibility with the solar spectrum, are a possible solution to cheap indoor light energy harvesting for potential self-sustaining devices.

1.1 Solid State Semiconductor Fundamentals

Solid-state devices are defined as electronic devices made entirely or largely of semiconductors, dielectrics, and metals. Most of the semiconductors are based on solid crystalline materials, where atoms are fixed in place with the lowest kinetic energy of the four states of matter. As a result of the closely fixed atoms in a (many body) crystalline solid, the energy levels form energy bands (groups of many electronic states) due to the overlapping of electron orbitals with neighbouring atoms. The valence band is the highest energy occupied band, with electrons forming covalent bonds between atoms, while the conduction band is the lowest energy unoccupied band; sitting between the bands no electronic states can exist, namely the energy bandgap which is a consequence of the periodicity of the lattice. A smaller bandgap requires less energy to excite an electron from the valence to the conduction band; therefore, a solid material's energy bandgap is an indicator of conductivity. For conductors, the valence and conduction band overlap; in contrast the two bands are separated by a considerable energy bandgap in insulators. Consequently, negatively charged electrons can travel between the bands in conductors but not in insulators, resulting in the conductivity or lack thereof respectively.

1. INTRODUCTION

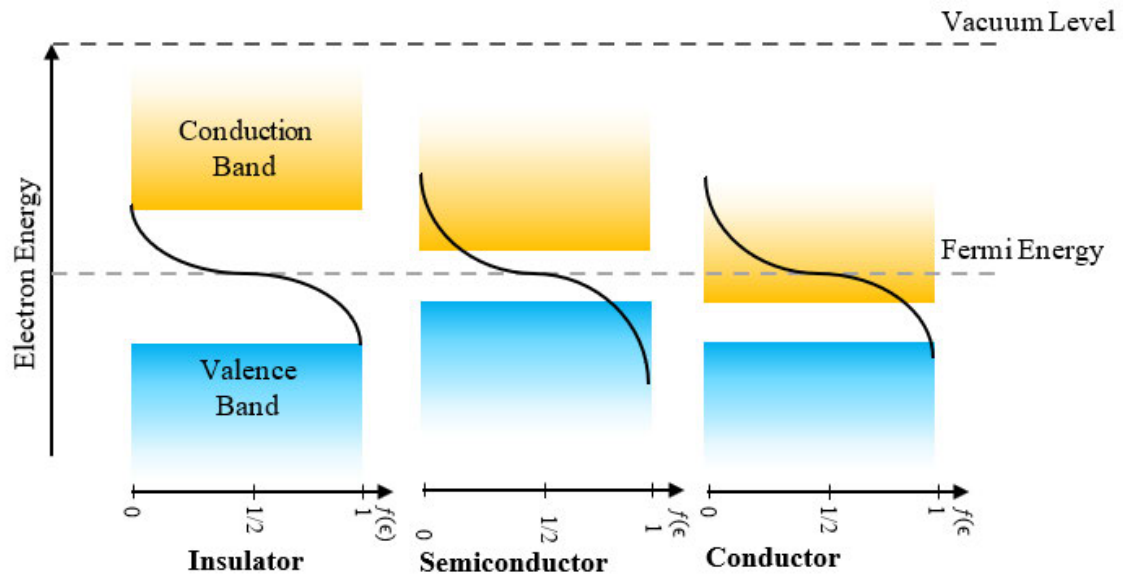


Figure 2.1: Comparative diagram of the band structure in insulators, semiconductors, and conductors at a temperature of 1000 K.

In contrast to conductors, semiconductor's conduction and valence bands do not overlap, producing an energy bandgap. However, the energy bandgap of a semiconductor is significantly smaller than an insulator, allowing the electrons to excite from the valence to the conduction band if supplied with sufficient energy, thermally or optically. If an electron is excited to the conduction band, it leaves behind an empty space, or respective positively charged hole in the valence band; semiconductors' current can therefore be described by the flow of negatively charged electrons in the conduction band or their respective positively charged holes in the valence band.

The Fermi-Dirac distribution is a fundamental concept in the field of semiconductor physics, providing a statistical description of the distribution of electrons in a material at thermodynamic equilibrium. It plays a crucial role in understanding the behaviour of charge

1. INTRODUCTION

carriers, such as electrons and holes, in semiconductors [22]. Therefore, the Fermi-Dirac distribution function ($f(E)$) gives the probability that an electron occupies an electronic state of E ,

$$f(E) = \frac{1}{1 + \exp\left(\frac{E - E_F}{k_B T}\right)}, \quad 1.11$$

where k_B is the Boltzmann's constant, T is temperature in kelvin (K) and E_F is the Fermi level, corresponding to the energy where the probability of being occupied is equal to one half. Figure 1.1 shows the Fermi levels and Fermi-Dirac distribution function associated with each of the three types of solids. At zero temperature ($T = 0$ K), the valence band is fully occupied, and the conduction band is empty – meaning that all electrons are used in forming the covalent bonds. When the electrons cannot move it results in indiscernible conductivity. For an efficient conductor, such as a metal, however, the Fermi energy sits within the conduction band and therefore, even at zero temperature the conduction band is only partially full; this allows electrical current to be conducted due to the freely moving electrons. For semiconductors, the Fermi energy sits within the bandgap, however this bandgap is considerably smaller than that of the insulator. Consequently, at room temperature there is a finite chance of electrons occupying the conduction band. In general, the higher the temperature and the smaller the energy gap, the higher the chance for an electron to occupy the conduction band will be. This is because of the increased probability for electrons to get thermally excited between bands (equilibrium condition). Another way to increase the electron occupation is through photoexcitation or applying voltage (non-

1. INTRODUCTION

equilibrium condition). It is important to be able to calculate the number of electrons and holes in each band.

The number of electrons in the conduction band and holes in the valence band depends on the number of available states as well as the probability distributed function for a given Fermi energy. The density of states ($g(E)$) of electrons in the conduction band and holes in the valence band for a three-dimensional semiconductor can be described by,

$$g_c(E) = \frac{1}{2\pi^2} \left(\frac{2m_e^*}{\hbar^2} \right)^{\frac{3}{2}} (E - E_c)^{\frac{1}{2}}, \quad 1.12$$

and

$$g_v(E) = \frac{1}{2\pi^2} \left(\frac{2m_h^*}{\hbar^2} \right)^{\frac{3}{2}} (E_v - E)^{\frac{1}{2}}, \quad 1.13$$

where m_e^* and m_h^* are the effective masses of electrons and holes (given by the curvature of the bands), \hbar is Planck's constant reduced by a factor of 2π and E_c and E_v are the energy of the conduction and valence bands respectively. The number of mobile charge carriers can be found through a simple integration of the density of states $g(E)$ and $f(E)$. The number of electrons and holes in their respective bands is given by,

$$n_e = \int_{E_c}^{\infty} g_c(E) f(E) dE \quad 1.14$$

and

$$n_h = \int_{-\infty}^{E_v} g_v(E) (1 - f(E)) dE \quad 1.15$$

from the bottom (E_c) to the top (∞) of the conduction band for number of electrons and the bottom ($-\infty$) to the top (E_v) of the valence band for holes. The top of the conduction band

1. INTRODUCTION

is not in reality infinity; however, despite the conduction band's finite width, this remains significantly larger than $k_B T$. In addition, as $f(E)$ tends to zero several multiples of $k_B T$ above the conduction band, the upper limit can be replaced by infinity. This further simplifies to,

$$n_e = 2 \left(\frac{m_e^* k_B T}{2\pi \hbar^2} \right)^{\frac{3}{2}} \exp \left(\frac{-(E_c - E_f)}{k_B T} \right), \quad 1.16$$

and

$$n_h = 2 \left(\frac{m_h^* k_B T}{2\pi \hbar^2} \right)^{\frac{3}{2}} \exp \left(\frac{-(E_f - E_v)}{k_B T} \right). \quad 1.17$$

The pre-factor to each of the exponentials are commonly denoted by N_c and N_v , which represent the effective density of states for the edges of the conduction and valence bands respectively. When in thermal equilibrium, for an intrinsic semiconductor,

$$n_e n_h = n_i^2 = N_c N_v \exp \left(\frac{-E_g}{k_B T} \right) \quad 1.18$$

where $n_e = n_h = n_i$ in the mass action law, represented in equation 1.18.

For an intrinsic (pure) semiconductor the E_F is close to the middle of the gap and electron and hole densities are equal. Via electrical doping, electron or hole density can be asymmetrically changed to create n-type or p-type semiconductors from which a p-n junction can be fabricated. This is at the heart of all inorganic solar cells (including Si). In case of organic semiconductors, the junction is often an intrinsic semiconductor sandwich between two metals (MIM) instead of p-n. An additional two major differences between organic and inorganic semiconductors are the lack of energy bands in organic semiconductors and hopping assisted transport as opposed to delocalised electronic states

1. INTRODUCTION

in banded (inorganic) semiconductors. In the next section organic semiconductors are briefly reviewed.

1.2 Organic Photovoltaic Cells: The Working Principle

Organic semiconductors are composed of conjugated molecules or polymers based on carbon, commonly including hydrogen, and sometimes also including heteroatoms such as nitrogen, oxygen, and sulphur. In contrast to crystalline inorganic semiconductors, organic semiconductors are weakly bound solids; meaning the spacing of neighbouring molecules is too wide for their orbitals to overlap. As a result, organic semiconductors do not form energy bands and instead have highest occupied molecular orbital (HOMO) and lowest unoccupied molecular orbital (LUMO) levels. These HOMO and LUMO levels are analogous to energy bands and can be viewed as effective valence and conduction bands of the organic semiconductor. Therefore, the conclusions from the previous chapter still apply to organic semiconductors, but with the difference that the carriers generally move much slower in organics compared to crystalline inorganic semiconductors. The slower carriers are partially compensated by organics' much thinner active layers resulting in less distance to travel prior to collection. In an organic solar cell (OSC), the active layer is composed of an organic semiconducting material/s which enables charge separation following initial mechanisms in the harvesting of solar energy [23]. The active layer is sandwiched between two charge transport (electron and hole transporting) layers and two electrodes, the anode and cathode as shown in Figure 1.4.

1. INTRODUCTION

1.2.1 Photocurrent Generation

As a result of the photovoltaic effect, current is generated in light-sensitive devices when exposed to an external light source. This current is photo-generated, therefore leading to the name of the mechanism, photocurrent generation. Photocurrent generation in an inorganic photovoltaic cell occurs when an incident photon is absorbed and excites an electron from the valence to conduction band (photoexcitation). The energy of the incident photon must be equal to or higher than the difference in energy between the valence and conduction bands (bandgap) to be absorbed and excite an electron.

The photoexcitation process within an organic photovoltaic cell is analogous with the inorganic process however not identical. As opposed to inorganic photocurrent generation, instead of the electron being excited from the valence to the conduction band upon successful absorption of an incident photon, it excites from the HOMO to the LUMO. In the HOMO ground state (also known as the pi state), the electrons are localised in pi bonds – these occur when double and triple bonds are present – typically associated with double bonds between carbon atoms in organic semiconductors. Photoexcitation sees the electron excite from the ground (pi) state to the higher energy (pi*) state (LUMO) leaving behind a hole in the pi state, this electron-hole pair is defined as an exciton [24]. Therefore, the energy required to excite the electron is equal to the energy difference between the HOMO and LUMO (energy gap); if an electron absorbs a photon of energy equal to or greater than the energy difference, photoexcitation occurs.

1. INTRODUCTION

The performance of a solar cell can be defined by the success of three main processes, harvesting of the target light spectrum and charge transport and collection. Upon evaluation, a cell's success at harvesting the sun's spectrum relies partially upon the spectral matching of the cell's absorption spectrum and the sun's emission spectrum. Due to narrow absorption spectra at higher energies, OSCs are generally lacking in the near infrared region (NIR). As a large proportion of the solar emission spectrum is in the NIR, the development of OSCs requires appropriate molecular design to tailor the energy gap and broaden absorption spectra to optimise the device performance [23].

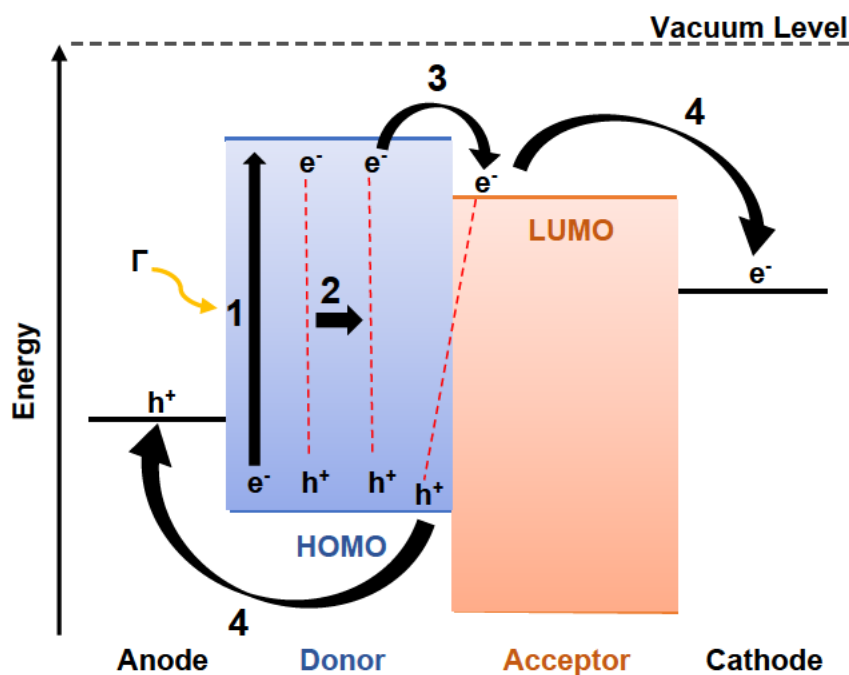


Figure 1.2: A schematic of the four operational mechanisms of photocurrent generation in a bulk heterojunction OSC where: 1. Exciton generation – a photon is absorbed, exciting an electron from the HOMO to the LUMO 2. Exciton diffusion – the exciton travels to the donor/acceptor interface 3. Exciton dissociation – the electron moves to the acceptor's LUMO and into a charge transfer (CT) state 4. Free charge collection at the electrodes [12].

1. INTRODUCTION

Solar cells exist within two classes, conventional and excitonic. In excitonic solar cells (XSCs), following the photogeneration of excitons they must diffuse to the interface in order to generate charge carriers; the charge carriers are generated and separated across the interface simultaneously. This differs from the conventional cell where free electron-hole pairs are generated throughout the active layer. The energy gap in an organic semiconductor (characterised as excitonic) is the energy required for optical absorption, this is less than the electrical bandgap required to create a free electron and hole [25]. This is due to the low dielectric constants of organic semiconductors compared to inorganic (around 3-4 compared with 11 respectively [26]) and weak intermolecular electronic interactions. The resulting charge carriers self-trapping creates a singlet exciton [27, 28], requiring them to overcome relatively significant binding energies in the range of 0.35-0.50 eV.

Organic semiconducting acceptor materials are added to the donor as the binding energies required exceed the typical thermal energy at room temperature. Without the added acceptor, it is very unlikely that the electron and hole would dissociate. The combined donor-acceptor morphology utilises the difference in electron affinities to create a driving force for the rapid transfer of the photoexcited electron from the LUMO of the donor to that of the acceptor [29]. At this stage, the electron remains close to its respective hole remaining in the coulombic attraction. As observed in the fourth mechanism of Figure 1.2, the separated electron and hole are formed in the charge separated (CS) state, this only occurs when the charge carriers in the exciton are distanced greater than the Coulomb

1. INTRODUCTION

capture radius. The charge carriers, once separated, travel to their respective electrodes and can be collected, inducing a photogenerated current [23].

In an OSC, following the photoexcitation of an electron from the HOMO to the LUMO (the first mechanism in Figure 1.2) a tightly bound electron-hole pair is created, namely the 'exciton'. The exciton is then required to travel to the donor acceptor interface to complete mechanism 3 in Figure 1.2; the exciton does this by exciton diffusion (mechanism 2 in Figure 1.2). Exciton diffusion lengths are generally short in organic semiconductors having exciton diffusion lengths 5-20 nm, this can limit the thickness of OSC active layers. Once at the interface between the electron donor (hole-transporting) and electron acceptor (electron-accepting) material in the active layer [30], the exciton dissociates (mechanism 3 in Figure 1.2) as the result of an electron transfer to the LUMO of the acceptor material giving rise to a CT state. Following this section an explanation of the device structure is provided.

1.2.2 Organic Photovoltaic Cells: Structure

Typically, the most efficient OSCs have a bulk heterojunction (BHJ) structured active layer. The BHJ solar cell was invented by Heeger *et al.* in 1995 [31] by combining two organic semiconducting materials in the active layer, an electron donor and acceptor. Observed performance increase was credited to the maximised interfacial area between the donor and acceptor materials in their so called 'interpenetrating phase-separated donor-acceptor network composite' [32]. The BHJ structure increases contact between the electron

1. INTRODUCTION

donating and accepting materials, increasing the overall donor/acceptor interface surface area. By increasing the donor/acceptor interface surface area, the excitons have a higher probability of dissociating and producing a photocurrent; therefore, relieving the nanometre constraints of exciton diffusion length on OPVs. Controlling the nano-morphology of the organic blend in the active layer can increase charge generation by way of fine dispersion of the layer; however, limiting the charge transport. Charge transport is maximised by adopting the bilayer; however, this blatantly reduces charge generation as it is a mechanism which occurs at the donor-acceptor interface. For example, in a characterisation of a PM6:IDIC material system device, a more considerable increase in short-circuit current density (J_{sc}) was observed from bilayer to BHJ structured active layer versus a more, although slight increase in open-circuit voltage (V_{oc}) from BHJ to bilayer. This resulted in a 21% increase in recorded efficiency [33]. It is obvious that the invention of the BHJ active layer structure was a profoundly important one in the history of organic photovoltaic cell development.

1. INTRODUCTION

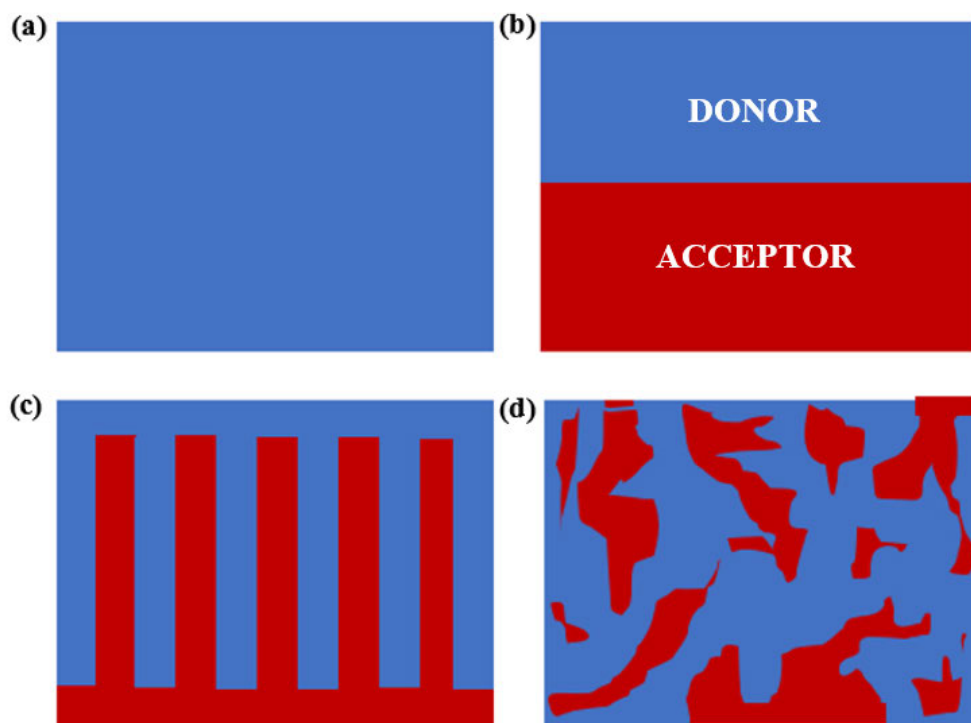


Figure 1.3: Schematic of four different OSC active layer morphologies, where blue and red indicate donor and acceptor respectively in (a) A singular donor layer (b) A donor-acceptor bilayer (c) The optimal morphology of the active layer (comb structure) and (d) The bulk heterojunction (BHJ) structure.

However, differences in electron affinities cause considerable intrinsic photovoltage loss that is not present in conventional inorganic solar cells therefore, nano-morphology has little impact on the final efficiency limit of organic solar cells [34].

1. INTRODUCTION

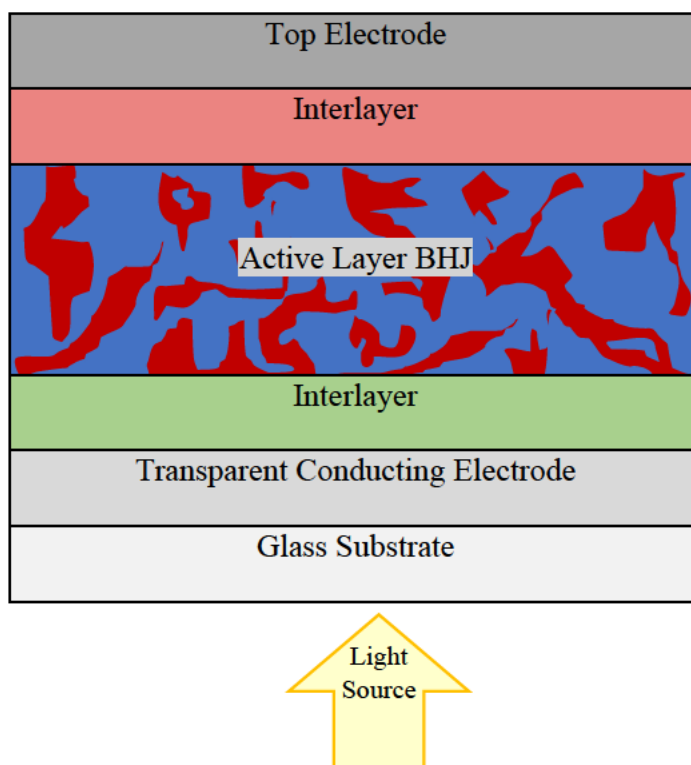


Figure 1.4: A schematic of an organic photovoltaic device with a BHJ structure. Orientation is implied by light source positioning.

A typical BHJ OSC structure is depicted in Figure 1.4, in which the BHJ active layer exists between two interlayers. These interlayers act to adjust work functions to increase compatibility between the active layer and respective electrodes. The electrodes, anode, and cathode, live on the exterior of the device either side of the interlayers. The electrodes are the destination at which the charge carriers are successfully converted into electrical energy. To allow for thorough illumination from the light source, one of the electrodes must be transparent, allowing the whole spectrum of photons passage to the active layer. Indium tin oxide (ITO) is a commonly used transparent conductive electrode (TCE) for OSCs.

1. INTRODUCTION

1.2.3 Power Conversion Efficiency: A Figure of Merit

A figure of merit is simply a quantity to characterise device performance relative to its alternatives [35]. There are several parameters of importance in solar cell characterisation informing on optimisation; however, power conversion efficiency (PCE) was developed as a useful figure of merit as it focuses on the efficiency of electrical power generated by any given solar cell. PCE is defined as the ratio of,

$$\text{PCE} = \frac{P_{\text{output}}}{P_{\text{input}}} \quad 1.21$$

the device's maximal operational electrical power output (P_{output}) and incident light power (P_{input}). As PCE is not a directly measurable value, it relies on other pathways of calculation based on measurable quantities. Both parameters in equation 1.21 can be reached by measurements of current and voltage; however, in solar cell characterisation the testing protocol (using a standard solar spectrum light source) has a standardised incident light power. Photovoltaic devices have several measurable factors such as short-circuit current (I_{sc}), open-circuit voltage (V_{oc}), and fill factor (FF); measurable current and voltage enable the calculation of P_{output} and therefore PCE.

In conclusion, PCE provides an important point of reference when comparing performance between photovoltaic cells. When accounting for the total cost of solar power generation, cell cost makes up only a small fraction. As a result, increasing the efficiency of photovoltaics causes a near-linear reduction in the cost of the devices [36] and the ability to track this progress aids the process.

1. INTRODUCTION

1.3 Characterisation of Solar Cells

The characterisation of solar cells is important for the comparison and tracking of parameters such as J_{SC} , V_{OC} , FF and ultimately PCE between research groups and industry across the globe. Historically, there have been a variety of methods for tracking efficiency progress, several methods rely on the collection of data at the maximum power point of a photovoltaic device, whereas other methods require combination of dark saturation measurements with measurements under either one or multiple different illumination conditions [37, 38, 39]. As measuring figure of merit, PCE, directly is not possible, analysing other parameters is necessary and is how other methods of characterisation are developed. These experimental methods may have different procedures, however, all determining PCE based on assumptions. The chosen method of characterisation of solar cells presented in this thesis is current-voltage (I - V) characterisation.

1.3.1 Current Voltage Characteristics

A photovoltaic cell's electrical behaviour is illustrated by mapping the relationship between current and voltage under various operating conditions, the result of which is defined as a J - V characteristic curve. This characterisation is performed by taking measurements of current across a sweep of voltages in a selected voltage range of a cell under air mass 1.5 global (AM1.5 G) illumination, or other standards where appropriate. Dividing the current

1. INTRODUCTION

values by cell surface area produces current density data for the solar cell. Current density is plotted against voltage, defining the J - V curve. Observable parameters include J_{SC} , V_{OC} , and the maximum power (P_{MAX}), representing the maximum current under short-circuit conditions, the maximum voltage across the cell with no external load, and the operating conditions that yield the highest electrical power output respectively [22].

The mentioned AM1.5 G spectrum is used as a reference spectrum for testing the performance of solar cells and modules as a critical part of characterisation. It provides a standardized representation of solar radiation, allowing for consistent comparison of different photovoltaic technologies. This is discussed further in *chapter 2.3.2*.

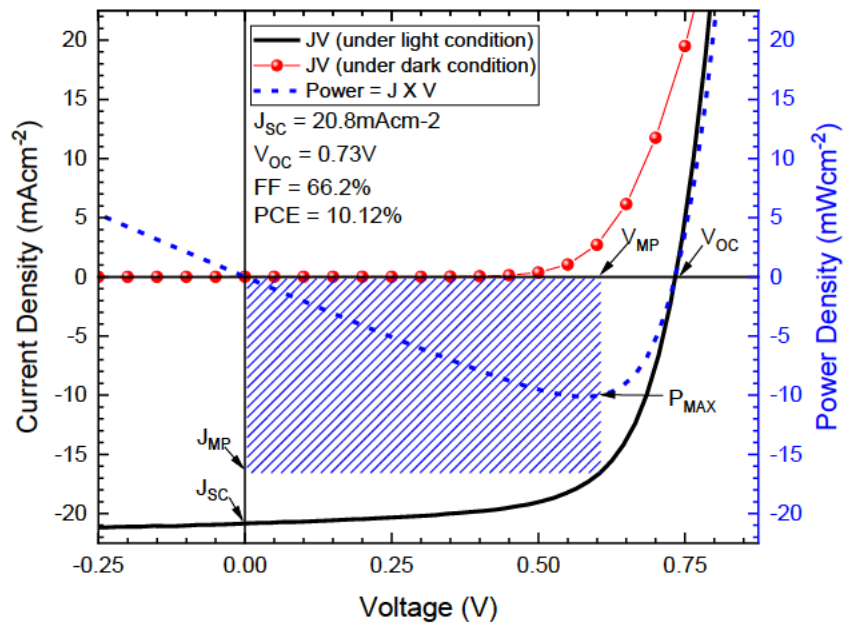


Figure 1.5: A typical J-V characteristic of a PM6:Y6 device. The solid black line is representative of the data measured under AM1.5 G illumination conditions and the red symbol line is data measured in dark conditions. The blue dashed line shows the maximum power output curve. Important parameters J_{SC} , V_{OC} , FF and PCE are listed also.

1. INTRODUCTION

In general, the J-V curve of a solar cell can be modelled and understood using the diode equation given as,

$$J(V) = J_d(V) + J_{sh}(V) - J_{ph} = J_0 \left[\exp\left(\frac{q[V - V_S]}{nk_B T}\right) - 1 \right] + \frac{V - V_S}{R_{sh}} - J_{ph} \quad 1.31$$

where the current density is the sum of diode (J_d) and shunt current (J_{sh}) densities minus the photocurrent density (J_{ph}) produced by the solar cell. J_0 is the dark saturation current density, V_S is the product of current density and series resistance (R_S), n is the ideality factor being a comparison to the ideal diode (where $n = 1$), and R_{sh} is the shunt resistance from current leakage due to active layer defects.

The above diode equation is utilised as it provides a theoretical framework, based on semiconductor physics, for understanding the behaviour of the solar cell under varying conditions. By applying the ideal diode equation, which accounts for the impact of temperature and material properties, one can analyse and predict the performance of solar cells, and the overall efficiency of energy conversion under varying operating conditions [40].

1. INTRODUCTION

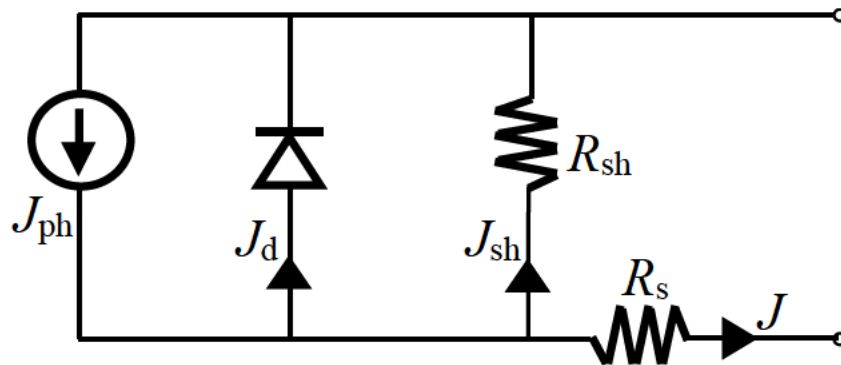


Figure 1.6: A circuit schematic of a typical PV cell, showing direction of current flow and applicable resistances described in equation 1.31.

A typical J - V curve is displayed in Figure 1.5, here key parameters are labelled, and the FF ratio is graphically presented. FF is the squareness ratio of the product of current density and voltage at P_{MAX} and the product of J_{SC} and V_{OC} . From these three quantities, PCE can be calculated.

1.4 PV Cells: From Outdoor to Indoor

1.4.1 IPV Characterisation Challenges

In line with early research investigating solar cell physics, IPV research presents multiple challenges. These challenges stand between researchers and the development of not only high performance IPV cells, but also testing protocols to compare them.

When compared to research into solar cell optimisation, indoor cells have no universal light standard at the moment. Solar cells are tested by characterisation using the solar standard

1. INTRODUCTION

sunlight spectrum, AM1.5 G. This testing protocol enables the direct comparison of solar cell development across the world and between research groups. However, due to the relative recency of IPV research – and as a result of varying illuminances and temperatures associated with artificial light – one indoor spectrum has not yet been standardised. Two popular colour temperatures of LEDs are 2700 K and 4000 K, a “warmer” and “cooler” toned white light, respectively. Without one standard LED spectrum to test within different research facilities, resulting data cannot be fairly compared.

In addition to the lack of a singular spectrum to characterise IPVs in conjunction with, the typical indoor light scenario presents new challenges such as diverged beams and inhomogeneous light distribution [18]. Issues highlighted above surrounding the characterisation of emerging IPVs, including the previously mentioned absent indoor light standard, provide explanation for the affected reliability of recent reports. Measurements do not have the same reliability and comparability as solar characterisation as in the majority of current cases there are significant limitations in the accuracy of indoor testing. The intensity dependent indoor $J-V$ characteristics recorded in this thesis was measured using an experimental set up developed by members in the Sêr SAM group at Swansea University. In collaboration with national laboratories and industry, an LED was chosen for this system in line with predictions for the upcoming indoor testing light standard. The set up and equipment is described in detail in *chapter 3*.

1. INTRODUCTION

1.4.2 Indoor Material Development

The previously conducted research and development of outdoor cells lends itself to the optimisation of more recent indoor cell optimisation ventures. Organic semiconductors are supported by well-established device physics and constant development in both device engineering and material design. When combined with the historically well-observed material properties of organic semiconductors such as their low-cost solution processing, lightweight and flexibility, they exhibit themselves as an appropriate and attractive choice for IPVs. Combining OSCs' challenges in large-scale fabrication, sensitivity to solar radiation and high temperatures, the most appropriate application for OPVs – based on technical superiorities and innate weaknesses – could be in IPV industry.

1.4.3 Advantages of Organic Indoor Photovoltaics

Due to differences in environment, intensity, and emission spectra, IPVs have different requirements for optimal efficiency and stability. In past decades, OPV devices had to be stored in inert atmospheres in hopes of avoiding rapid chemical degradation that resulted from oxygen, water, and electrode reactions with the organic active layer. Due to increased interest and research, small OPV cells on flexible substrates have lifetimes upwards of several years now [41]. Although an improvement on their short lifetimes, these figures are still vastly inferior to inorganic solar cells with lifetimes upwards of 25 years [29]. However, with different requirements for outdoor versus indoor device stability, prevention of sunlight degradation is not as crucial to IPV devices as for conventional PV devices used

1. INTRODUCTION

for solar harvesting; therefore, indoor OPV (IOPV) is emerging as an attractive option for indoor light energy harvesting.

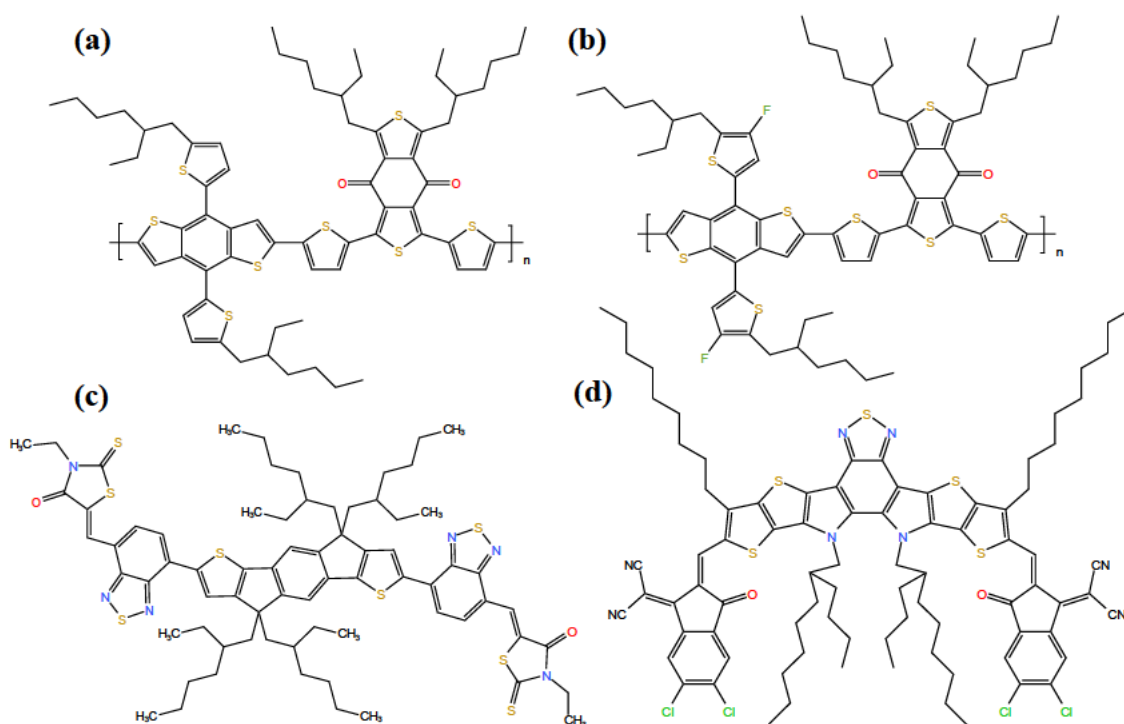


Figure 1.7: Schematic examples of semiconducting donor and acceptor molecules (a) PBDB-T (PCE-12) an electron donor (b) PBDB-T-2F (PM6) an electron donor (c) EH-IDTBR an electron non-fullerene acceptor (NFA) and (d) BTP-eC9 an electron NFA.

The focus on IOPVs is promising for several reasons, such as their previously mentioned unique properties of being lightweight and flexible. An additional, more desirable property of organic semiconductors for use specifically in IPVs, includes their high tunability in regards to optical absorption, which lends itself to the nature of typical indoor lighting spectra. Furthermore, by adapting the energy levels of the donor or acceptor material, through modifying their chemical structure, the difference in energy lost during charge

1. INTRODUCTION

generation is reduced [42]. The narrow emission and absorption peaks of indoor light spectra and organic photovoltaic cell properties respectively marry to produce a compatible light energy source and harvester.

In order for a successful move towards IOPVs, a more conclusive understanding of the properties of artificial light is required to maximise efficiency. The spectra of LEDs, although varied in many ways have one main property in common, they have narrow emission spectra relative to that of AM1.5 G [18]. Through embracing the narrow characteristic of LED ambient indoor light spectra and pairing them with organic light energy harvesting systems, the proportion of photoexcited electrons increases and as a result, increases PCE.

1.4.4 Importance of Indoor Photovoltaic Development

Ignoring the initial driving factors of applications in IPVs, the importance of utilising ambient indoor light is an obvious choice. Buildings such as hospitals, offices and warehouses present a scenario in which some form of ambient light is present 24 hours a day, 7 days a week. This is a significant quantity of light energy which is essentially wasted to the environment. Due to the availability of ambient light typically found within these buildings, they are readily deployable. Harvesting energy through photovoltaic devices in the mentioned environments will enable the amplification of power generation within these environments which become more abundant each day.

1. INTRODUCTION

The interest and importance of research into IPVs is garnered and demonstrated by the power required for constantly emerging technologies such as IoT. With the gross number of IoT devices in 2020 reaching 10 billion, the predicted number of IoT devices is set to triple by 2030. The exponential growth of electrically powered devices such as IoT inherently requires a consistent power supply; a condition that creates issues associated with battery maintenance and difficulty of installation (requirement of wires). Energy supply issues could limit future growth and diversification of functionality in the IoT ecosystem [43]. In consideration to the mass deployment of IoT, the requirement for convenient ways to enable and power these devices (moving away from traditional power sources) is more significant than ever before. Traditional solutions may utilise the use of battery power; however, batteries are unsustainable (hazardous materials going to landfill) and require periodic maintenance. When facing billions of devices, the ability to reduce maintenance is crucial, therefore battery power is not a sustainable option for this exponentially growing ecosystem.

1. INTRODUCTION

POWER CONSUMPTION

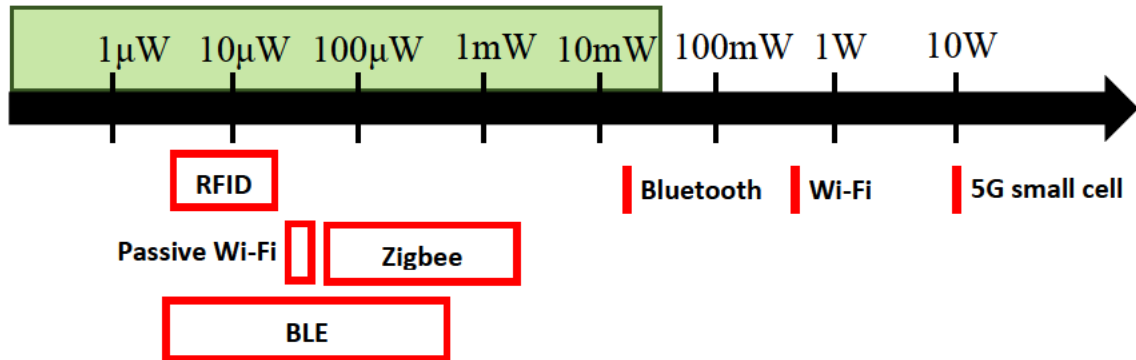


Figure 1.8: Power consumption scale of varying IoT communication protocols. Power consumption ranges are indicated by red boxes and red lines are exact values. The translucent green box highlights approximate indoor energy harvesting capabilities [20].

Solar spectrum intensities incident on solar cells are approximately between 2-3 orders of magnitude higher than intensities received by indoor cells (a combination of the ambient light source [LED] and indirect solar emissions) [44]. Therefore, IPV produce energy on orders of magnitude lower than standard outdoor PVs. However, the power requirement for IPV powered devices such as IoT is significantly lower (see Figure 1.8) hence, IPV remains a viable option to replace battery power in these devices. In addition to the challenges of maintaining battery powered devices, another large problem is the economic sustainability of battery powered IoT, which is unjustifiable to the rate at which these devices are being deployed at. Therefore, while simultaneously boasting minimal maintenance with a well-established sustainability advantage, photovoltaic energy harvesting emerges as an appropriate solution for an ever-growing problem.

1. INTRODUCTION

1.5 Summary

The introductory chapter of this thesis reviewed the fundamental physics of PV processes, an overview of working principles of OSCs with extension to IPV, and characterisation in addition to the challenges associated with, and importance of IPV development.

Currently, indoor characterisation measurements are subject to large errors and have no standard testing protocol; therefore, measured data cannot be deemed comparable. Throughout this thesis, exact claimed efficiencies of IPV from literature have not been referred to in attempt to avoid any unfair comparisons being drawn.

1.6 Aims of this Thesis

The introductory chapter of this Thesis explored the core learnings behind the research and development of solid-state semiconductors, organic solar cells, the Shockley-Queisser limit and indoor photovoltaics. Following on from core theory, in *chapter 2* the fundamental understandings of Shockley and Queisser will be further explained while employing additional considerations such as measured EQE_{PV} and non-radiative recombination predictions to assess the solar cell semiconducting optimal bandgap. Extending the thermodynamics of solar cells to indoor PV, *chapter 3* will draw on these SQ limit assumptions to predict the optimal material energy bandgap for application in the emerging field of indoor photovoltaics. Collated thermodynamic limit data on multiple proposed active layer material systems will provide an insight into potential candidates for high

1. INTRODUCTION

performance IOPVs; determined by their thermodynamic compatibility with the optimal energy bandgap for the chosen LED spectra. As a result, highlighting the realistic upper limit of IPV cells and inform on material choice, in hopes of fostering development in the field. This theory defines the initial phase of this body of work and heavily influenced the materials systems chosen to optimise and fabricate for testing under artificial indoor illumination. *Chapter 4* discusses the experimental data obtained through intensity dependent measurements taken under these conditions. Conclusions based on the gathered data refer to the effects of thermodynamic compatibility, leakage currents and non-radiative recombination mechanisms, informing on indoor photovoltaic active layer material choice. The aforementioned chapters of this Thesis aim to deduce the importance of thermodynamic compatibility in regards to IOPV performance.

Chapter 2

Theoretical Thermodynamic Limit of Solar Cells

2.1 Introduction

Edmond Becquerel observed the first evidence of the photovoltaic effect in 1839. He found that, immersed in a liquid two different brass plates produced a continuous current once illuminated with sunlight. At this point, the power conversion efficiencies were not exceeding beyond 1% and they did not improve dramatically for the next 75 years to come. However, by 1954 the single-crystal silicon solar cell was invented by *Chapin et al*, also emphasised by *Fuller* and *Pearson* [45], and far exceeded its predecessors with a 6% efficiency. By 2007, silicon cell modules dominated the market with 45% of sales coming from modules with multicrystalline cells and 40% from single-crystalline cells [46]. The record for silicon solar cell efficiency evolved from 14% in 1961 [47] (at the time the concept of detailed balance was published) to 26.7% in 2021 under AM1.5 G illumination [48].

As efficiencies climb, efforts have been made to obtain the theoretical limit power conversion efficiency of solar cells in the past. Kirchhoff's thermal radiation laws (1860), Planck's radiation law (1900), Einstein's radiative balance between two levels (1917) and Van Roosbroeck-Shockley radiative recombination in semiconductors (1954) can all be considered as precursors to the detailed balance limit proposed by Shockley and Queisser

2. THEORETICAL SOLAR UPPER THERMODYNAMIC LIMIT

(1961) [49]; the Shockley-Queisser (SQ) limit describes the theoretical upper limit for single junction solar cells. By taking the upper limit of J_{sc} , V_{oc} and FF (defined in *Chapter 1*), the SQ limit provides a theoretical threshold for solar cell efficiency. The solar cell efficiency is based on PCE, described in *Chapter 1*, the main figure of merit in solar cell characterisation under AM1.5 G illumination. The SQ limit model has been used to identify not only the upper limit of efficiency in individual solar cell systems to be aimed for in device optimisation, but also has allowed the identification of more thermodynamically appropriate material systems for use in solar photovoltaics.

While the SQ limit for efficiency is an important metric for tracking the progress of solar cell efficiencies, it considers radiative recombination as the only loss mechanism. This does not account for the voltage losses caused by non-radiative recombination of charge carriers. Therefore, the inclusion of non-radiative losses gives a more realistic estimate of the upper limit of efficiency to optimise towards.

Moving towards the Shockley-Queisser limit of efficiency, key technological and material advancements have led to the improvement of solar cell efficiency through recent history. In the 1950s and 1960s, there was a definite silicon dominance, the early focus was on cells primarily made of crystalline silicon. The development of the first practical solar cell by Bell Labs in 1954 marked a significant breakthrough. Moving forward, in the 1980s and 1990s, a new age of thin-film technologies influenced improvement in efficiency. Although efficiencies remained relatively lower compared to crystalline silicon, the 1980s saw the emergence of thin-film photovoltaics such as amorphous silicon and cadmium telluride

2. THEORETICAL SOLAR UPPER THERMODYNAMIC LIMIT

(CdTe) solar cells which allowed for reduced production costs and flexibility in application. In the 2000s, multi-junction solar cells gained attention, using multiple semiconductor materials to capture a broader spectrum of sunlight. Tandem solar cells, stacking layers of different materials, also emerged. Concentrator photovoltaics further improved efficiency by focusing sunlight onto small, high-efficiency solar cells [50] [51] [52].

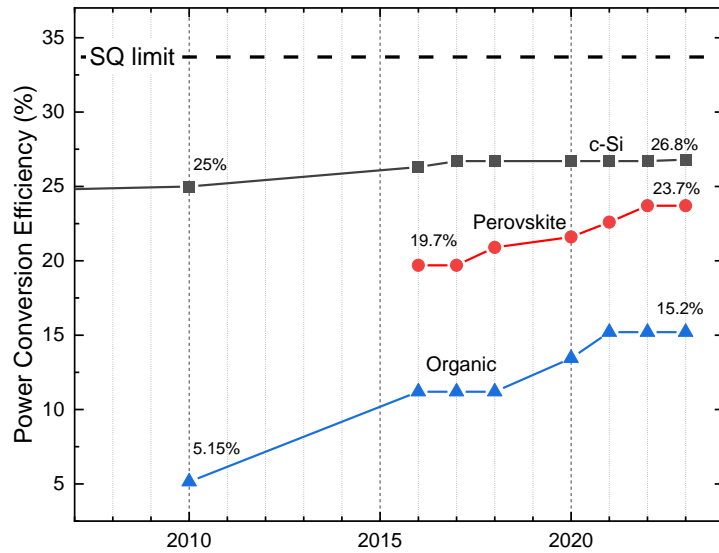


Figure 2.1: PCE timeline of novel solar cells from 2007 through to 2021 compared to the SQ limit (dashed line) of 33.7% at $E_g=1.14$ eV. Material systems are presented with the line and scatter graph key with crystalline silicon (c-Si), perovskite and organic in grey, red, and blue respectively. Data was collected from solar cell efficiency tables from 2001-2023 [53, 54, 48, 55, 56, 57, 58, 59, 60, 61].

While silicon modules remain the leading solar cells in the market in terms of the PCE, perovskites have made their progress within the last decade seem effortless. Perovskite solar cells, using a class of materials with a perovskite crystal structure, emerged as a promising technology in the 2010s. This material system has combined properties of

2. THEORETICAL SOLAR UPPER THERMODYNAMIC LIMIT

organics and inorganics to produce rapid efficiency growth from 3.8% to above 25% [62], growth that is historically unprecedented in photovoltaic research and comparable to traditional solar cells within a relatively short time. In addition to Si and perovskites having seen significant development in their efficiencies, OPV efficiencies have had a considerable increase through the utilisation of non-fullerene acceptors (NFAs). NFA-based devices have been promising in the development of OPVs due to significantly reduced recombination losses, resulting in efficiencies exceeding 18%. NFA molecules make electron acceptor level tuning more accessible resulting in reduced exciton dissociation energy losses. These reduced losses combined with higher mobility (enabling thicker active layers) and the material systems' lower effective energy gaps (1.4 eV vs 1.6 eV), promises higher attainable efficiencies [63].

Chapter 2 of this thesis will examine the history and process of calculating the SQ limit, the solar illumination standard and, characterisation protocols, as well as highlighting the progress of various solar cell material systems in relation to their theoretical upper limit of efficiency. Currently leading OSC material systems and efficiencies will be discussed as well as analysed relative to corresponding SQ limit calculations. Through this discussion, the importance of the energy bandgap will be emphasised and its link with OSC efficiency will be explored.

2. THEORETICAL SOLAR UPPER THERMODYNAMIC LIMIT

2.2 The Principle of Detailed Balance

“The Law of Entire Equilibrium” [64], “The Principle of Microscopic Reversibility” [65], “The Hypothesis of the Unit Mechanism” [66] and “The Principle of Detailed Balancing” [67] are various labels given to one definition over the past century. The detailed balance principle, as it will be named for the remainder of this Thesis, defines that if a system is in thermal equilibrium, then all microscopic processes in the system are compensated exactly by their respective inverse process. The distinguishing factor between the principle of detailed balance and any obvious prerequisite in maintaining thermal equilibrium is in the definition of thermal equilibrium. To maintain this equilibrium, exclusively zero net change in time anywhere in the system is required; therefore, optical generation could be compensated by non-radiative recombination processes which would breach the principle of detailed balance as the rate of emission may not be balanced by the rate of absorption [68].

The effects of the principle of detailed balance in relation to the calculation of PCE limits are discussed further throughout this chapter.

2.3 The Shockley-Queisser Limit

When developing a formalism for calculating the theoretical upper limit in PCE, Shockley and Queisser modelled their work of the detailed balance of photons absorbed and emitted at open circuit conditions [45]. The brief mention of SQ precursors in the introduction to this chapter documents the history of the balance between absorption and emission [49].

2. THEORETICAL SOLAR UPPER THERMODYNAMIC LIMIT

Utilising the definition of the detailed balance of radiative microscopic processes infers that the macroscopically observable photon fluxes are equal in equilibrium in and out of the device. Consequently, if the sample and environment are the same temperature, the black body radiation absorbed is equal to that emitted [68]. Unlike thermodynamic detailed balance, where a situation of no external forces is a required condition, the SQ calculation involves constant sunlight illumination; this creates a quasi-equilibrium condition. Therefore, electrons and holes are in thermal equilibrium within their respective conduction and valence bands, but there is a constant, non-zero chemical potential between them. As a result, the SQ limit is an extension of the principle of detailed balance under quasi-equilibrium conditions. When compared with the previously accepted semiempirical limit, the detailed balance limit exceeds it by only approximately 50% in the range of applicable energy gaps. The detailed balance limit, lying twice as far from the semiempirical limit and quadruple the achieved values at the time, suggested great improvements on PCE as possible [45]. Considering only radiative recombination mechanisms and infinite carrier mobility, PCE is calculated depending only on the semiconductor's energy bandgap. The semiconductor energy bandgap is an important parameter in PCE calculations as it informs the wavelength regime of photons that are capable of being absorbed and subsequently emitted. SQ, although a simplified model, is often used as a basis for additional energy conversion mechanism considerations [69, 70, 71, 72, 73, 74].

2. THEORETICAL SOLAR UPPER THERMODYNAMIC LIMIT

In conclusion, detailed balance simplifies the theoretical upper limit with a few main assumptions; despite the simple estimation of the SQ limit, it has proven extremely important in providing guidance for research in the photovoltaic field.

2.3.1 Conditions

There were five main assumptions considered by Shockley and Queisser when developing detailed balance; collectively, they summarised the ideally functioning solar cell. They are defined as the following:

1. Only photons of energy equal to or higher than the semiconductor energy bandgap are absorbed.
2. Each absorbed photon generates one single electron-hole pair.
3. Non-radiative recombination processes are neglected, and the only recombination process is radiative.
4. Resistive losses are assumed to be zero.
5. The cell temperature is assumed to be equal to the ambient temperature (300 K) [75].

These five conditions form the foundation for determining the maximum PCE of solar cells.

EQE_{PV} is defined by,

$$EQE_{PV} = \frac{\text{Extracted electrons/sec}}{\text{Incident Photons/sec}}. \quad 2.1$$

2. THEORETICAL SOLAR UPPER THERMODYNAMIC LIMIT

Considering 2 and 1 respectively, only photons with energy equal to or higher than the energy bandgap of the material are absorbed, and each absorbed photon generates one electron-hole pair. Hence, the EQE_{PV} used in the calculation of the SQ limit is simply characterised as a step function,

$$EQE_{PV} = \begin{cases} 1, & \text{when } E \geq E_g \\ 0, & \text{when } E < E_g \end{cases} \quad 2.2$$

where E is incident photon energy and E_g is the energy bandgap of the semiconductor. However, the absolute absorption of photons in the solar cell is unattainable due to energetic disorder, device thickness and absorption coefficients. In the context of application, the product of extended volume and perfect collection of charge carriers would require infinite carrier mobility. Therefore, an EQE_{PV} of 1 would never be experimentally observed.

In working principle, a photovoltaic cell converts (some of) the absorbed incident photon flux energy into work. As mentioned above, the regions of the photon emission spectrum (the solar spectrum for solar cells) that are absorbed by the cell are determined by the energy bandgap of the semiconductor material, with EQE_{PV} function ideally equal to equation 2.2. The absorbed photon's energy excites an electron from the valence to the conduction band. This produces an electron in the conduction and a remaining hole in the valence band. This situation is indeed expected inorganic crystalline Si cells at the time. Due to the focus on organic semiconductors in this Thesis, however, a more appropriate explanation for the process in organic solar cells sees the electron exciting from the HOMO to the LUMO energy levels and creates an exciton. In organic solar cells, the excitons can be further

2. THEORETICAL SOLAR UPPER THERMODYNAMIC LIMIT

dissociated at donor-acceptor interfaces into free charge carriers, namely electrons and holes. The free charge carriers have two possible fates, to be externally extracted by the circuit to produce a current or alternatively, to recombine before reaching the electrodes. Recombination can be radiative where a photon is emitted, or non-radiative where a photon is not emitted; therefore, resulting in other loss mechanisms. While non-radiative recombination can be reduced, in some cases, using materials of higher quality with a reduced existence of trap states, radiative recombination is unavoidable and a consequence of detailed balance. Therefore, in an ideal solar cell radiative recombination is expected to be the only recombination mechanism as stated in assumption 3.

When a solar cell is not under illumination, it will essentially be in equilibrium with its environment. The PV cell emits and absorbs at the ambient cell temperature (assumption 5) as a blackbody; this is under the assumption that emission occurs only for photons with energy equal to, or above, the bandgap energy via radiative recombination. Subsequent to illumination, the solar cell ceases to be in thermal equilibrium with its surroundings, generally resulting in a non-zero current. The total current generated is

$$I_{\text{total}} = q(\gamma_{\text{abs}} - \gamma_{\text{em}}), \quad 2.3$$

where q is the charge of an electron (elementary charge), and γ_{abs} and γ_{em} are the flux of photons absorbed and emitted, respectively. When the cell is illuminated, the emission rate must equal the absorption rate at open circuit conditions for continuity reasons [76].

As only radiative recombination is considered in the SQ limit, non-radiative recombination mechanisms that exist in the typical solar cell situation are ignored. When taking into

2. THEORETICAL SOLAR UPPER THERMODYNAMIC LIMIT

consideration the non-radiative recombination, V_{OC} is considerably lower than the situation which takes radiative recombination alone into consideration. To add further emphasis, the SQ limit is a simple but practical tool in the calculation of limit efficiencies [75]. It is notable to mention however, cells' efficiencies always sit below their upper theoretical limit. In conclusion, the acknowledgement and inclusion of real-world limitations such as EQE_{PV} and non-radiative recombination losses can paint a more reliable picture of maximum achievable PCE.

2.3.2 AM1.5 G Solar Standard

To accurately track the progress of solar cell efficiency, a fair comparison between research centres is necessary. The development of the solar standard was a necessary change due to the considerable variation in emission spectra experienced at different locations globally. With the incident surface solar emission being defined by the location (latitudinally and longitudinally), altitude, time of day and even weather conditions, the variations in measuring conditions, significant or minute, are seemingly limitless. If measurements were to be taken on the same day and exact time at two locations, the conditions may vary so greatly at each research site that it would be impossible to draw a fair comparison and conclusion between them. The variations in conditions from location to location are among other things affected by geometric considerations and atmospheric conditions such as reflectance; this ultimately creates an issue of measurement protocol.

2. THEORETICAL SOLAR UPPER THERMODYNAMIC LIMIT

To address this issue, the International Commission on Illumination standardised the first solar spectrum in 1972; this is where the use of a 1000 Wm^{-2} irradiance in a wavelength range of 290-3000 nm was suggested as a reference for solar intensity. The standard was further refined in 1982 by the American Society for Testing and Materials, a resulting three photon emission spectra emerged [77]: air mass zero (AM0), air mass 1.5 direct (AM1.5 D) and air mass 1.5 global (AM1.5 G). AM0, AM1.5 D and AM1.5 G are known as the extra-terrestrial, direct and circumsolar, and global tilt spectrum respectively. The ‘air mass’ description in all three spectra relates to how much atmosphere the light has passed through; therefore, AM0 has passed through none and AM1.5 D and G are at a value 150% of air mass 1 which would be the shortest path to the earth’s surface (approximately 9 km of effective atmosphere). Therefore, AM0 relates to solar cell research for space applications and AM1.5 for applications on the earth’s surface. AM1.5 G is the standard designed for flat plate modules in terrestrial use, therefore, this is the solar standard used globally to compare the characterisation of solar cell devices [78]. This was chosen as it represents an average yearly irradiance where there are many large population centres, making it a very important tool for solar cell characterisation.

2. THEORETICAL SOLAR UPPER THERMODYNAMIC LIMIT

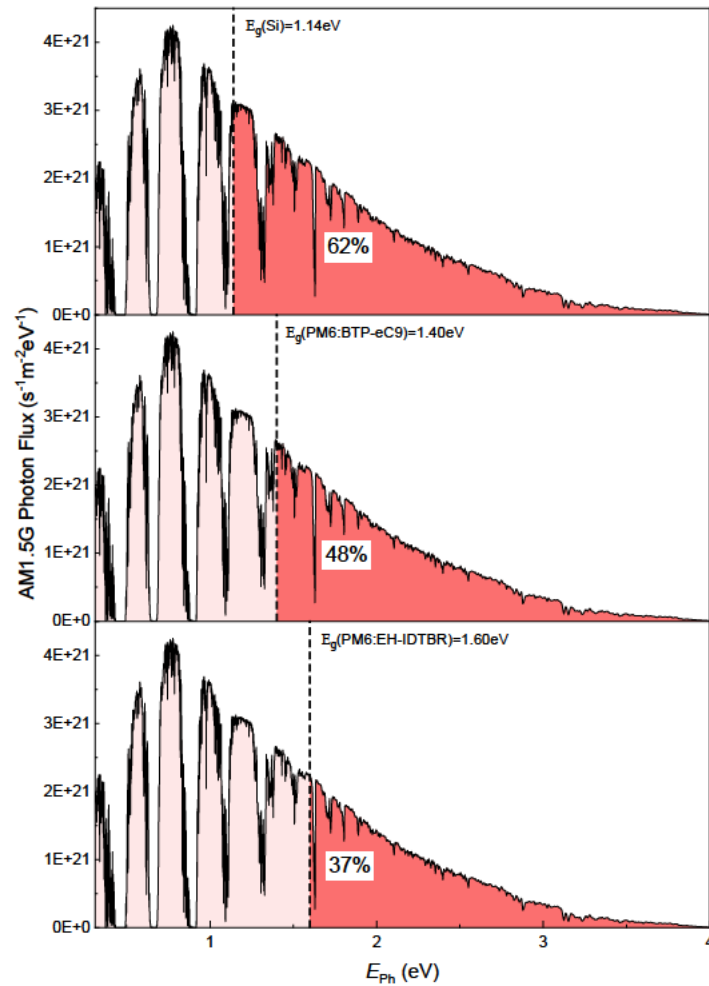


Figure 2.2: AM1.5 G solar spectrum as a function of photon energy. The top panel displays the ratio of photon flux with energy high enough ($E \geq E_g$) to be absorbed by silicon (Si) and the following respective panels present the same ratio for organic semiconducting material systems PM6:BTP-eC9 and PM6:EH-IDTBR.

The development and establishment of this standard provided researchers with a directly comparable spectrum to test all emerging devices. While the solar standard did not directly impact the material progress of solar cells, it was an aid as well as a necessity in monitoring the progress of solar cells throughout recent history.

2. THEORETICAL SOLAR UPPER THERMODYNAMIC LIMIT

As described in *Chapter 1*, only photons of energy equal to or higher than the semiconductor energy bandgap can be absorbed. When considering the process from incident photons to generated current, we understand that more photons absorbed results in more efficient energy harvesting and therefore more generated current. As shown in Figure 2.2, the standard solar spectrum (AM1.5 G) has a large proportion of its photoemissions in the NIR (0.65-2.0 eV). The majority of these lower energy photons cannot excite the electrons in wider energy gap organic semiconductors – such as PM6:EH-IDTBR – to the LUMO; therefore, they are only capable of absorbing 37% of the solar spectrum. When compared to Si, which can absorb 62% of the solar spectrum, the organic semiconducting system is harvesting 25% less of the sun’s radiative energy.

2.4 Shockley-Queisser Limit Calculation

Combining the foundational conditions initially set out by Shockley and Queisser with the solar standard for intensity (not established in 1961), the modern SQ upper limit for photovoltaic PCE performance can be calculated. The calculation of this refined SQ PCE can be described in the following process.

The EQE_{PV} has been previously defined through a ratio of extracted electrons and incident photons in equation 2.1. Another useful quantity is the internal quantum efficiency (IQE_{PV}) given by the ratio of electrons contributing to the external circuit per absorbed photon for a PV cell. Therefore, EQE_{PV} can be expressed as the product of the efficiency of photons absorbed by the active layer,

2. THEORETICAL SOLAR UPPER THERMODYNAMIC LIMIT

$$\eta_{\text{abs,AL}} = \frac{\gamma_{\text{abs}}}{\gamma_{\text{incident}}} = \frac{\gamma_{\text{abs}}}{\gamma_{\text{abs}} + \gamma_{\text{reflect}} + \gamma_{\text{trans}} + \gamma_{\text{parasitic}}} \quad 2.4$$

and the IQE_{PV} ,

$$\text{EQE}_{\text{PV}} = \eta_{\text{abs,AL}} \times \text{IQE}_{\text{PV}}, \quad 2.5$$

where $\eta_{\text{abs,AL}}$ is the absorption efficiency (absorptance due to the active layer AL) and $\gamma_{\text{parasitic/reflect/incident/trans}}$ are the absolute number of photons parasitically incident on and parasitically absorbed/reflected/transmitted by the PV cell's non-active layer.

When measured experimentally, EQE_{PV} spectra are plotted against the photon wavelength (λ) or sometimes the photon energy (E). In the SQ model for the upper limit of PCE, the EQE_{PV} used is a step function previously defined in equation 2.2. This suffices for estimated upper limits of efficiency; however, experimentally the measured EQE_{PV} would never be exactly 1. Therefore, this is a factor in the calculation of PCE which defines the thermodynamic compatibility of the material system used in the PV device and its solar spectrum absorbing capabilities.

When illuminated over an extended spectral range and under short-circuit conditions, the photocurrent density (J_{ph}) can be described by,

$$J_{\text{ph}} = q \int_0^{\infty} \text{EQE}_{\text{PV}}(\lambda) \Phi_{\text{ph}}(\lambda) d\lambda, \quad 2.6$$

2. THEORETICAL SOLAR UPPER THERMODYNAMIC LIMIT

where the light source's flux density is Φ_{ph} and J_{ph} is defined as the current induced by light. In solar cell characterisation, and therefore the calculation of the upper limit of PCE, the chosen light source spectrum is the standard AM1.5 G shown in Figure 2.2.

The J_0^{rad} is the corresponding current density measured under dark conditions (where the environment is void of external illumination) for which J_{ph} equals zero and J_0^{rad} is the total generated current density. Therefore, for J_0^{rad} the current density integral is a product of the EQE_{PV} and spectral flux of the environment which is taken to be a blackbody at room temperature,

$$J_0^{\text{Rad}} = q \int_0^{\infty} EQE_{\text{PV}}(E) \Phi_{\text{BB}}(E) dE, \quad 2.7$$

where,

$$\Phi_{\text{BB}} = \frac{2\pi E^2}{h^3 c^2} \exp\left(\frac{-E}{k_{\text{B}}T}\right), \quad 2.8$$

is an approximation for the Planck's blackbody flux (Φ_{BB}) at temperature (T) when $E \gg k_{\text{B}}T$.

When a sample is equivalent in temperature to its environment and the temperature does not change with time nor have any external forces acting (such as applied voltage or illumination) on the sample, it is said to be in thermodynamic equilibrium [68]. In dark conditions, the net current must equal zero to satisfy this equilibrium. Therefore, when voltage is equal to zero, so must current. In fact, for dark conditions, it can be shown that,

$$J_{\text{Total}} = J_{\text{R}}^{\text{Rad}} = J_0^{\text{Rad}} \left(e^{\frac{qV}{k_{\text{B}}T}} - 1 \right), \quad 2.9$$

2. THEORETICAL SOLAR UPPER THERMODYNAMIC LIMIT

where V is the voltage and J_R^{Rad} is the recombination current density where only radiative recombination is considered. The expression in equation 2.9 can be adjusted to define total current density in the illuminated condition by adding the light-induced current term $J_{G,L}$ as

$$J_{\text{Total}} = J_0^{\text{Rad}} \left(e^{\frac{qV}{k_B T}} - 1 \right) - J_{G,L}, \quad 2.10$$

to account for the photogenerated current when the solar cell is illuminated where $J_{G,L}$ is the total value of generated current density if all carriers are collected and therefore, $J_{G,L} = J_{\text{SC}}$. Based on equation 2.10, the open-circuit voltage – the voltage when net current equals zero ($V = V_{\text{OC}}$) – is defined by,

$$V_{\text{OC}} \approx \frac{k_B T}{q} \ln \left(\frac{J_{G,L}}{J_0^{\text{Rad}}} \right), \quad 2.11$$

when V is solved for $J_{\text{Total}} = 0$.

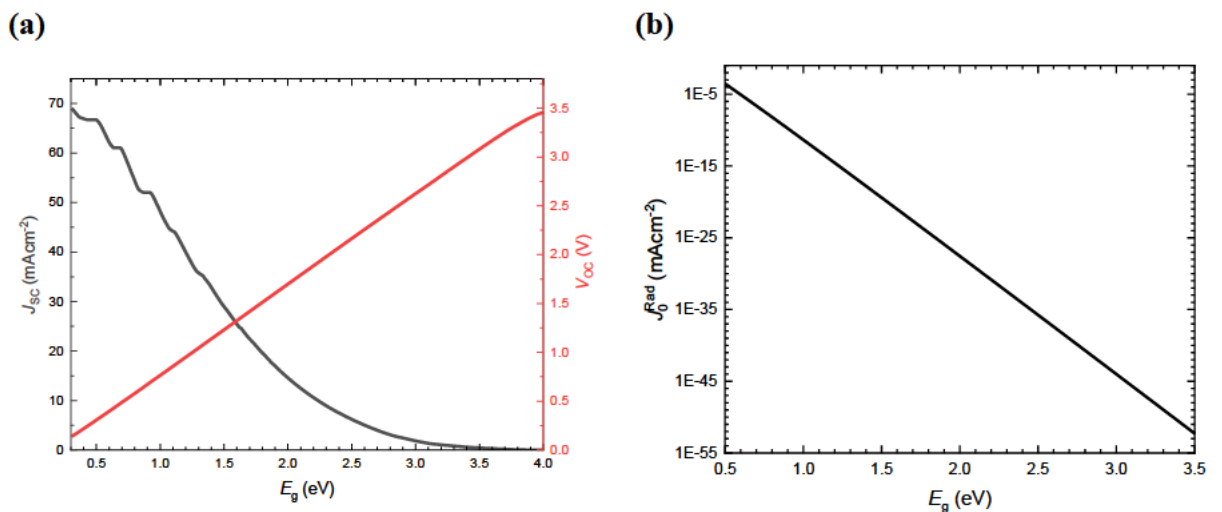


Figure 2.3: SQ upper limit of (a) J_{SC} and V_{OC} and (b) dark saturation current density considering only radiative recombination (J_0^{Rad}) as a function of energy bandgap.

2. THEORETICAL SOLAR UPPER THERMODYNAMIC LIMIT

The fill factor, FF , of a measured device can be calculated from its light J - V curve and, in short, is the squareness of the measured J - V characteristic curve. The value of J_{MP} and V_{MP} are defined as the current density and voltage values corresponding to the P_{MAX} on the J - V curve; this is shown in Figure 1.6, section 1.3.1. The fill factor is then defined as,

$$FF = \frac{P_{Max}}{J_{sc}V_{oc}} = \frac{J_{MP}V_{MP}}{J_{sc}V_{oc}}, \quad 2.12$$

the ratio between the product of J_{MP} and V_{MP} per the product of the short-circuit current density and open-circuit voltage. For J - V curves described by equation 2.10, FF is approximately given by

$$FF \approx \frac{\frac{qV_{oc}}{k_B T} - \ln\left(1 + \frac{qV_{oc}}{k_B T}\right)}{1 + \frac{qV_{oc}}{k_B T}}, \quad 2.13$$

the value of FF used in upper limit simulations of PCE in the remainder of this thesis.

As shown in Figure 2.3 above, J_{sc} and V_{oc} have opposite dependences with respect to the energy bandgap; hence, the optimal value of the product of the two parameters will have a trade-off depending on energy bandgap. Since the product of J_{sc} and V_{oc} is directly proportional to device PCE, high values in each must be a cautious and informed balance.

2.4.1 Theoretical Upper Limit: Power Conversion Efficiency

Power conversion efficiency, a figure of merit to describe the efficiency of a photovoltaic device, is given by the ratio of the output and input power of the device. We know the input

2. THEORETICAL SOLAR UPPER THERMODYNAMIC LIMIT

power (1000 Wm^{-2}) as a constant standard described by the AM 1.5 G spectrum in solar applications, whereas the output power can be calculated from a few important parameters. PCE was previously described in section 1.2.3 equation 1.21 in terms of powers, the power out can be further expanded into the following parameters: short-circuit current density, open-circuit voltage, and fill factor,

$$\text{PCE} = \frac{J_{\text{sc}}V_{\text{oc}}FF}{P_{\text{in}}}, \quad 2.14$$

where P_{in} is the input.

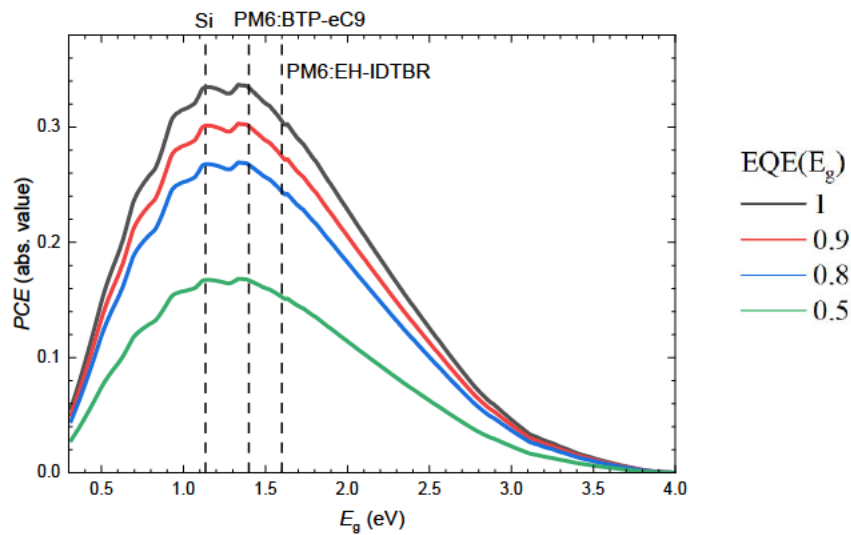


Figure 2.4: SQ PCE as a function of photon energy. Different simulated values of EQE_{PV} are identifiable by varying coloured solid lines. Three materials systems' bandgaps are labelled on the plot showing their upper theoretical limit; vertical dashed lines therefore represent material energy gaps for reference.

When assuming SQ conditions, PCE can be plotted with varying energy bandgap. This resulting analysis provides researchers with a theoretical upper limit for efficiency in solar cell devices. As shown in Figure 2.4, the SQ limit for efficiency is obtained to be 34% (2

2. THEORETICAL SOLAR UPPER THERMODYNAMIC LIMIT

sig. fig.), corresponding to energy bandgaps of 1.14 eV and 1.34 eV. This is different from the value found in 1961 by Shockley and Queisser at 1.1 eV for 30% efficiency, most probably explained by their use of a different solar spectrum for the calculations. This was due to the lack of a standardised spectrum prior to 2003 [79]. However, a notable mention goes to the energy bandgap of silicon at 1.12 eV [80]. With a bandgap similar to that corresponding to the SQ theoretical limit for efficiency, it makes silicon a leading material for promisingly high efficiency solar cells. Organics, in turn, are generally ‘wider gap semiconductors’ with energy gaps exceeding 2.0 eV in some cases; this makes them less thermodynamically appropriate materials for solar cell use as their absorption potential is reduced. Therefore, the SQ PCE calculations provide an important basis for material choice relative to the light source incident.

2.4.2 Theoretically Optimal Energy Bandgap

As the SQ limit calculation depends only on the semiconductor energy bandgap, it is beneficial to adequately clarify its link with efficiency. As inferred by Figure 2.2, the bandgap of the active layer material system for a solar cell is very important; the bandgap determines the portion of the solar emission spectrum photons that can be absorbed and converted into electrical energy. Therefore, the choice of material is largely dependent on bandgap and the overall spectral matching of emission and absorption spectra.

From the SQ PCE analysis shown in Figure 2.4, the theoretical maximum upper limit for PCE can be inferred. Additionally, another important conclusion is inferred from this

2. THEORETICAL SOLAR UPPER THERMODYNAMIC LIMIT

analysis – the optimal energy bandgap. This value yields the energy bandgap at which PCE is at maximum; the optimal energy bandgap for AM1.5 G under SQ conditions is found to be at 1.14 eV and 1.34 eV. The optimal energy bandgap is an important indicator of thermodynamically promising materials for use in solar cells, especially when predicting high performance material systems.

Historically, when observing high-performing solar cell material systems, inorganic semiconductor devices stand out. Silicon (Si) emerges as the most prolific solar cell material; with a bandgap of 1.12 eV, similar to that of the SQ optimal energy bandgap, Si solar cells have performed better than its organic counterparts. Organic semiconductor material systems' (more than one material) calculated energy gaps are representative of the effective bandgaps. These effective bandgaps are defined as the calculated energy difference between the donor's HOMO level and the acceptor's LUMO level [81]. Moreover, typically organic semiconductors have energy gaps 1.7-2.1 eV and above; in comparison to Si with a bandgap of 1.12 eV, this is considerably further from the optimal energy bandgaps predicted by the SQ model. Researchers have altered and narrowed the energy gap of organics in the past through varying polymer chain length [82]; this successful tuning of the bandgap from 2.1 eV to 1.2 eV can promote photon harvesting dramatically, from 30% to 80% as reported by *Moliton and Nunzi (2006)* [83]. However, fundamentally they are not as thermodynamically appropriate for solar cell applications compared to Si. Thermodynamic factors do not solely govern the efficiencies of solar cells. An important consideration of OPV performance is the lower intrinsic carrier mobilities

2. THEORETICAL SOLAR UPPER THERMODYNAMIC LIMIT

compared to Si and other inorganic materials. Nonetheless, it remains an influential factor in material choice.

2.4.3 Current High-Performance Organic Materials

Y6 and its derivative BTP-eC9, BTP-eC9-2Cl and HDO-4Cl based ternary devices have been reported to exhibit power conversion efficiencies of 18-19% with impressive FF s exceeding 80%. These improvements were mainly attributed to better charge transport and reduced recombination losses [84]. In general, the PCE of many organic semiconductors is limited by charge transport, characterised by low carrier mobilities. The highest efficiency PM6:Y6 devices have resulted from improved J_{sc} and V_{oc} attributed to the broader light absorption, while in contrast the reduced FF is limited by the less balanced charge transport [85].

Here arises the compatibility issue between thermodynamically appropriate materials and their charge transport properties which directly affects device performance. Through this analysis we can observe the importance of thermodynamically appropriate materials while acknowledging other factors that affect the efficiency of applied devices.

2. THEORETICAL SOLAR UPPER THERMODYNAMIC LIMIT

2.5 Non-Radiative Recombination Contributions

The SQ limit demonstrates both power and simplicity with equations that have resonated in the semiconductor community; however, it considers the energy bandgap as the only semiconductor parameter in its calculations, this is also its limitation [49].

Detailed balance states that there must always be some energy loss due to radiative recombination; therefore, voltage losses are inherent and define the theoretical upper threshold for V_{oc} [86]. Evolving from detailed balance, the SQ limit exclusively accounts for radiative recombination which occurs via the inverse process that photoexcitation of an electron absorbing an incident photon's energy and exciting to the LUMO energy level. This reverse process sees the electron relax to the HOMO energy level and releasing a photon of equal energy to the one previously incident and absorbed [87, 88, 89]. However, depending on the energy bandgap, doping level, fabrication process and material quality, a cell's performance level can be strongly affected. Therefore, non-ideal materials experience non-radiative recombination, where a photon is not emitted as a result. Typically, recombination is affected by two processes happening in series, the movement of the charge carriers towards one and other and the dissipation of energy by the electron-hole pair occurring at the interfacial CT state in organic heterojunction cells. The rate-limiting process is determined by the slower of the two processes happening in series. BHJ organic device recombination, both radiative and nonradiative, occur via the lowest CT state energy and work by *Benduhn et al.* [1] demonstrates the link between a higher overlap of vibrational modes of the CT and ground state with increased rates of recombination. It is

2. THEORETICAL SOLAR UPPER THERMODYNAMIC LIMIT

shown that the nonradiative recombination rate constant is increased with an increase in the overlap of occupied vibrational modes of the CT state with the most energetically accessible vibrational modes of the ground state. Therefore, this overlap defines the energy of the apparent CT state. This differs to the case of radiative recombination where spontaneous emission from the CT state to any vibrational mode of the ground state occurs [90]. Due, partially, to the high vibrational energy of the carbon-carbon bonds and the resulting considerable spacing of the vibrational states (typically 0.15 eV for molecular structures containing carbon-carbon bonds), understanding of the nonradiative recombination mechanisms is important in the aim to improve the performance of OPV devices. The mentioned nonradiative energy losses result in OSCs experiencing large energy losses ranging from 0.60-1.1 eV, this range sits significantly higher than the predicted SQ limit radiative losses of 0.25-0.30 eV [91]. For this reason, non-radiative recombination is a considerable reduction factor in the upper limit of efficiency [92, 93, 94] and must be accounted for to accurately depict the theoretical upper limit of power conversion efficiency of a solar cell.

Recombination rate can be described as

$$R = an + \beta n^2 + \delta n^3 \quad 2.15$$

the sum of 1st, 2nd, and 3rd order charge carrier (n) polynomial terms with different constants relating to Shockley-Read-Hall, bi-molecular and Auger recombination respectively. Due to the low dielectric constant associated with organic semiconductors, the coulomb attraction between the charge carriers is strong and the carrier densities can barely reach to

2. THEORETICAL SOLAR UPPER THERMODYNAMIC LIMIT

a point where Auger process is effective and dominant. In the introductory chapter of this thesis, the coulomb capture radius was described as the minimum displacement of an electron and hole pair prior to bi-molecular recombination when describing the four mechanisms from exciton generation to collected free charge carriers at the electrodes. Due to the nature of bi-molecular recombination, it is directly proportional to the square of the carrier density,

$$R_{\text{bi}} = \beta np = \beta n^2 \quad 2.16$$

where charge carrier densities of electrons (n) and holes (p) are equal to one and other when generation equals recombination and when the probability of this recombination is equal to 1, the recombination rate constant (β). In homogenous organic layers the associated β is expected to be equal to the Langevin recombination constant (β_L) which is proportional to the sum of the charge carrier mobilities as

$$\beta = \beta_L = (\mu_n + \mu_p) \frac{q}{\varepsilon \varepsilon_0}, \quad 2.17$$

where μ_n and μ_p are the electron and hole mobilities and ε and ε_0 are the permittivity of the semiconducting material and free space respectively. Experimentally, it is found that β in the active layer of organic solar cells is smaller than β_L by a pre-factor of ζ [95],

$$\zeta = \zeta_{\text{geo}} \times \zeta_{\text{CT}}, \quad 2.18$$

the product of bi-molecular recombination at the interface (ζ_{geo}) and by CT states (ζ_{CT}), where $\zeta \leq 1$. Since the extraction rate is proportional to the carrier density, we expect the

2. THEORETICAL SOLAR UPPER THERMODYNAMIC LIMIT

carrier density under illumination to be described by $G - R - n/t_{\text{ext}} = 0$, where t_{ext} is the extraction time and G the generation rate. Noting that the photocurrent is given by

$$J_{\text{ph}} = qd \frac{n}{t_{\text{ext}}} \quad 2.19$$

its intensity dependence can be clarified.

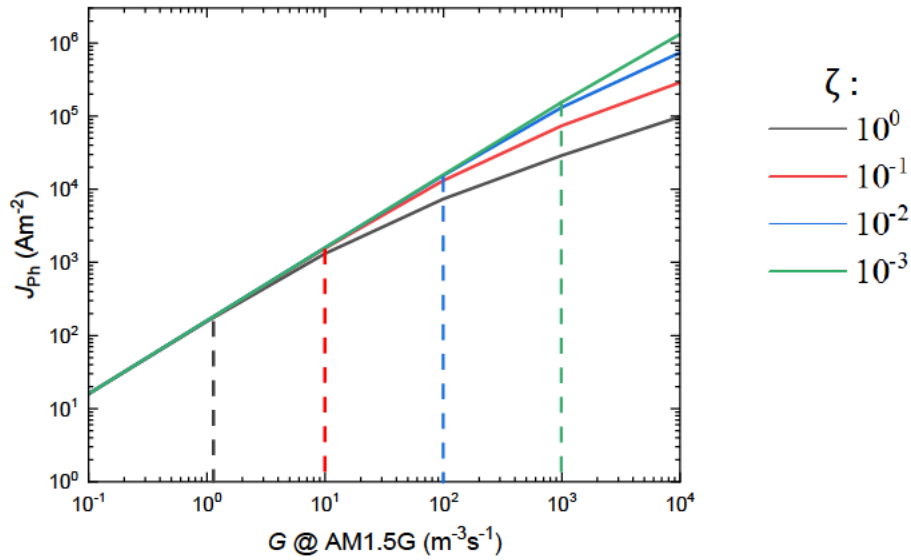


Figure 2.5: Light intensity dependence on photocurrent density. The different coloured solid lines represent varying values of ζ displayed in the key. Generation rate is proportional to light intensity and is normalised to the generation rate at AM1.5 G; therefore, $G = 1$ is the generation rate at AM1.5 G. Dashed coloured lines correspond to an estimation of the G at which photocurrent density is affected by ζ

For PV cells, the aim is to reduce ζ as much as possible to increase the FF and therefore the PCE. The intensity dependent relationship between photocurrent density and generation rate displayed in Figure 2.5 exhibits the effect of increased bi-molecular recombination as intensity is increased. However, upon deeper analysis, the effects on solar PV cells are more

2. THEORETICAL SOLAR UPPER THERMODYNAMIC LIMIT

significant as the non-linear deviation of generated photocurrent from the generation rate of charge carriers occurs at relatively low generation rates and therefore intensities when compared directly to AM1.5 G. This can be seen in Figure 2.5, with effects of ζ occurring at generation rates several orders of magnitude below that of AM1.5 G; therefore, bimolecular recombination dominates at high light intensities. For this reason, these effects are not as influential in IPVs as the lower intensities experienced by the cells will result in less generation. The device's FF will always have an upper limit meaning the continued decrease in ζ will not result in a FF of 1.

Resistive losses are also a factor influencing the efficiencies of solar cells. For solar cells to approach their theoretical efficiency limit, attention is not only to be placed on the materials but also on the reduction of the series resistance. Series resistance is a major contributor in solar cell efficiency limitations and, for example, by decreasing the dimensions of cells their series resistance area contribution is simultaneously reduced [75].

2.6 Summary

Chapter 2 of this thesis explored the history of the SQ limit as well as its working principle. A spotlight was placed on the assumptions that form detailed balance and the route to calculating the SQ limit. The history of the solar spectrum standard was researched and incorporated into the limit calculated which was compared to the limit reported in 1961 by Shockley and Queisser; differences were examined with possible causes mentioned and explained. From the SQ calculations performed in section 2.3.1, a maximum power

2. THEORETICAL SOLAR UPPER THERMODYNAMIC LIMIT

conversion efficiency of 34% was reached at an energy bandgap of 1.14 eV. This optimal energy bandgap was used in conjunction with spectral figures to further explain the use of Si and other semiconducting material systems in solar cells as opposed to OPV.

In conclusion, as an important indicator of material choice for application in high-performance devices, the SQ limit establishes itself as an important starting reference for PV optimisation. Despite its main historical focus on the solar cell limit, the maths utilised in this process can be applied to PV systems in a variety of different light sources. With interest in IPVs rising in recent years, detailed balance can be an equally beneficial tool for indoor as well as the already established outdoor. *Chapter 3* will investigate the upper thermodynamic limit for efficiency in IPV and utilise new experimental data surrounding non-radiative losses to improve this somewhat simplified analysis, informing material choice in a relatively new and promising field of research.

Chapter 3

Indoor Photovoltaic Thermodynamic Theoretical Limit

3.1 Introduction

Indoor PV (IPV) is defined as PV that harvests light energy from indoor environments to convert it into electrical energy. The majority of illumination received by Indoor PV devices is artificial having several orders of magnitude lower intensity than sun light. While sunlight delivers an illuminance of approximately 100,000 lux, indoor environment lighting (such as LED light) delivers illuminances typically between 200-1000 lux [44]. These light sources are usually located in homes or offices [96]. Unlike outdoor solar illumination, indoor artificial lighting constantly radiates at a consistent intensity peak, making it a stable form of energy for harvesting.

When designing an optimal IPV device, an important question posed at this time is that of active layer material choice. Materials have previously been optimised to approach the SQ limit for the solar standard; however, as IPVs are a relatively new field of interest for research, this limit has not been popularly calculated using an LED standard.

Material choice in photovoltaics can be governed by two leading factors in improving PCE, a more thermodynamically appropriate energy bandgap versus a material with better transport properties. Materials such as Y6 and BTP-eC9 are well-established materials in the organic solar cell field, with impressive transport properties responsible for their

3. INDOOR THERMODYNAMIC THEORETICAL LIMIT

increasingly high PCEs. By calculating the SQ limit for the indoor scenario with an LED standard, the optimal energy bandgap can be identified and connected to existing, previously researched material systems. These existing systems may have been poor performing active layers for solar cells but may outperform themselves when illuminated with an LED light at low intensities. *Harrison K. H. Lee et al.* [97] has shown the well-matched emission and absorption spectra of fluorescent lamps and PCDTBT respectively, due to fluorescent lamps existing mostly in the visible region compared to the vast number of infrared photons which cannot photoexcite electrons in these polymers. This highlights the importance of revisiting materials originally written off by research into solar cell optimisation. For example, PCDTBT based indoor photovoltaic devices outperform their same devices when illuminated with the solar spectrum [98, 99, 100, 101, 102, 103]. In addition, NFA materials have been shown to perform well under indoor illumination with some ITIC derivatives producing triple the PCEs under LED compared to solar AM1.5 G incident illumination [104].

With any growing field of research, results are being published boasting high-efficiency materials systems. The interest in IPV in recent history has seen the publishing of many investigative works where IOPV cells have been tested under artificial indoor lighting [105, 97]. PCEs exceeding 30% under a varied range of artificial lighting conditions were reported [106]. Lighting ranged from incandescent, halogen, and fluorescent bulbs to LEDs. Although high efficiencies are the route forward in IPV optimisation, due to a lack of indoor light standards and indoor light characterisation systems, publications are

3. INDOOR THERMODYNAMIC THEORETICAL LIMIT

incomparable due to inconsistencies in testing protocols [107]. By performing thermodynamic limit calculations applicable to the typical indoor environment, a theoretical upper limit for PCE in IPVs can be established, providing a realistic optimisation goal for researchers.

In *Chapter 3* of this Thesis, the theoretical upper limit for efficiency indoors will be calculated to inform on active layer material choice. These calculations will then be improved by replacing the Shockley-Queisser EQE step-function with EQE data. Processing these calculations will output a graphic informing the most thermodynamically appropriate materials predicted for IPV applications. By selecting the most promising material systems from these calculations and testing them under the indoor characterisation set up in the Swansea University Optoelectronics Laboratory, intensity dependant data can be measured. In *Chapter 4*, the experimental data from the thermodynamically promising material systems will then be compared against a material system which is well established in the solar cell field for its efficient transport properties. As a result, a graphic comparison of the importance of thermodynamic compatibility versus transport properties for the indoor environment can be analysed, exploring a key aim of this thesis.

3.2 Indoor Light Sources

21st century technology development is consistently increasing the demand for economically sustainable energy sources that reduce the requirement for constant and expensive maintenance. IPV devices with good performance fit this bill; however,

3. INDOOR THERMODYNAMIC THEORETICAL LIMIT

appropriate progress in optimisation of IPV performance is greatly impeded by the varying light conditions associated with the indoor environment [108]. Ideal IPV environments would have a consistent supply of light energy; for example, residential homes [109, 108, 110, 111], offices, factories [112] and hospitals [113, 114, 115, 116, 117]. Considered in impeding conditions is not only the nature of the artificial lighting indoors – which relative to time is constant, however between environments is widely varied – but in addition the natural daylight, which varies broadly throughout its daily period [110]. The mentioned environments of interest often have windows and use natural sunlight during the day for lighting, while simultaneously being subsidised by artificial light.

IPVs present different challenges compared to Solar PVs associated with light source position and orientation. Solar PVs can be placed onto roofs and in large open spaces such as fields; therefore, their positioning at an angle to the light source (sun) is easily kept consistent. In contrast to outdoor photovoltaics which are designed to face their light source, IPV positioning depends more on the environment and its individual requirements. It is assumed IPVs will be set onto surfaces such as walls and ceilings, implying direct and diffuse components of light [118]. Therefore, IPVs produce more obstacles in device characterisation due to their orientation relative to the light source to be harvested [119].

3.2.1 Indoor Light Source Standard

In comparison to the already well-established solar standard AM1.5 G described in *Chapter 2.2.2*, there is not currently a standard emission spectrum for use in characterisation of

3. INDOOR THERMODYNAMIC THEORETICAL LIMIT

IPVs. When addressing the development of an indoor standard light spectrum, there are several factors to consider. While solar emission has differences in intensity, indoor lighting not only has variations in its light intensity but also the type of light emitted, and colour temperature of the light also contributes to these variations. Common types of indoor lighting include cold cathode fluorescent lamps, incandescent bulbs, and LEDs. The visual differences in the distribution of these light spectra in turn would impact IPV performance. For example, the fluorescent lamp spectrum is made up predominantly of spectral spikes and incandescent bulbs produce a broad spectrum that spans thoroughly across the NIR region. This is distinctly different to an LED light spectrum as LEDs offer more control over the spectral distribution, allowing for targeted light output in specific wavelengths. The mentioned characteristic differences of fluorescent and incandescent light spectra compared to that of an LED would alter the proportion of photons incident on the photovoltaic cell with sufficient energy to cause an electron to photoexcite, eventually converting light to electrical energy [120]. The indoor thermodynamic limits presented in this Thesis focus exclusively on two LED spectra which are said to be strong contenders for the LED standard for IPV characterisation. The results, however, can be re-calculated straightforwardly for any arbitrary source spectrum. Two popular suggestions for the LED standard indoor testing spectra are 2700 K and 4000 K, a warmer and cooler white light, respectively (see Figure 3.1).

The 2700K and 4000K LED spectra are popular choices for indoor photovoltaic characterisation due to the large utilisation of 2700K lighting in residential, retail, and

3. INDOOR THERMODYNAMIC THEORETICAL LIMIT

hospitality spaces to promote a relaxed feel, and 4000K in offices, hospitals, and warehouses to promote a focused atmosphere. Due to their large presence in the spaces which are being targeted for the use of indoor photovoltaics, it indicates a need to optimise indoor cells material choice and operation to these environments. In additional support of this thinking, standardisation bodies such as the International Electrotechnical Commission suggest usage of the ‘white LED light’ for indoor photovoltaic characterisation [121] which corresponds closer to the ‘focused’ atmosphere lighting of 4000K.

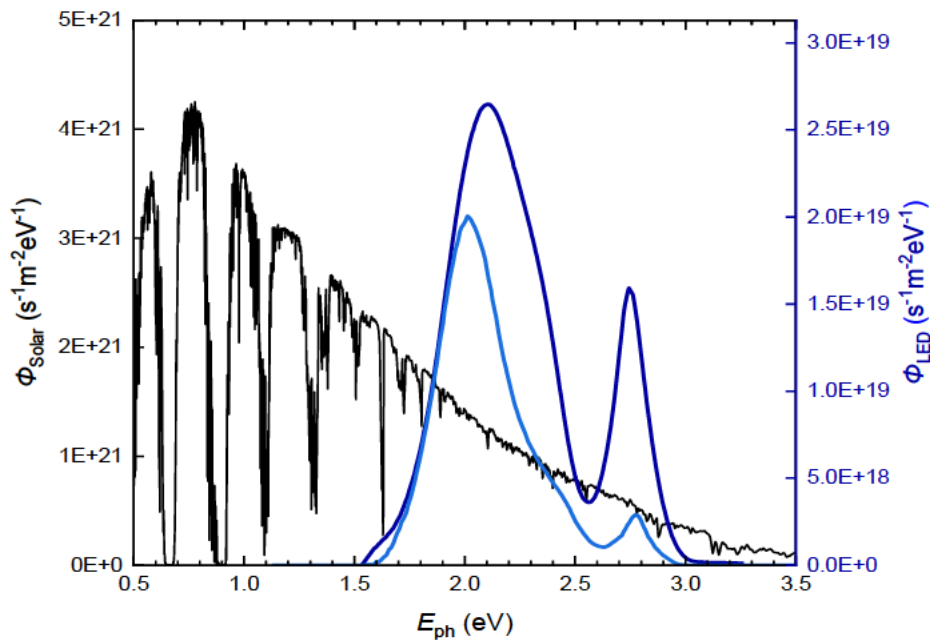


Figure 3.1: The comparison of three normalised emission photon flux spectra as a function of photon energy, including: AM1.5 G (left axis, black), 2700 K (right axis, light blue) and 4000 K LED (right axis, dark blue).

There are obvious differences between the chosen LED and solar spectra, as well as between the respective LEDs. Namely, the LEDs’ characteristically intense, narrow emission spectra, with peaks at shorter wavelengths compared with the broader AM1.5 G

3. INDOOR THERMODYNAMIC THEORETICAL LIMIT

spectrum [122]. From this comparison, it becomes evident that OSCs require a broad material absorption spectrum to match the broad emission spectrum of sun light. This, however, works in reverse for IPV requirements with a narrower, more finely tuneable material absorption being desirable. In addition to this, from a thermodynamic perspective, the LEDs' spectra being bluer than the sun generally require material systems with wider gaps. This is promising for the use of organic semiconductors in IPV as their highly and easily tuneable properties [123, 124] make them a favourable option.

Despite the variations in LEDs of different colour temperatures affecting the current characterisation of IPV cells, additional differences affecting active layer material choice also exist. Unfortunately, until an indoor light source is standardised, IPV cell characterisation metrics may subject to large errors.

3.2.2 Indoor Light Source Metrics

In solar cell characterisation SI units such as watts are used to describe the power and intensity supplied by the target light source. However, in IPV, existing artificial light source (photometric) terminology is adopted for consistency; including illuminance measured in units of lux. Illuminance describes the area density of luminous flux, measured in lumens, incident at a singular point. From illuminance, many light source metrics originate. Lux, the metric unit of illuminance, equates to the lumens per square meter. Other units, such as footcandle, are standard in the lighting industry, which is just another metric of lumens per

3. INDOOR THERMODYNAMIC THEORETICAL LIMIT

square foot – however, units of lux are the common terminology in IPVs pairing the industry (lumens) and physics (per square meter) [125].

The conversion from irradiance to illuminance is dependent on each individual emission spectrum. Illuminance is dependent on the way the human eye observes light. As a result, there is no consistent linear conversion constant that applies to all spectra. The conversion is described by,

$$\text{Illuminance} = \frac{\text{Luminous flux}}{\text{Area}} = \frac{L_0 \int V(\lambda)P_{\text{source}}(\lambda)d\lambda}{\text{Area}} \quad 3.21$$

where the L_0 constant is the maximum spectral luminous efficacy at a value of 683 lm/W, V is the standard relative eye sensitivity normalised to unity for the peak at 550 nm (visible green), P_{source} is the power spectrum of the radiation source and Area is the illuminated area.

| Spectrum | Illuminance (lux) |
|----------------------|-------------------|
| AM1.5 G | 116,000 |
| 2700 K LED | 529 |
| 4000 K LED | 105,000 |
| Sêr SAM (4000 K) LED | 1,000 |

Table 2: The illuminance values of the three light spectra used in the focus of this research to 3 significant figures.

Illuminance values of utilised spectra were calculated using equation 3.21 and recorded in Table 1 to reference in further text.

3. INDOOR THERMODYNAMIC THEORETICAL LIMIT

The European Union has a standard (NEN EN 12464-1:2011) which defines the illuminance requirements for different working situations, highlighting generalised examples of indoor lighting conditions (see Table 2). With areas next to a window well-lit with direct sunlight reaching upwards of 1000 lux, additional lighting is required in insufficiently lit areas of the indoor environment.

| General Rooms | Illuminance (lux) |
|---|--------------------------|
| Storage/ Corridors/ Stairs and Escalators/ Elevators | 100 |
| Warehouse | 150 |
| Toilets and Bathrooms/ Canteens | 200 |
| Reception/ Shop floor/ Classroom/ Sports hall | 300 |
| Office/ Meeting Room/ Cash desk/ Lecture room/ Library reading room | 500 |
| Precise working room (example: technical drawing) | 750 |

Table 3: The required illuminances of different indoor working situations as determined by the European Union (NEN-EN 12464-1:2011 en).

Due to the safety requirements for lighting levels, minimum illuminance levels for a number of relevant tasks and environments are documented by several governing bodies [126]. Requirements differ slightly between documents; however, a fair estimation of minimum and maximum illuminances indoors can be attained. Through these combined external measurements, illuminances as high and low as 750 and 5 lux are recorded respectively. Placed into perspective, direct sunlight equates to 100,000 lux and indirect

3. INDOOR THERMODYNAMIC THEORETICAL LIMIT

sunlight 10,000 lux; therefore, outdoor illuminance can be anywhere between 1-3 orders of magnitude greater than that of typical indoor light. As this difference in illuminance is so great, factors that reduced PCE in solar cells may be different to those affecting IPV. As a result, intensity dependent measurements of IPV devices during characterisation may inform on important factors of material system or device requirements and provide valuable insight into improving PCEs.

3.3 Intensity dependence on Leakage Current

Losses contributing to a reduced PCE can occur on a material system level or device level; within any PV device, there are two main sources of current loss through sheet resistance (R_s) and shunt resistance (R_{sh}). Shunt resistance evolves from the non-idealities or impurities related to device fabrication causing alternative conducting current paths for electrons and holes, and subsequent power dissipation [127, 128, 129]. Shunt resistance can be estimated by taking the inverse of the dark I - V slope at low voltages; the effect of the shunt resistance is simulated in Figure 3.3.

3. INDOOR THERMODYNAMIC THEORETICAL LIMIT

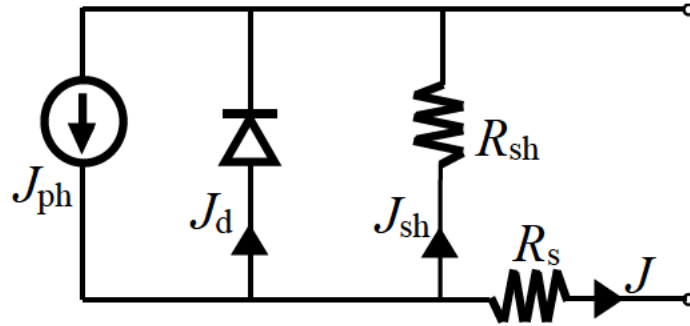


Figure 3.2: A circuit schematic of a typical PV cell, showing direction of current flow and applicable resistances.

As shown in Figure 3.2, the leakage current density (J_{sh}) being the result of a finite R_{sh} is opposite in direction to the photogenerated current density (J_{ph}). In addition to these parameters, we also have the diode current density (J_d) and finally the sheet resistance (R_s). As observed from Figure 3.2, the R_{sh} is in parallel to the J_{ph} ; therefore, maximum photocurrent density collected at the electrodes (J) arises from reduced J_{sh} as a result of increased R_{sh} .

To identify the effect of R_{sh} on J of the circuit, it can be described as such,

$$J(I, V) = J_d(V) + J_{sh}(V) - J_{ph}(I, V) \quad 3.31$$

where our total current output and photocurrent are functions of both the light intensity and the voltage, but the leakage current is dependent only on the voltage [130]. At high intensities, photocurrent is high enough to deem current losses associated with the shunt resistance negligible; however, at low-light intensities typical of indoor lighting, the R_{sh} may cause major losses which can be observed in the V_{oc} and FF .

3. INDOOR THERMODYNAMIC THEORETICAL LIMIT

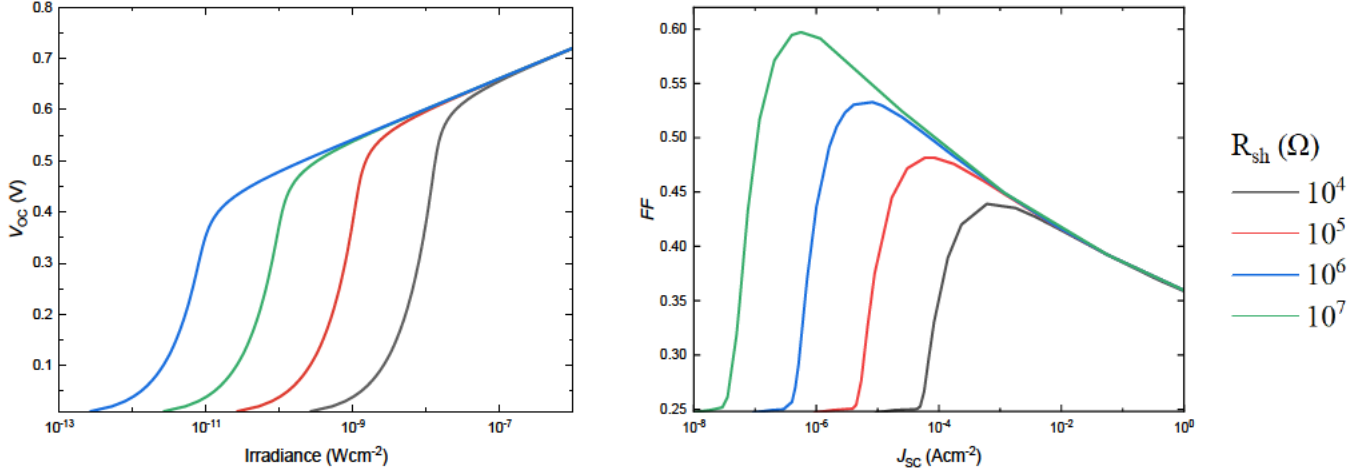


Figure 3.3: Intensity dependence with varying R_{sh} on (a) V_{OC} and (b) FF . The dashed lines from left to right indicate irradiance values of a 4000 K LED at 50 lux and 1000 lux as well as the irradiance value of AM1.5 G. Varying R_{sh} is differentiated by the colour of the solid lines described in the key.

When considering solar cells, the effects of series resistance significantly outweigh those of shunt resistance. In contrast, IPV devices experience PCE losses in the opposite way. As shown in Figure 3.3, R_{sh} causes a considerable loss in open circuit voltage at lower intensities as well as significant effects in resulting FF . As R_{sh} limits V_{OC} where $V_{OC} \ll V_{OC,sh}$ where,

$$V_{OC,sh} = J_{SC}R_{sh}. \quad 3.32$$

When experiencing high intensities, J_{SC} is high and results in the V_{OC} being determined by the logarithmic dependence of the recombination of photogenerated carriers. However, at low intensities, the V_{OC} has a linear dependence on both J_{SC} and R_{sh} , limiting V_{OC} as shown in Figure 3.3(a). Using this logic and replacing V_{OC} with proxy value of E_g/q , we can find a critical R_{sh} ,

3. INDOOR THERMODYNAMIC THEORETICAL LIMIT

$$R_{\text{sh,critical}} = \frac{E_g}{qJ_{\text{SC}}}. \quad 3.33$$

where ideally, the R_{sh} must be larger than the critical R_{sh} value ($R_{\text{sh,critical}}$). This is an important limiting factor in IPV development due to the lower light intensities typical of the indoor environment. In conclusion, devices with high R_{sh} are required for high-performing IPV PCEs.

3.4 Shockley-Queisser Limit: Indoors

3.4.1 Indoor Theoretical Upper Limit: Power Conversion Efficiency

To calculate the theoretical indoor upper limit for PCE in a photovoltaic cell, we make use of Shockley-Queisser model once again. However, to replace the AM1.5 G solar spectrum two different LED spectra are considered, a warm and cool white light, 2700 K and 4000 K, respectively. Accepting that there is no indoor spectrum standard currently, the two LED spectra were used to offer some variation in the calculations which would address varying indoor scenarios.

To produce a more realistic value for the Shockley-Queisser calculations, an EQE_{PV} step function of value 0.8 was used instead of 1,

$$EQE_{\text{PV}} = \begin{cases} 0.8, & \text{when } E \geq E_{CT} \\ 0, & \text{when } E < E_{CT} \end{cases}. \quad 3.41$$

This represents a more realistic photovoltaic device situation and provides a more realistic value for predicting power conversion efficiencies. In addition to this consideration, non-

3. INDOOR THERMODYNAMIC THEORETICAL LIMIT

radiative voltage losses were included in the final PCE calculations to better estimate the indoor environment. Total V_{OC} loss can be described as,

$$\Delta V_{OC,loss} = \Delta V_{OC,rad} + \Delta V_{OC,nr} \quad 3.42$$

where $\Delta V_{OC,rad}$ is the radiative open-circuit voltage loss and $\Delta V_{OC,nr}$ is the non-radiative open-circuit voltage loss. Research showing a trend of decreasing $\Delta V_{OC,nr}$ with increasing V_{OC} , despite $\Delta V_{OC,nr}$ varying widely for similar V_{OC} values, provides evidence of the trend having dependence on the non-radiative decay process as opposed to defected materials. As a result, this suggests a dependence on the wavefunction overlap between the high energy ground-state modes and the occupied modes of the excited state. From this an energy gap law is deduced for transitions that are radiation-less. This defines the decreasing non-radiative decay constant with increasing energy gap between the ground and excited state. Therefore, the charge-transfer state (E_{CT}) affects not only the radiative V_{OC} limit, but also the $\Delta V_{OC,nr}$ [131].

The models used were made using experimental data from *Benduhn et al.* [1] and *Ullbrich et al.* [132], they make up several differing PCE approximations from radiative and optimistic values to lower limits based on a range of experimental data.

3. INDOOR THERMODYNAMIC THEORETICAL LIMIT

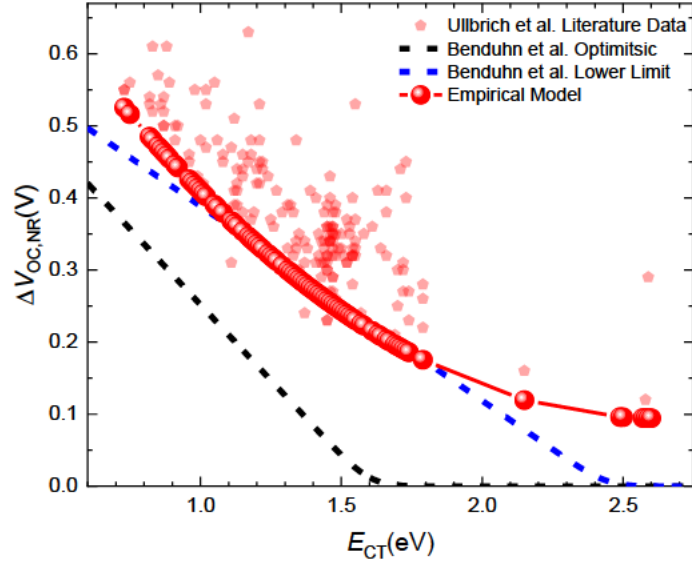


Figure 3.4: Non-radiative voltage losses as a function of bandgap energy. The two dashed lines, black and blue, are representative of two non-radiative models referenced in this Thesis, an optimistic and lower limit model respectively [1]. The translucent, red pentagons are collated literature data reported by *Ullbrich et al.* [132], while the red circle scatter and line data represents the lower limit empirical model created for this Thesis from the *Ullbrich et al.* [132] reported data.

The three models for non-radiative voltage losses are plotted in Figure 3.4; these values were found using *Benduhn et al.* [1] and *Ullbrich et al.* [132]. We can observe from this that, in the generic case, the non-radiative voltage loss decreases with increasing bandgap energy. Therefore, depending solely on the non-radiative losses, the PCE theoretical upper limit would correspond to a wider energy bandgap.

3. INDOOR THERMODYNAMIC THEORETICAL LIMIT

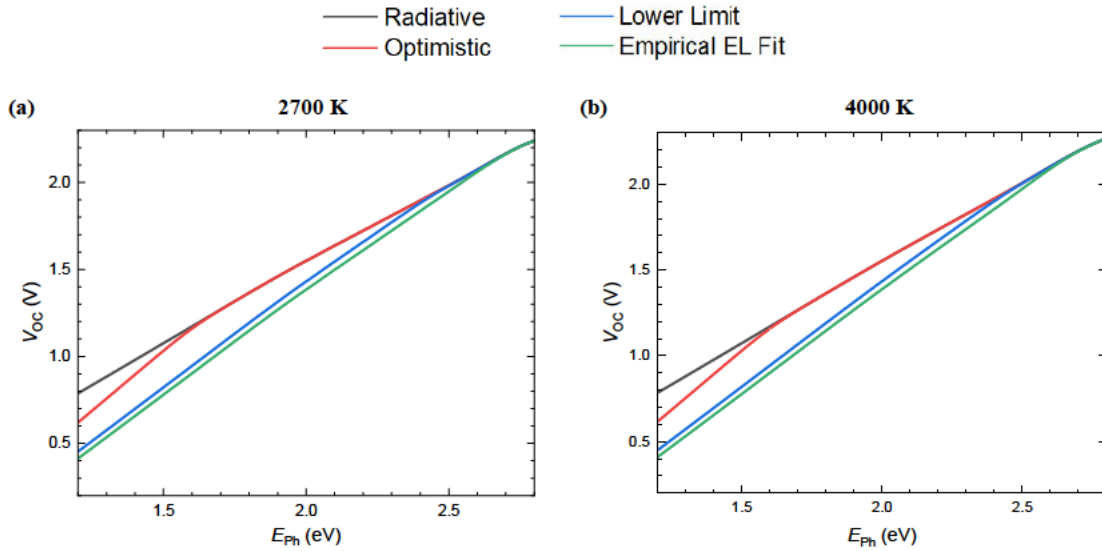


Figure 3.5: Simulated open circuit voltage as a function of bandgap energy for four models: radiative, optimistic, lower limit and the empirical fit from Benduhn et al. [1] represented by black, red, blue, and green solid lines respectively. Simulated using the LED spectra of (a) 2700 K and (b) 4000 K.

To apply these non-radiative loss models to my indoor application a new open circuit voltage is calculated from our baseline Shockley-Queisser limit, a radiative theoretical upper limit presented in Figure 3.5. Moving on intuitively from this calculation, these open circuit voltages are then used in place for the PCE calculations, providing theoretical PCE limits for a range of optimistic through pessimistic non-radiative estimations.

3.4.2 Indoor Theoretical Optimal Energy Bandgap

Resulting from the vast difference in the emission spectra between typical indoor lighting and the solar standard, the calculated indoor maximum power conversion efficiency corresponds to a significantly different optimal energy bandgap. This variation in optimal

3. INDOOR THERMODYNAMIC THEORETICAL LIMIT

energy bandgap results in the requirement of different active layer material systems to harness more thermodynamic compatibility to generate higher PCEs.

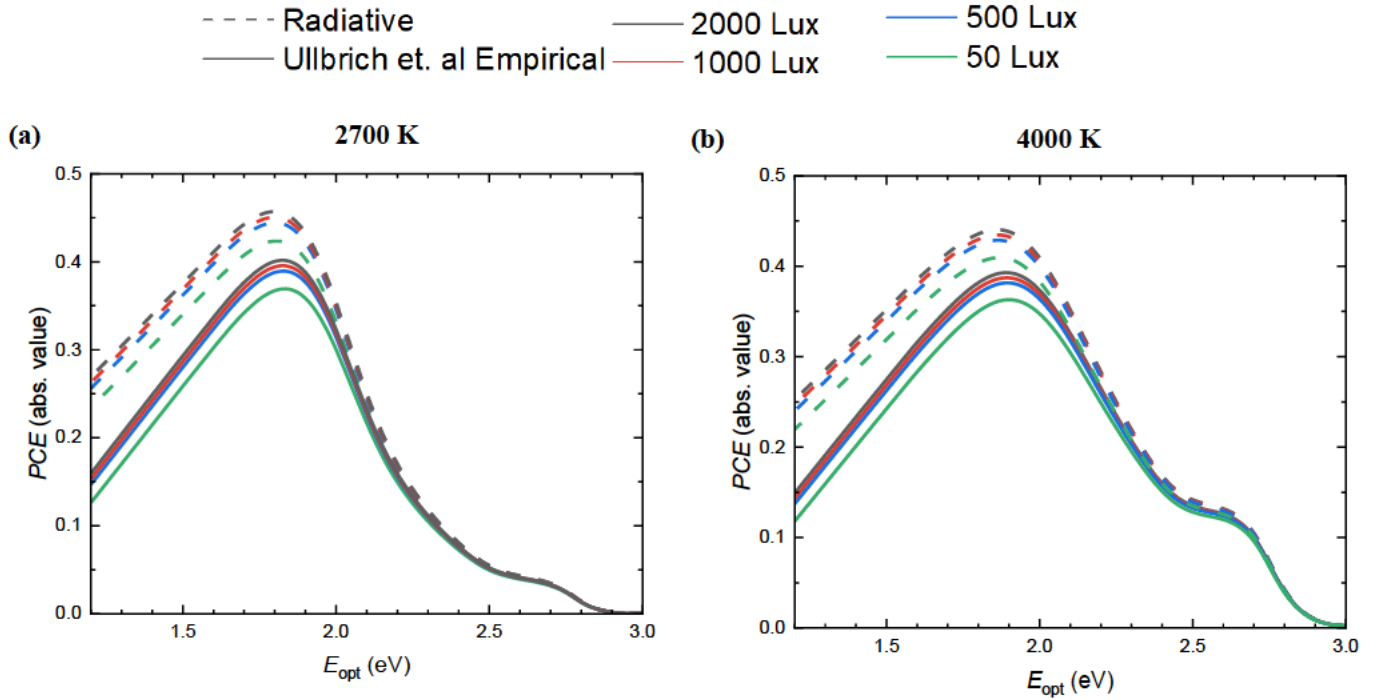


Figure 3.6: Simulated PCE as a function of optical energy bandgap for LEDs of (a) 2700 K and (b) 4000 K.

As shown in Figure 3.6, the radiative SQ limit produces a higher simulated value for PCE over the one including non-radiative losses described by an empirical model based on the *Ullbrich et al.*. The maximum PCEs for a 4000 K and 2700 K LED are therefore produced at optimal energy bandgaps of 1.89 eV and 1.84 eV (as shown in Figure 3.6 panels (a) and (b) respectively) in comparison to the optimal energy bandgaps of 1.14 eV and 1.34 eV for solar simulations. As such, for IPV's the SQ model predicts thermodynamically appropriate materials with a similar energy gap to that of the optimal gap produced in this simulation and analysis.

3. INDOOR THERMODYNAMIC THEORETICAL LIMIT

3.4.3 Chosen Indoor Organic Active Layers

Utilising the Shockley-Queisser theoretical limit calculations (equations 2.6, 2.11, 2.13, and 2.14) previously derived in *Chapter 2.3.1*, thirteen of Sêr SAM's existing active layer material systems' EQE_{PV} data was processed and compared in terms of J_{SC} , V_{OC} , FF and PCE. This analysis allowed the direct comparison of each parameter, producing a short-list of the most promising material systems for IPV applications. This analysis was performed using the 2700 K LED (500 lux) to simulate a typical indoor light source; therefore, this analysis identifies the material systems most thermodynamically tuned to the emission spectrum of this artificial light source.

3. INDOOR THERMODYNAMIC THEORETICAL LIMIT

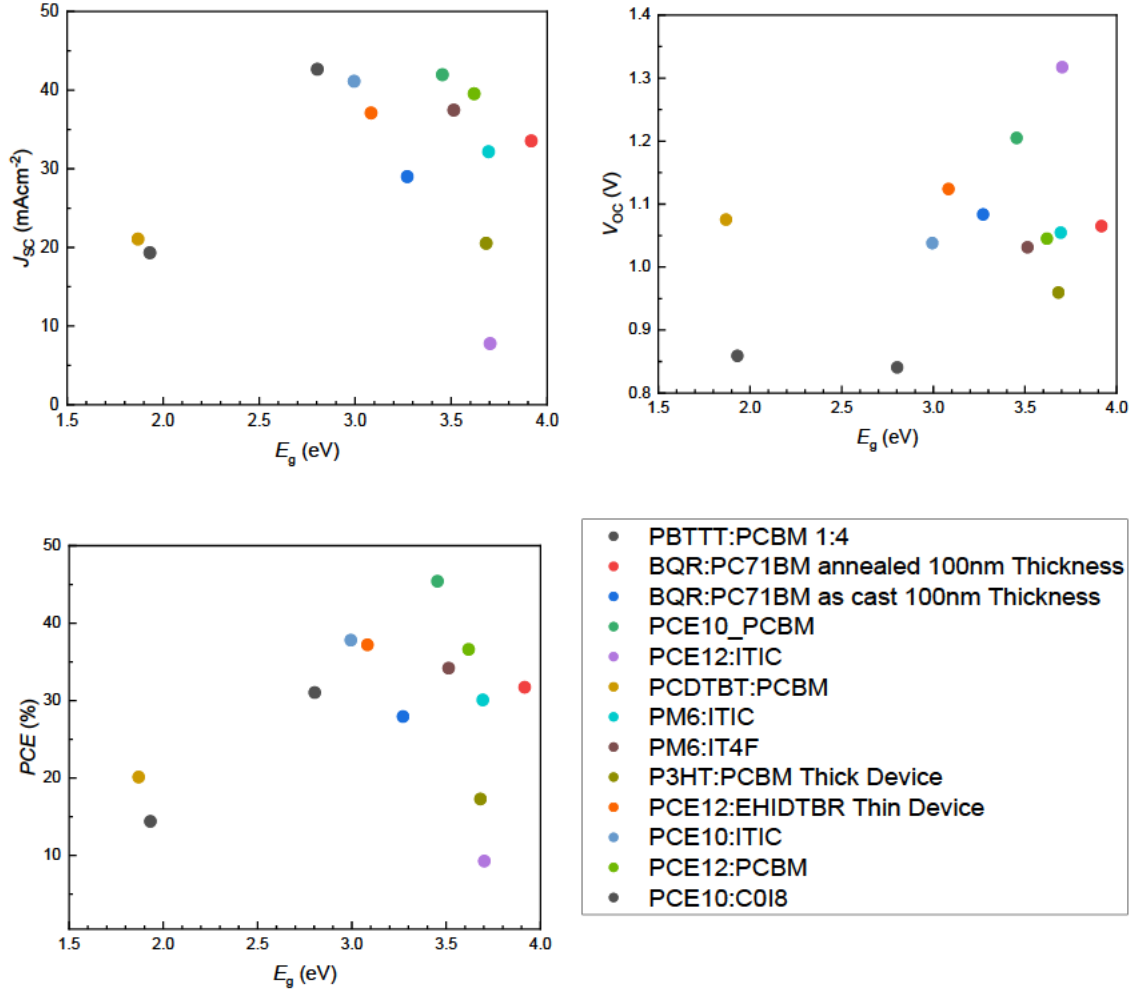


Figure 3.7: An analysis of three main parameters in OPV using a 2700 K LED 500 lux spectrum. The first three panels in order analyse J_{sc} , V_{oc} and PCE respectively. The final panel is a key for the data presented in the other three panels.

As seen in Figure 3.7, PBDB-T:EH-IDTBR stood out as a promising material system from the analysis of existing EQE_{PV} data. With other material systems' figures of merit fluctuating generously from J_{sc} to V_{oc} , PBDB-T:EH-IDTBR boasts high, but balanced, J_{sc} and V_{oc} ; the product of these two reflecting the PCE when illuminated indoors.

3. INDOOR THERMODYNAMIC THEORETICAL LIMIT

When reviewing the EQE_{PV} data of PM6 and EH-IDTBR, the bandgaps were noted, and they made for a good spectral match for the theoretical optical bandgap calculated from the indoor Shockley-Queisser limit. Therefore, PM6:EH-IDTBR was chosen as the second material system to be investigated. Both PBDB-T:EH-IDTBR and PM6:EH-IDTBR share one common attribute, their thermodynamically appropriate bandgaps. Using the Shockley-Queisser theory, this suggests their possible success for IOPV applications.

As confirmed by years of OPV research, PM6:Y6 and derivatives such as PM6:BTP-eC9 have a strong foothold in this field. Demonstrating high PCEs, the material system has excellent charge carrier transport for an organic material system. This is what makes this material system attractive for OPV. However, with a smaller optical bandgap, PM6:Y6 does not make as close a spectral match to the typical indoor LED spectrum as the material systems mentioned above. This poses the question of interest in this Thesis, for IOPVs, does spectral matching or charge transport quality impact efficiency more? Therefore, in addition to the two previously mentioned systems (PBDB-T:EH-IDTBR and PM6:EH-IDTBR), PM6:BTP-eC9 was also used to act as a comparison between the previous wide gap material systems to this narrower gap system.

3. INDOOR THERMODYNAMIC THEORETICAL LIMIT

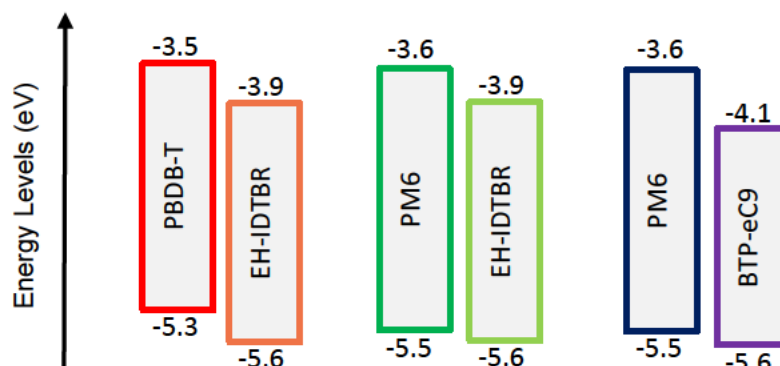


Figure 3.8: A schematic representation of the energy levels (eV) of three OPV material systems chosen for this work. From left to right: PBDB-T:EH-IDTBR, PM6:EH-IDTBR and PM6:BTP-eC9. The energy bandgap of all three materials systems are 1.40 eV, 1.60 eV and 1.40 eV respectively. Chemical structures as seen in Figure 1.7.

Chemical structures of all organic semiconductors can be referenced in Figure 1.7.

3.5 Summary

Through the generation of several simulations presented in this chapter, a few notable conclusions have been drawn. Through the adaptation of the classic SQ limit, two competing LED spectra for the standard testing protocol were used in place of the radiation source. This analysis produced radiative theoretical upper limit values of PCE for these environments and their related optimal energy bandgaps. This analysis was further improved using models of non-radiative models which used currently published research as a data starting point. As a result, this chapter produced two theoretical upper limits for IPV efficiency for the specified artificial light sources. This defined analysis forms a basis

3. INDOOR THERMODYNAMIC THEORETICAL LIMIT

to measure characterisation of IPVs against, eliminating any glaringly high values of claimed efficiency.

In addition to the successful analysis of the theoretical upper limit of efficiency, existing EQE_{PV} data (within the Sêr SAM group) was harnessed with the SQ calculations to predict the most thermodynamically appropriate active layer material systems for IPV application. This analysis defined the material systems chosen to investigate in this Thesis and so was a significant milestone within this research. Moving forward, these material systems will be tested on a homemade IPV simulator setup for characterisation with intensity dependent measurements investigating the associated losses previously explained in this chapter. *Chapter 4* will explore the results of the intensity dependent calculations, discussing and drawing conclusions of the importance of thermodynamic compatibility.

Chapter 4

Experimental Methodology and Results

In this chapter, solar and indoor characterisations of the three chosen material systems (PBDB-T:EH-IDTBR, PM6:EH-IDTBR, and PM6:BTP-eC9) will be presented. The relationship between thermodynamic compatibility and IPV performance, described in previous chapters, will be analysed and measured values of J_{SC} , V_{OC} , FF and PCE will be compared with radiative and non-radiative theoretical predictions at several illuminances.

4.1 Solar Cell Characterisation

A solar cell characterisation set-up was used to measure the light characteristics of the devices made for testing under indoor conditions to determine the best-performing pixels. Furthermore, the effect of shunt resistance of the device-under-test, R_{sh} on light intensity dependence of performance metrics is investigated. R_{sh} (or specific shunt resistance R_{sh}) is the inverse of the J - V slope under dark conditions, and therefore, it is measured from dark I - V curves in the work presented in this chapter. Measured values of specific R_{sh} were used in conjunction with indoor characteristics to analyse device performance under low light intensities in the following sections.

4. RESULTS AND DISCUSSION

4.1.1 Solar Cell Characterisation Set-up

A solar simulator is used to investigate the solar cell performance of the devices in this Thesis via a J - V sweep. The solar simulator is based on a Xenon lamp and an AM1.5 G filter, which is then calibrated using a KG5 filtered silicon reference cell.

A Keithley 2450 source-measure unit (SMU) was used to measure I - V characteristics of all devices in dark conditions (no illumination) with multiple data points being taken between the voltage values of -0.1 and 0.1 V; this allowed the identification of the gradient around the zero potential point – resulting in a good estimation of shunt resistance. This SMU was used as it can measure current to nano amp precision and so produced accurate readings around the open circuit condition to reduce potential errors. This was used for the dark measurements as precision was more important in these measurements due to very low values.

4.1.2 Shunt Resistance Results

To find the value of R_{sh} a set of data was collected for each device around the zero applied potential point. Around this point, the inverse slope of I - V determines the value of R_{sh} in the PV devices under test.

4. RESULTS AND DISCUSSION

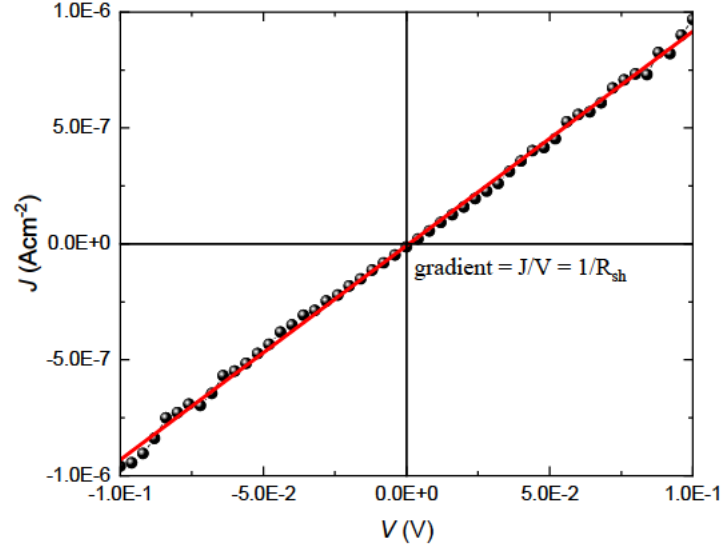


Figure 4.1: J - V characteristic (with no excess illumination) of PBDB-T:EH-IDTBR device of cell area 0.9482cm^2 . Experimental data and a linear fit are represented by the black circles and red solid line respectively.

The inverse linear fittings of each J - V characteristic is then interpreted as the specific shunt resistance of the device cell with units Ωcm^2 due to the area consideration in J - V characterisation versus I - V . Therefore, due to use of J - V curves in the remainder of this Thesis, specific shunt resistance will be represented by R_{sh} .

| | Device R_{sh} ($\text{M}\Omega\text{cm}^2$) | | | |
|-----------------|--|-------------------|-------------------|-------------------|
| | 0.04cm^2 | 0.14cm^2 | 0.39cm^2 | 0.95cm^2 |
| PBDB-T:EH-IDTBR | 5.36 | 4.71 | 0.24 | 3.89 |
| PM6:EH-IDTBR | 5.27 | 0.26 | 0.26 | 0.05 |

Table 3: The shunt resistances of two material systems, PBDB-T:EH-IDTBR and PM6:EH-IDTBR, with device sizes 0.04 , 0.1416 , 0.3894 and 0.9482 cm^2 .

From the values of R_{sh} measured for each device, using the theory from *chapter 3.3.1*, a prediction of optimal device performance under indoor illumination can be determined. Using the aforementioned theory, devices with higher R_{sh} should perform better under low

4. RESULTS AND DISCUSSION

light conditions; therefore, both 0.04 cm^2 pixel devices should perform best out of the devices under test.

4.2 Indoor Photovoltaic Characterisation

Device characterisations under simulated indoor conditions are used within this chapter and Thesis to demonstrate the light dependence on parameters J_{SC} , V_{OC} , FF , and ultimately PCE. Intensity dependence is an important consideration in the development of IPV. This is because indoor light sources typically provide illuminances much lower than those found outdoors, and with greater variation. As there is no set standard illumination to benchmark currently – unlike for solar simulators – as IPV is being developed a range of illuminances can be measured. As discussed in *chapter 3.3.1*, R_{sh} is an important determining factor in PCE performance at lower incident illuminances; this is demonstrated in the following sections through indoor characterisation.

4.2.1 Chosen Light Source

As previously mentioned, currently there is no standardised light spectrum source for IPV device characterisation. During the development of the Sêr SAM group's indoor characterisation set-up, a representative spectrum was ascertained in conversations with the National Physical Laboratory (NPL). This aids the research in this Thesis to remain as relevant as possible to the IPV industry as a light standard is developed in the future. The suggested light source standard was a 4000 K LED with collimated beam. The specification

4. RESULTS AND DISCUSSION

of the LED used for the IPV characterisations in this Thesis can be found in the following set-up description. It should be noted that while diffused light is more relevant to actual operation of IPV devices, it is more difficult to quantify the exact illuminance of diffused light. Therefore, a collimated beam was used.

4.2.2 Indoor Photovoltaic Characterisation Set-up

Following on from discussions with NPL, a light source similar to the standard LED-B4 spectrum, the international commission on illumination's (CIE's) standard illuminant LED-B4, was selected for use. Featuring variable output power control (in continuous wave mode) and LED stabilisation, a 4000 K LED light source was chosen (Prizmatix, UHP-T-LED-White). This LED's illuminance value of 1000 lux can be referenced from Table 1.

Important in the characterisation of IPV devices, the variability in irradiances of one environment causes edge cases to become relatively wide; therefore, a large range of irradiances should be considered in characterisation. To achieve the desired irradiances a motorised attenuator (Standa, 10MVAA) was used to attenuate the output of the LED. Through the combination of variable LED power control and attenuation, a large range of irradiances was attained. The light source is then parallelised as the LED is passed through a collimator. The test device is then placed vertically below the collimator far enough away to ensure an incident homogenous beam.

4. RESULTS AND DISCUSSION

In calibrating the IPV characterisation system, a NIST-calibrated lux meter (Digi-Sense, Model 20250-00) and a Si photodiode of known responsivity (Thorlabs, FDS1010) verified the illuminance at the device under test (DUT) location. Finally, it should be noted that a custom-made LabVIEW programme was used to operate the testing and calibration described above.

4.2.3 Intensity Dependence Results and Discussion

Taking advantage of the IPV characterisation set-up created by members of the Sêr SAM research group, intensity-dependent measurements of the three chosen material system devices were taken. J - V measurements were taken across intensities of approximately 4.5 orders of magnitude, producing an intensity-dependent graphical analysis of three parameters (J_{SC} , V_{OC} , and FF) and the overall performance of the figure of merit, PCE.

4. RESULTS AND DISCUSSION

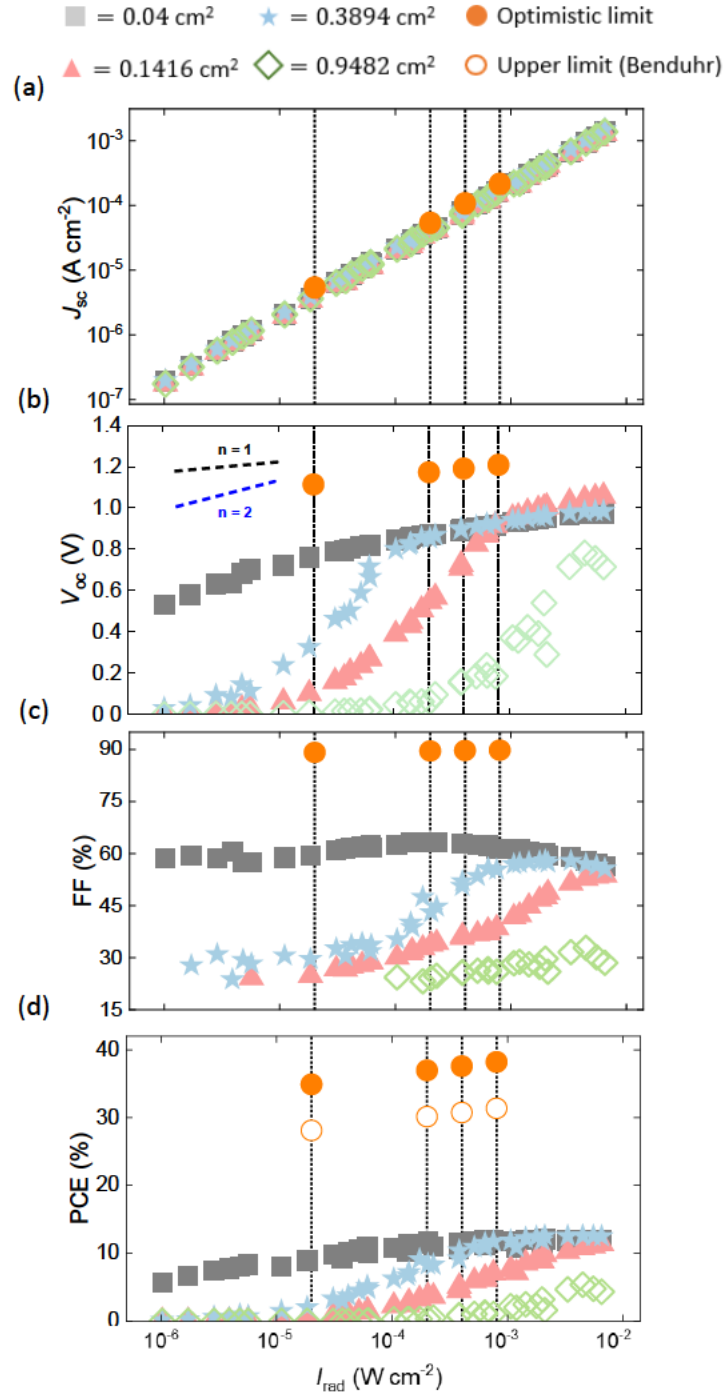


Figure 4.2: Intensity-dependent data of the PM6:EH-IDTBR material system PV device sample, with varying sizes pixels of 0.04, 0.1416, 0.3894, and 0.9482 cm² depicted by grey squares, pink triangles, blue stars and green diamonds respectively. Solid orange circles show the optimistic

4. RESULTS AND DISCUSSION

radiative detailed balance limit and the hollow orange circles show the Bendhur lower theoretical limit. The intensity axis is log scaled and the vertical dashed lines from left to right respectively showcase illuminance values of 50, 500, 1000, and 2000 lux. Various parameters are displayed (a) J_{SC} (b) V_{OC} (c) FF and (d) PCE. In panel (b), two dashed lines, black and blue, signify slopes of ideality factor (n) 1 and 2 respectively.

Through indoor characterisation graphical analysis, as shown in Figure 4.2, the dependence of R_{sh} is portrayed through pixels of varying areas and therefore shunts. Light intensity-dependent measurements of V_{OC} are of particular interest as they can often be used to determine the nature of recombination, with bimolecular recombination displaying as a slope of $n = 1$, and trap-assisted recombination resulting in a slope greater than this. When analysing the V_{OC} intensity-dependent measurements, the linear versus non-linear regime is more easily observable. In theory, when R_{sh} is high enough, the R_{sh} reduction will be negligible; this is not a significant issue in solar cell physics. At higher light intensities photocurrent (I_{ph}) is at least one order of magnitude higher than the leakage current (I_{sh}) – where I_{sh} is inversely proportional to R_{sh} ; therefore, the light current dominates favourably.

However, under low light intensities – typical of indoor environments – the opposite case presents itself. Using the n key on panel (b) in Figure 4.2, the pixel of area 0.04 cm^2 can be seen to change from an n of 1 to 2 approximately around the 250 lux illuminance mark as opposed to the device performing just under this experiencing the change in n at approximately 1000 lux. The remaining two lesser-performing devices experience this change at higher illuminances in these measurements with their linear trend of light intensity on V_{OC} beginning at higher intensities.

4. RESULTS AND DISCUSSION

In addition to this, as seen in Figure 4.2, the effect of a decrease in R_{sh} is large, this is because I_{ph} is now below one order of magnitude out from I_{sh} and so light current is significantly affected. The effect of this low R_{sh} and high I_{sh} will exhibit in an increased V_{OC} slope. For example, as predicted the 0.04 cm^2 pixel size, having the largest R_{sh} , outperforms the remaining devices at lower intensities. This can be seen in the illuminance markers signified on the graphs with dashed lines. While the regime remains linear for the other pixel sizes at illuminances of 500, 1000 and 2000 lux, the 0.04 cm^2 pixel still behaves in a linear regime past the 50 lux illuminance marker. In a system experiencing exclusively bimolecular recombination, this will then appear to have slopes mimicking trap-assisted recombination characteristics. From this figure, it is evident that the devices with a lower R_{sh} are increasing in slope at higher intensities and therefore, R_{sh} is significantly affecting the light intensity-dependent measurements of V_{OC} .

The solid orange circular key noted on each graph displays the theoretical optimistic radiative limits (calculation based on *chapter 2*, equations 2.6 - 2.14). This can be seen to linearly decline therefore illustrating the linear regime when neglecting the effect of R_{sh} , which can be seen best with the lesser performing devices, particularly where the separation between measured data and theoretical value increases non-linearly. As seen in Figure 4.2 panel (a), the J_{SC} experimental results are following the same trend and approximately the same value as the optimistic radiative limit. Therefore, from this, it is deducible that J_{SC} is not affected by R_{sh} in the way other PV parameters are. For instance, as observed from panels (b), (c), and (d), the effects of R_{sh} are more evident. In addition to this, the optimistic

4. RESULTS AND DISCUSSION

radiative limit sits further away from the experimental data. The same measurements and analysis were then performed on the PBDB-T:EH-IDTBR devices.

4. RESULTS AND DISCUSSION

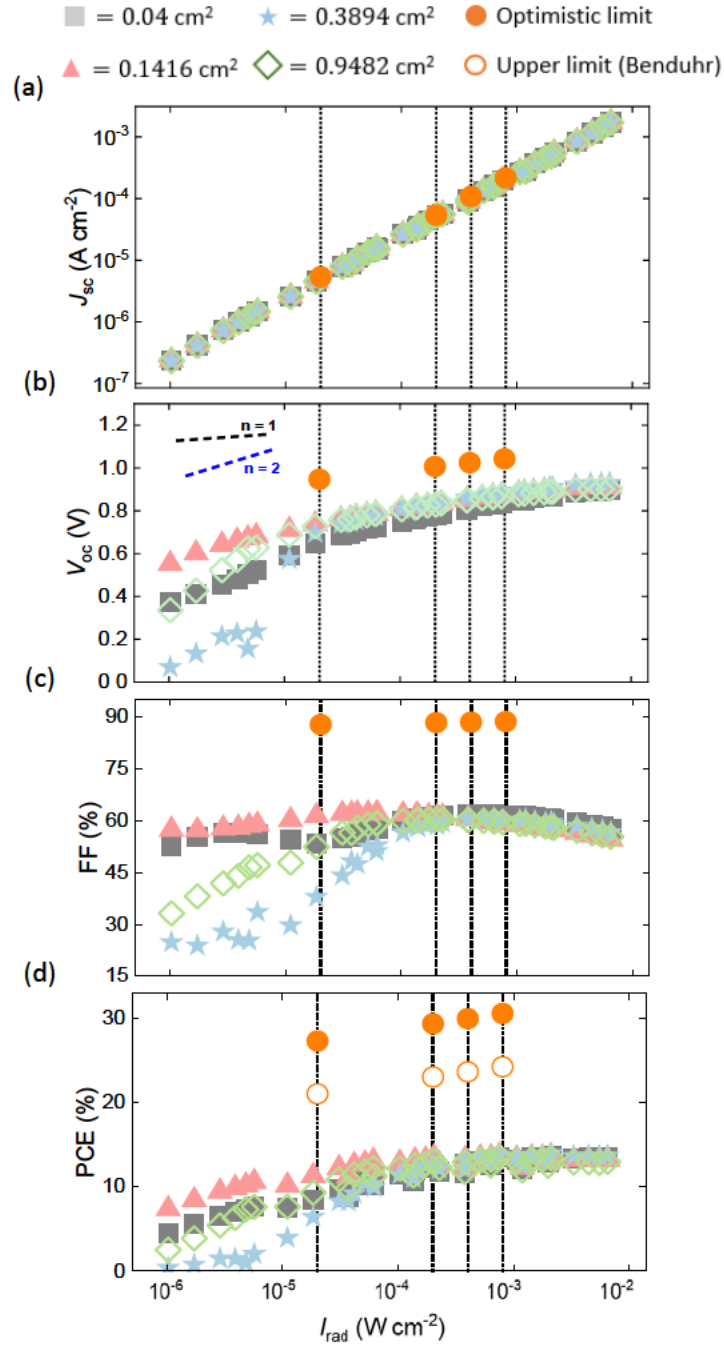


Figure 4.3: Intensity-dependent data of the PBDB-T:EH-IDTBR material system PV device sample, with varying sizes pixels of 0.04, 0.1416, 0.3894, and 0.9482 cm² depicted by grey squares, pink triangles, blue stars and green diamonds respectively. Solid orange circles show the optimistic radiative detailed balance limit and the hollow orange circles show the Bendhur lower theoretical

4. RESULTS AND DISCUSSION

limit. The intensity axis is log scaled and the vertical dashed lines from left to right respectively showcase illuminance values of 50, 500, 1000, and 2000 lux. Various parameters are displayed (a) J_{sc} (b) V_{oc} (c) FF and (d) PCE. In panel (b), two dashed lines, black and blue, signify slopes of ideality factor (n) 1 and 2 respectively.

In Figure 4.3, it is apparent that the PBDB-T:EH-IDTBR devices, when compared to the PM6-based devices in Figure 4.3, performed better under the simulated indoor illumination. Observing both panels (d) in each figure shows a higher achieved PCE at an illuminance of 500 lux of around 2-3% in the PBDB-T based devices. Once again, the dependence of R_{sh} on V_{oc} is displayed in the above graphical analysis and it is noticeable that at 500 lux that the devices' n change is more consistent from slope 1 to 2 occurring at, and closely around, this illuminance as determined using the n key in panel (b). In reference to Table 3, the relationship between R_{sh} and light dependence on V_{oc} correlates as predicted, with the lowest shunt device producing a non-linear relationship at a higher intensity in comparison to the remaining devices.

In addition to this, the dependence of R_{sh} on FF can be observed from both panels (c) in Figures 4.2 and 4.3. In Table 3, it can be determined that the values of R_{sh} for the PBDB-T:EH-IDTBR devices are higher than that of the PM6:EH-IDTBR devices. This is apparent from the two different effects on the trends of light intensity dependence on FF for the PM6-based devices. In Figure 4.3, the two devices with the higher R_{sh} values have an increase of FF as the light intensity decreases initially, before a decrease thereafter. The remaining two low R_{sh} devices decrease in FF from illuminance values above that of 2000 lux, denoted by the dashed line furthest right. However, when compared with the

4. RESULTS AND DISCUSSION

PBDB-T based devices as seen above in Figure 4.2, all four devices with decreasing R_{sh} (although still high) have an increase in FF as light intensity decreases to approximately 1000 lux illuminance – as denoted by the second dashed line to the right. Therefore, in these devices, the I_{sh} is not causing as significant an effect on the FF . In conclusion, with the two higher shunt devices maintaining their FF at illuminances as low as 50 lux (the furthest left dashed line), this further exaggerates the importance of a high R_{sh} at lower light intensities and therefore, in IPV development.

It is also worth mentioning the relationship between light intensity and J_{sc} . As shown in Figures 4.2 and 4.3, all four devices in each material system – with a difference only in their values of R_{sh} – have identical dependence on the light intensity, this identically linear relationship demonstrates the lack of effect of I_{sh} on J_{sc} .

4. RESULTS AND DISCUSSION

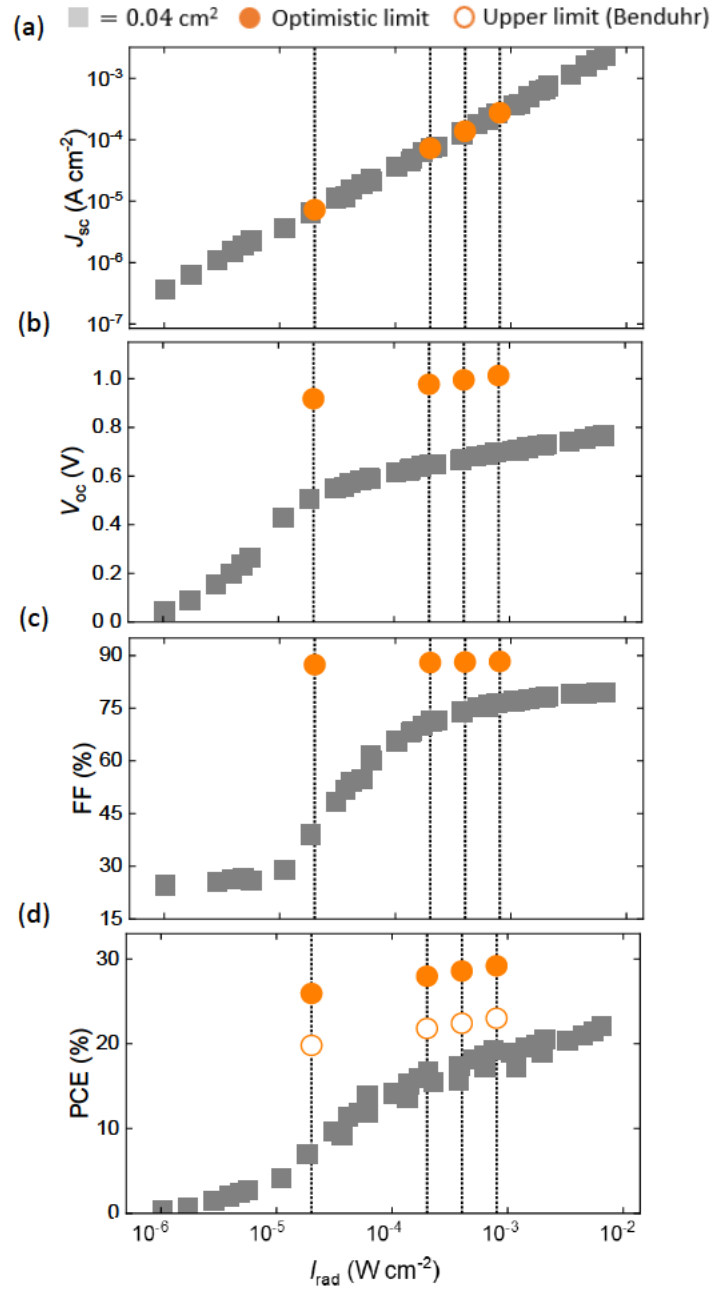


Figure 4.4: Intensity-dependent data of the PM6:BTP-eC9 material system PV device, pixel size 0.04 cm^2 depicted by grey squares. Solid orange circles show the optimistic radiative detailed balance limit and the hollow orange circles show the Bendhur lower theoretical limit. The intensity axis is log scaled and the vertical dashed lines from left to right respectively showcase illuminance

4. RESULTS AND DISCUSSION

values of 50, 500, 1000, and 2000 lux. Various parameters are displayed (a) J_{SC} (b) V_{OC} (c) FF and (d) PCE.

Following the format of analysis for the previous two material systems, PM6:BTP-eC9 shows a similar trend of all parameters to the previous systems. However, the PCE sits closer to the theoretically calculated limits. This could be due to many reasons, for example, the PM6:BTP-eC9 material system is more optimised compared to the new systems developed for this research. Despite the higher theoretical values for PBDB-T:EH-IDTBR PCE at lower illuminances, the device in Figure 4.4 reaches experimentally higher PCE.

One of the main points of research in this Thesis surrounded determining the compromise between thermodynamic compatibility and better charge transport in existing OSC material systems. As seen in Figure 4.4, the FF experienced by PM6:BTP-eC9 (representative of one of the best performing OPV systems at the time of writing this Thesis) is significantly higher (~15%) than the two best EH-IDTBR based devices (with better thermodynamic compatibility) in the range of illuminances greater than 500 lux. When considering the effect of charge transport on J - V characteristics, the relationship to FF is typically observed to be proportional. As the PM6:BTP-eC9 material system is known for good charge transport in OPVs, the higher FF observed in Figure 4.4, compared to the other intensity-dependent analyses, can be interpreted as a result of better charge transport of the material system.

Chapter 5

Conclusion

Indoor photovoltaics is a relatively new research field when compared to the well-established research presented over the past century in the physics of solar photovoltaics. Indoor photovoltaics present a difference in the light source from which energy is to be harvested. Whether the route to indoor photovoltaic development lies in the optimisation of existing well-performing solar photovoltaic material systems or the revisiting of material systems altogether, gauging these promising high power conversion efficiency systems through thermodynamic compatibility predictions, a considerable improvement is directly connected to the active layer material development. The discussion in this Thesis begins by utilising existing data (measured in the context of solar photovoltaic development) within the research group to determine favourable options for indoor performance analysis further on. In addition to the material choice, this indoor photovoltaic field calls for research into the loss mechanisms dominating the lower light intensity range. With indoor photovoltaics expecting to receive radiative intensity on orders of magnitude lower than that previously investigated for solar photovoltaic applications, the research into the possible differences in loss mechanisms explored in *chapter 4* should provide an insight into efficiency limiting factors.

From the indoor photovoltaic analysis presented in *chapter 4*, the final conclusions are as follows. The best-performing material system out of the two EH-IDTBR systems were the

5. CONCLUSION

PBDB-T devices, with the majority of the devices' light dependence on open-circuit voltage remaining linear towards the lower range of typical indoor light intensities. However, valuable insight is taken from the PM6:EH-IDTBR device analysis. In this set of measurements, the wider range of shunt resistances present obviously display the effects on the decrease in parameters of open-circuit voltage, fill factor, and ultimately PCE. In conclusion, a high ($>M\Omega$) shunt resistance is required for optimal device performance when exposed to low-intensity illumination. The PM6:EH-IDTBR material system's theoretical optimistic limit for power conversion efficiency is the highest out of the recorded systems. However, the model system, PM6:BTP-eC9, achieves the highest power conversion efficiencies due to its higher short-circuit current and recorded fill factors across the 500, 1000 and 2000 lux range.

Finally, a conclusion can be drawn on the significance of the compromise between thermodynamic compatibility and charge transport properties within a given material system for indoor photovoltaic development. From this research, it becomes apparent that while the model PM6:BTP-eC9 device outperforms the two novel EH-IDTBR based material system devices (selected based upon thermodynamic compatibility), these material systems have the potential to achieve higher power conversion efficiencies as development continues. As this Thesis included the use of non-radiative recombination loss empirical models, it can be used as a more accurate prediction of promising systems for indoor organic photovoltaic material choice.

5. CONCLUSION

Future research may benefit from improving on the possible developments this Thesis has shed light on. Optimisation of the EH-IDTBR based devices could see the efficiencies reaching closer to their lower empirical theoretical values, this would see the devices performing over that of the PM6:BTP-eC9 model system experimental results recorded in this Thesis. In developing devices that have a stronger innate thermodynamic compatibility, the improvement on parameters such as shunt resistance and properties such as charge transport can only see the enhancement of indoor photovoltaic devices in the future. Improvement in these areas could result in the implementation of indoor photovoltaic cells to power Internet of Things devices and ease their widespread expansion by reducing their reliance on battery power and therefore, maintenance. Through increasing the number of Internet of Things devices that can be deployed, positive applications such as their use in air pollution censoring and improving our understanding of agricultural growing climates improve the socio-economic quality of life of not exclusively industrial but also public sectors.

5. CONCLUSION

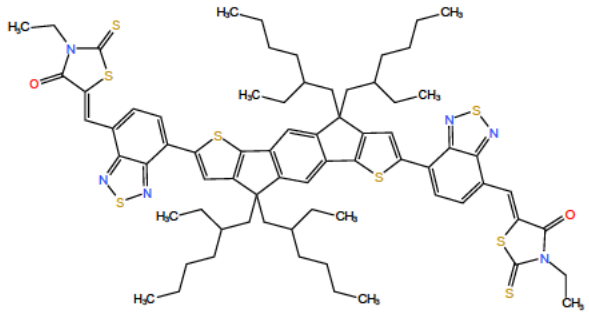
Appendix

Device Fabrication

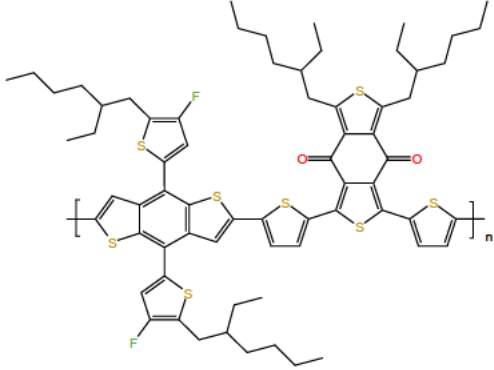
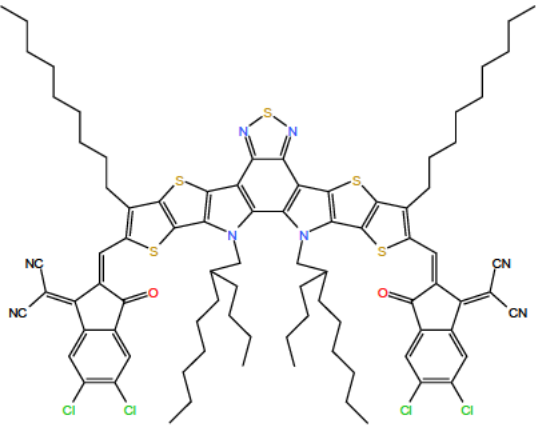
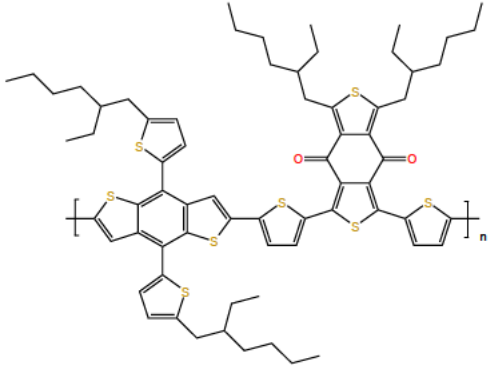
A.1 Materials

PEDOT:PSS (Poly(3,4-ethylenedioxythiophene)-poly(styrenesulfonate))

PDINO (perylene diimide functionalized with amino N-oxide)

| Name | Formula | Structure |
|-----------------|--|--|
| EH-IDTBR | <chem>CCN1C(=O)SC1=C/C=C2/C=C3/C=C4/C=C5C(=O)N(C)SC5=C4C(=O)N(C)SC4=C3C(=O)N(C)SC3=C2</chem> ((5Z)-3-ethyl-2-sulfanylidene-5-[[4-[9,9,18,18-tetrakis(2-ethylhexyl)-15-[7-[(Z)-(3-ethyl-4-oxo-2-sulfanylidene-1,3-thiazolidin-5-ylidene)methyl]-2,1,3-benzothiadiazol-4-yl]-5,14-dithiapentacyclo[10.6.0.03,10.04,8.013,17]octadeca-1(12),2,4(8),6,10,13(17),15-heptaen-6-yl]-2,1,3-benzothiadiazol-7-yl]methylidene]-1,3-thiazolidin-4-one) |  |

APPENDIX

| | | |
|-----------------------|--|--|
| <p>PM6</p> | <p>(Poly[(2,6-(4,8-bis(5-(2-ethylhexyl-3-fluoro)thiophen-2-yl)-benzo[1,2-b:4,5-b']dithiophene))- alt-(5,5-(1',3'-di-2-thienyl-5',7'-bis(2-ethylhexyl)benzo[1',2'-c:4',5'-c']dithiophene-4,8-dione))])</p> |  <p>The structure shows a polymer repeat unit with a central benzene ring. It is substituted with two dithiophene rings at the 1,2 and 4,5 positions. Each dithiophene ring has a 2-ethylhexyl group and a 3-fluoro group. The polymer chain is represented by brackets and a subscript 'n'.</p> |
| <p>BTP-eC9</p> | <p>2,2'- [[12,13-Bis(2-butyloctyl)-12,13-dihydro-3,9-dinonylbisthieno[2'',3'':4',5']thieno[2',3':4,5]pyrrolo[3,2-e:2',3'-g][2,1,3]benzothiadiazole-2,10-diyl]bis[methyldiyne(5,6-chloro-3-oxo-1H-indene-2,1(3H)-diylidene)]]bis[propanedinitrile]</p> |  <p>The structure shows a complex polymer repeat unit. It features a central benzothiadiazole core. This core is linked to two thieno[2,3:4,5]pyrrolo[3,2-e:2',3'-g] units. These units are further substituted with 2-butyloctyl and 3,9-dinonyl groups. The structure also includes methyldiyne and propanedinitrile groups, and a 5,6-chloro-3-oxo-1H-indene-2,1(3H)-diylidene moiety. The polymer chain is represented by brackets and a subscript 'n'.</p> |
| <p>PBDB-T</p> | <p>(Poly[(2,6-(4,8-bis(5-(2-ethylhexyl)thiophen-2-yl)-benzo[1,2-b:4,5-b']dithiophene))- alt-(5,5-(1',3'-di-2-thienyl-5',7'-bis(2-ethylhexyl)benzo[1',2'-c:4',5'-c']dithiophene-4,8-dione))])</p> |  <p>The structure shows a polymer repeat unit similar to PM6. It features a central benzene ring substituted with two dithiophene rings. Each dithiophene ring has a 2-ethylhexyl group. The polymer chain is represented by brackets and a subscript 'n'.</p> |

APPENDIX

A.2 Substrate Preparation

Sourced from Oscilla, commercially patterned indium tin oxide (ITO) coated glass substrates were used for all devices fabricated. Substrates were cleaned with an Alconox detergent (2% aqueous diluted) solution at 60°C and then sonicated in de-ionised (DI) water, acetone and 2-propanol respectively for 10 minutes each. The substrates were dried using Nitrogen and followed by Ultra-Violet treatment in the Ossila, L2002A2-UK cleaner.

A.3 Electron/Hole Transport Layer Deposition

Photovoltaic cells were fabricated in line with a conventional device architecture with PEDOT:PSS forming the hole transport layer. PEDOT:PSS was passed through a 0.45µm PVDF filter and then diluted 1:3 with DI water before being deposited on UV treated substrates at 6000RPM for 30 seconds (resulting in a thickness of 30nm). Finally, the substrates were then annealed at 155°C for 15 minutes.

A.4 Active Layer and Top Electrode Deposition

All devices' top electrodes were Silver (Ag) and thermally evaporated under a vacuum of 10^{-6} Tor. Evaporation masks were used to ensure pixel areas of 0.04cm², 0.1416cm², 0.3894cm² and 0.9482cm².

APPENDIX

PM6:EH-IDTBR - Devices were made in line with a conventional device architecture (ITO/PEDOT:PSS/PM6:EH-IDTBR/PDINO/Ag). PM6 and EH-IDTBR at a 1:1 ratio was combined with Chlorobenzene (CB) and 1,8-Diiodooctane (DIO) to form a solution of concentration of 30 mg mL^{-1} (content 99.5% and 0.5% respectively). The CB was added first and stirred at 45°C for 2 hours and then DIO was added before spin coating on the preprepared substrates at 2000RPM for 30 seconds to achieve a thickness of 100nm. Cast active layers were then annealed at 90°C for 10 minutes. 100nm of Ag was evaporated for the top electrode.

PBDB-T:EH-IDTBR - Devices were made in line with a conventional device architecture (ITO/PEDOT:PSS/PBDB-T:EH-IDTBR/PDINO/Ag). PBDB-T and EH-IDTBR at a 1:1 ratio was combined with Chlorobenzene (CB) and 1,8-Diiodooctane (DIO) to form a solution of concentration of 30 mg mL^{-1} (content 99.5% and 0.5% respectively). The CB was added first and stirred at 45°C for 2 hours and then DIO was added before spin coating on the preprepared substrates at 1500RPM for 60 seconds to achieve a thickness of 100nm. Cast active layers were then annealed at 90°C for 10 minutes. 100nm of Ag was evaporated for the top electrode.

PM6:IDIC - Devices were made in line with a conventional device architecture (ITO/PEDOT:PSS/PM6:IDIC/PDINO/Ag). PM6 and IDIC at a 1:1 ratio was combined with Chlorobenzene (CB) and 1,8-Diiodooctane (DIO) to form a solution of concentration of 30 mg mL^{-1} (content 99.5% and 0.5% respectively). The CB was added first and stirred at 45°C for 18 hours (overnight) and then DIO was added before spin coating on the

APPENDIX

preprepared substrates at 2000RPM for 30 seconds to achieve a thickness of 100nm. Cast active layers were then annealed at 90°C for 10 minutes. 100nm of Ag was evaporated for the top electrode.

PBDB-T:EH-IDTBR - Devices were made in line with a conventional device architecture (ITO/PEDOT:PSS/PBDB-T:IDIC/PDINO/Ag). PBDB-T and IDIC at a 1:1 ratio was combined with Chlorobenzene (CB) and 1,8-Diiodooctane (DIO) to form a solution of concentration of 30 mg mL⁻¹ (content 99.5% and 0.5% respectively). The CB was added first and stirred at 45°C for 18 hours (overnight) and then DIO was added before spin coating on the preprepared substrates at 2000RPM for 30 seconds to achieve a thickness of 100nm. Cast active layers were then annealed at 90°C for 10 minutes. 100nm of Ag was evaporated for the top electrode.

References

- [1] Benduhn et al., "Intrinsic non-radiative voltage losses in fullerene-based organic solar cells," *Nature Energy*, vol. 2, p. 17053, 2017.
- [2] M. Riede, D. Spoltore and K. Leo, "Organic Solar Cells - The Path to Commercial Success," *Advanced Energy Materials*, vol. 11, no. 1, p. 2002653, 2020.
- [3] H. Hoppe and N. S. Sariciftci, "Organic solar cells: An overview," *Journal of Materials Research*, vol. 19, pp. 1924-1945, 2004.
- [4] G. C. Righini and F. Enrichi, "Chapter One - Solar cells' evolution and perspectives: a short review," in *Solar Cells and Light Management - Materials, Strategies and Sustainability*, Elsevier, 2020, pp. 1-32.
- [5] N. Kumari, S. K. Singh and S. Kumar, "A comparative study of different materials used for solar photovoltaics technology," *Materials Today: Proceedings*, vol. 66, no. 8, pp. 3522-3528, 2022.
- [6] A. A. Abdulkadir and F. Al-Turjman, "Smart-grid and solar energy harvesting in the IoT era: An overview," *WILEY*, vol. Special Issue Paper, pp. 1-10, 2018.
- [7] R. Elghamry, H. Hassan and A. A. Hawwash, "A parametric study on the impact of integrating solar cell panel at building envelope on its power, energy consumption, comfort conditions, and CO₂ emissions," *Journal of Cleaner Production*, vol. 249, p. 119374, 2020.
- [8] R. Velik, "East-South-West Orientation of PV Systems and Neighbourhood Energy Exchange to Maximize Local Photovoltaics Energy Consumption," *INTERNATIONAL JOURNAL of RENEWABLE ENERGY RESEARCH*, vol. 4, no. 3, pp. 566-570, 2014.
- [9] C. Peng, Y. Huang and Z. Wu, "Building integrated photovoltaics (BIPV) in architectural design in China," *Energy and Buildings*, vol. 43, no. 12, pp. 3592-3598, 2011.
- [10] T. Ahmad and D. Zhang, "A critical review of comparative global historical energy consumption and future demand: The story told so far," *Energy Reports*, vol. 6, pp. 1973-1991, 2020.
- [11] M. D. Archer and R. Hill, *CLEAN ELECTRICITY FROM PHOTOVOLTAICS Series on Photoconversion of Solar Energy - Vol. 1*, London: Imperial College Press, 2001.

- [12] A. Goetzberger, J. Luther and G. Willeke, "Solar cells: past, present, future," *Solar Energy Materials and Solar Cells*, vol. 74, no. 1-4, pp. 1-11, 2002.
- [13] Heliatek; Whitepaper, "organic photovoltaics—truly green energy: ultra-low carbon footprint," 2020.
- [14] M. Krebs-Moberg, M. Pitz, T. L. Dorsette and S. H. Gheewala, "Third generation of photovoltaic panels: A life cycle assessment," *Renewable Energy*, vol. 164, pp. 556-565, 2021.
- [15] K. Orgil, "Comparison of Organic and Inorganic Solar Photovoltaic Systems," Electrical Engineering Department, California Polytechnic State University, San Luis Obispo, 2018.
- [16] B. Qu and S. R. Forrest, "Continuous roll-to-roll fabrication of organic photovoltaic cells via interconnected high-vacuum and low-pressure organic vapor phase deposition systems," *Applied Physics Letters*, vol. 113, p. 053302, 2018.
- [17] H. S. Ryu, S. Y. Park, T. H. Lee, J. Y. Kim and H. Y. Woo, "Recent progress in indoor organic photovoltaics," *Royal Society of Chemistry*, vol. 12, p. 5792, 2020.
- [18] Y. Cui, L. Hong and J. Hou, "Organic Photovoltaic Cells for Indoor Applications: Opportunities and Challenges," *ACS - Applied Materials and Interfaces*, vol. 12, pp. 38815-38828, 2020.
- [19] I. Mathews, S. N. Kantareddy, T. Buonassisi and I. M. Peters, "Technology and Market Perspective for Indoor Photovoltaic Cells," *Joule*, vol. 3, no. 6, pp. 1415-1426, 2019.
- [20] H. K. H. Lee, J. Wu, J. Barbe, S. M. Jain, S. Wood, E. M. Speller, Z. Li, F. A. Castro, J. R. Durrant and W. C. Tsoi, "Organic photovoltaic cells - promising indoor light harvesters for self-sustainable electronics," *Journal of Materials: Chemistry A*, vol. 6, no. 14, pp. 5618-5626, 2018.
- [21] S. X.-d.-S. a. K. E. Kyriakos Georgiou, "The IoT Energy Challenge: A Software Perspective," *IEEE EMBEDDED SYSTEM LETTERS*, vol. 10, no. 3, pp. 53-56, 2018.
- [22] C. Kittel, *Introduction to Solid State Physics*, 8th edition: John Wiley & Sons, 2005.
- [23] N. Marinova, S. Valero and J. L. Delgado, "Organic and perovskite solar cells: Working principles, materials and interfaces," *Journal of Colloid and Interface Science*, vol. 488, pp. 373-389, 2017.

- [24] D. Garratt, L. Misiekis, D. Wood and e. al., "Direct observation of ultrafast exciton localization in an organic semiconductor with soft X-ray transient absorption spectroscopy.," *Nature Communications*, vol. 13, no. 3414, 2022.
- [25] B. A. Gregg, "Excitonic Solar Cells," *J. Phys. Chem. B*, vol. 107, pp. 4688-4698, 2003.
- [26] C. Wang, Z. Zhang, S. Pejic, R. Li, M. Fukuto, L. Zhu and G. Sauve, "High Dielectric Constant Semiconducting Poly(3-alkylthiophene)s from Side Chain Modification with Polar Sulfinyl and Sulfonyl Groups," *MACROMOLECULES*, vol. 51, no. 22, p. 3, 2018.
- [27] X. Y. Zhu, Q. Yang and M. Muntwiler, "Charge-Transfer Excitons at Organic Semiconductor Surfaces and Interfaces," *Accounts of Chemical Research*, vol. 42, no. 11, pp. 1779-1787, 2009.
- [28] Z. Fu, X. Zhang, H. Zhang, Y. Li, H. Zhou and Y. Zhang, "On the Understandings of Dielectric Constant and Its Impacts on the Photovoltaic Efficiency in Organic Solar Cells," *Chinese Journal of Chemistry*, vol. 39, no. 2, pp. 381-390, 2020.
- [29] M. C. Scharbar and N. S. Sariciftci, "Efficiency of bulk heterojunction solar cells," *Progress in Polymer Science*, vol. 38, no. 12, pp. 1929-1940, 2013.
- [30] J. Chen, Y. Chen, L.-W. Feng, C. Gu, G. Li, N. Su, G. Wang, S. M. H. W. Swick, X. Guo, A. Facchetti and T. J. Marks, "Hole (donor) and electron (acceptor) transporting organic semiconductors for bulk-heterojunction solar cells," *EnergyChem*, vol. 2, no. 5, p. 100042, 2020.
- [31] G. Yu, J. Gao, J. C. Hummelen, F. Wudl and A. J. Heeger, "Polymer Photovoltaic Cells: Enhanced Efficiencies via a Network of Internal Donor-Acceptor Heterojunctions," *Science*, vol. 270, no. 5243, pp. 1789-1791, 1995.
- [32] N. S. Sariciftci, L. Smilowitz, A. J. Heeger and F. Wudl, "Photoinduced Electron Transfer from a Conducting Polymer to Buckminsterfullerene," *Science*, vol. 258, no. 5087, pp. 1474-1476, 1992.
- [33] S. Y. Park, C. Labanti, J. Luke, Y.-C. Chin and J.-S. Kim, "Organic Bilayer Photovoltaics For Efficient Indoor Light Harvesting," *Advanced Energy Materials*, vol. 12, no. 3, p. 2103237, 2021.
- [34] J. A. Hauch, P. Schilinsky, S. A. Choulis, S. Rajoelson and C. J. Brabec, "The impact of water vapour transmission rate on the lifetime of flexible polymer solar cells," *Applied Physics Letters*, vol. 93, p. 103306, 2008.

- [35] A. C. Olivieri and G. M. Escandar, "Chapter 6 - Analytical Figures of Merit," in *Practical Three-Way Calibration*, Elsevier, 2014, pp. 93-107.
- [36] B. Ehrler, E. Alarcón-Lladó, S. W. Tabernig, T. Veeken, E. C. Garnett and A. Polman, "Photovoltaics Reaching for the Shockley-Queisser Limit," *ACS Energy Letters*, vol. 5, no. 9, pp. 3029-3033, 2020.
- [37] A. G. Aberle, "Fabrication and characterisation of crystalline silicon thin-film materials for solar cells," *Thin Solid Films*, Vols. 511-512, pp. 26-34, 2006.
- [38] M. A. M. Al-Alwani, A. B. Mohamad, N. A. Ludin, A. A. Kadhum and K. Sopian, "Dye-sensitised solar cells: Development, structure, operation, principles, electron kinetics, characterisation, synthesis materials and natural photosensitisers," *Renewable and Sustainable Energy Reviews*, vol. 65, pp. 183-213, 2016.
- [39] S. Willis, "Advanced Optoelectronic Characterisation of Solar Cells," Dissertation, Oxford University, UK, 2011.
- [40] B. G. Streetman and S. Banerjee, *Solid State Electronic Devices*, 7th edition: Pearson, 2014.
- [41] Y. Zhang, I. D. W. Samuel, T. Wang and D. G. Lidzey, "Current Status of Outdoor Lifetime Testing of Organic Photovoltaics," *Advanced Science*, vol. 5, no. 8, p. 1800434, 2018.
- [42] S. M. Menke, N. A. Ran, G. C. Bazan and R. H. Friend, "Understanding Energy Loss in Organic Solar Cells: Toward a New Energy Regime," *Joule*, no. 2, pp. 25-35, 2018.
- [43] V. Pecunia, L. G. Occhipinti and R. L. Z. Hoye, "Emerging Indoor Photovoltaic Technologies for Sustainable Internet of Things," *Advanced Energy Materials*, vol. 11, no. 29, p. 2100698, 2021.
- [44] A. Venkateswararao, J. K. W. Ho, S. K. So, S.-W. Liu and K.-T. Wong, "Device characteristics and material developments of indoor photovoltaic devices," *Materials Science and Engineering: R: Reports*, vol. 139, p. 100517, 2020.
- [45] W. Shockley and H. Queisser, "Detailed balance limit of efficiency of p-n junction solar cells," *Journal of Applied Physics*, vol. 32, no. 3, pp. 510-519, 1961.
- [46] H. P. Lewis Fraas, *Solar Cells and Their Applications*, Hoboken, New Jersey: John Wiley & Sons Inc., 2010.
- [47] M. Wolf, *Proc. IRE*, vol. 48, p. 1246, 1960.

- [48] M. A. Green, K. Emery, Y. Hishikawa, W. Warta and E. D. Dunlop, "Prog. Photovoltaics," *Res. Appl*, vol. 22, p. 701, 2014.
- [49] T. Markvart, "Shockley: Queisser detailed balance limit after 60 years," *WIREs Energy and Environment*, vol. 11, no. 4, p. e430, 2022.
- [50] M. A. Green, "Solar Cell Efficiency Tables (Version 45)," *Progress in Photovoltaics: Research and Applications*, vol. 23, no. 1, pp. 1-9, 2015.
- [51] J. Nelson, *The Physics of Solar Cells*, Imperial College Press, 2003.
- [52] M. Wolf and H. S. Rauschenbach, "Thin Film Crystalline Silicon Solar Cells: Physics and Technology," *Wiley-VCH*, 2007.
- [53] M. A. Green, K. Emery, D. L. King, S. Igari and W. Warta, "Solar Cell Efficiency Tables (Version 25)," *PROGRESS IN PHOTOVOLTAICS: RESEARCH AND APPLICATIONS*, vol. 13, pp. 49-54, 2005.
- [54] M. A. Green, K. Emery, Y. Hishikawa and W. Warta, "Solar cell efficiency tables (version 36)," *PROGRESS IN PHOTOVOLTAICS: RESEARCH AND APPLICATIONS*, vol. 18, pp. 346-352, 2010.
- [55] M. A. Green, "Solar cell efficiency tables (version 49)," *PROGRESS IN PHOTOVOLTAICS: RESEARCH AND APPLICATIONS*, vol. 25, pp. 3-13, 2017.
- [56] M. A. Green, Y. Hishikawa, W. Warta, E. D. Dunlop, D. H. Levi, J. Hohl-Ebinger and A. W. Y. Ho-Baillie, "Solar cell efficiency tables (version 50)," *PROGRESS IN PHOTOVOLTAICS: RESEARCH AND APPLICATIONS*, vol. 25, pp. 668-676, 2017.
- [57] M. A. Green, K. Emery, Y. Hishikawa, W. Warta and E. D. Dunlop, "Solar cell efficiency tables (version 52)," *PROGRESS IN PHOTOVOLTAICS: RESEARCH AND APPLICATIONS*, vol. 26, pp. 427-436, 2018.
- [58] M. A. Green, E. D. Dunlop, J. Hohl-Ebinger, M. Yoshita, N. Kopidakis and X. Hao, "Solar cell efficiency tables (version 56)," *Progress in Photovoltaics: Research and Applications*, vol. 28, no. 7, pp. 629-638, 2020.
- [59] M. A. Green, E. D. Dunlop, J. Hohl-Ebinger, M. Yoshita, N. Kopidakis and X. Hao, "Solar cell efficiency tables (Version 58)," *Progress in Photovoltaics: Research and Applications*, vol. 29, pp. 657-667, 2021.

- [60] M. A. Green, E. D. Dunlop, J. Hohl-Ebinger, M. Yoshita, N. Kopidakis, K. Bothe, D. Hinken, M. Rauer and X. Hao, "Solar cell efficiency tables (Version 60)," *Progress in Photovoltaics: Research and Applications*, vol. 30, no. 7, pp. 687-701, 2022.
- [61] M. A. Green, E. D. Dunlop, G. Siefer, M. Yoshita, N. Kopidakis, K. Bothe and X. Hao, "Solar cell efficiency tables (Version 61)," *Progress in Photovoltaics: Research and Applications*, vol. 31, no. 1, pp. 3-16, 2022.
- [62] N. K. Tailer, M. Abdi-Jalebi, V. Gupta, H. Hu, M. Dar, G. Li and S. Satapathi, "Recent progress in morphology optimization in perovskite solar cell," *J. Mater. Chem. A*, vol. 8, pp. 21356-21386, 2020.
- [63] B. Ehrler, E. Alarcon-Llado, S. W. Tabernig, T. Veeken, E. C. Garnett and A. Polman, "Photovoltaics Reaching for the Shockley-Queisser Limit," *ACS Energy Letters*, vol. 5, pp. 3029-3033, 2020.
- [64] G. N. Lewis, "A New Principle of Equilibrium," *Proc. Nat. Acad. Sci.*, vol. 11, no. 179, 1925.
- [65] R. C. Tolman, "The Principle of Microscopic Reversibility," *Proc. Nat. Acad. Sci.*, vol. 11, no. 436, 1925.
- [66] O. E. Richardson, "The Hypothesis of the Unit Mechanism," *Proc. Roy. Soc. Lon.*, vol. 36, no. 392, 1924.
- [67] O. E. Lawrence, "The Principle of Detailed Balance," *Phys. Rev.*, vol. 27, no. 555, 1926.
- [68] T. Kirchartz, "Generalized detailed balance theory of solar cells," *Diplom-Ingenieur*, 2009.
- [69] A. Marti, J. L. Balenzategui and R. F. Reyna, "Photon recycling and Shockley's diode equation," *Journal of Applied Physics*, vol. 82, pp. 4067-4075, 1997.
- [70] C. D. Mathers, "Upper limit of efficiency for photovoltaic solar cells," *Journal of Applied Physics*, vol. 48, pp. 3181-3182, 1977.
- [71] G. L. Araujo and A. Marti, "Generalized detailed balance theory to calculate the maximum efficiency of solar cells," presented at the 11th E.C. Photovoltaic Solar Energy Conf., Montreux, Switzerland, 1992.
- [72] O. D. Miller and E. Yablonovitch, "The physics required to approach the Shockley-Queisser limit," presented at the 37th IEEE Photovoltaic Specialists Conf., Seattle, WA, USA, 2011.

- [73] O. D. Miller, E. Yablonovitch and S. Kurtz, "Strong internal and external luminescence as solar cells approach the Shockley-Queisser limit," *IEEE Journal of Photovoltaics*, vol. 2, no. 3, pp. 303-311, 2012.
- [74] M. A. Green, "Third generation photovoltaics: Ultra-high conversion efficiency at low cost," *Progr. Photovolt., Res. Appl.*, vol. 9, pp. 123-135, 2001.
- [75] A. Vossier, F. Gualdi, A. Dollet and e. al., "Approaching the Shockley-Queisser limit: General assessment of the main limiting mechanisms in photovoltaic cells," *Journal of Applied Physics*, vol. 117, p. 015102, 2015.
- [76] J. N. Munday, "The effect of bandgap materials on the Shockley-Queisser limit," *Journal of Applied Physics*, vol. 112, p. 064501, 2012.
- [77] D. Coles, "Standard Solar Spectrum," Ossila, [Online]. Available: <https://www.ossila.com/pages/standard-solar-spectrum>. [Accessed 8 January 2023].
- [78] C. A. Gueymard, "The sun's total and spectral irradiance for solar energy applications and solar radiation models," *Solar Energy*, vol. 76, no. 4, pp. 423-453, 2004.
- [79] S. Rühle, "Tabulated values of the Shockley-Queisser limit for single junction solar cells," *Solar Energy*, vol. 130, pp. 139-147, 2016.
- [80] C. Meier, A. Gondorf, S. Luttjohann and A. Lorke, "Silicon nanoparticles: Absorption, emission, and the nature of the electronic bandgap," *Journal of Applied Physics*, vol. 101, p. 103112, 2007.
- [81] Z. Wu, N. Li, N. Eedugurala and e. al., "Noise and detectivity limits in organic shortwave infrared photodiodes with low disorder.," *npj Flex Electron*, vol. 4, no. 6, 2020.
- [82] J. C. BERNÈDE, "ORGANIC PHOTOVOLTAIC CELLS: HISTORY, PRINCIPLE AND TECHNIQUES," *Journal of the Chilean Chemical Society*, vol. 53, no. 3, pp. 1549-1564, 2008.
- [83] A. Moliton and J. Nunzi, "How to model the behaviour of organic photovoltaic cells," *Polymer International*, vol. 55, no. 6, pp. 583-600, 2006.
- [84] Y. Zeng, D. Li, H. Wu, Z. Chen, S. Leng, T. Hao, S. Xiong, Q. Xue, Z. Ma, H. Zhu and Q. Bao, "Enhanced Charge Transport and Broad Absorption Enabling Record 18.13% Efficiency of PM6:Y6 Based Ternary Organic Photovoltaics with a High Fill Factor Over 80%," *Advanced Functional Materials*, vol. 32, no. 13, p. 2110743, 2021.

- [85] S. M. Hosseini, N. Tokmoldin, Y. W. Lee, Y. Zou, H. Y. Woo, D. Neher and S. Shoaee, "Putting Order into PM6:Y6 Solar Cells to Reduce the Langevin Recombination in 400 nm Thick Junction," *Solar RRL*, vol. 4, no. 11, p. 2000498, 2020.
- [86] S. M. Menke, N. A. Ran, G. C. Bazan and R. H. Friend, "Understanding Energy Loss in Organic Solar Cells: Toward a New Energy Regime," *Joule*, no. 2, pp. 25-35, 2018.
- [87] U. Rau, U. W. Paetzold and T. Kirchartz, "Thermodynamics of light management in photovoltaic devices," *Physical Review B*, vol. 90, p. 035211, 2014.
- [88] O. D. Miller, E. Yablonovitch and S. Kurtz, "Strong Internal and External Luminescence as Solar Cells Approach the Shockley–Queisser Limit," *IEEE JOURNAL OF PHOTOVOLTAICS*, vol. 2, no. 3, pp. 303-311, 2012.
- [89] U. Rau, "Reciprocity relation between photovoltaic quantum efficiency and electroluminescent emission of solar cells," *Physics Review B*, vol. 76, p. 085303, 2007.
- [90] M. Azzouzi, J. Yan, T. Kirchartz, K. Liu, J. Wang, H. Wu and J. Nelson, "Nonradiative Energy Losses in Bulk-Heterojunction Organic Photovoltaics," *Physical Review X*, vol. 8, no. 3, p. 031055, 2018.
- [91] S. Liu, J. Yuan, W. Deng, M. Luo, Y. Xie, Q. Liang, Y. Zou, Z. He, H. Wu and Y. Cao, "High-efficiency organic solar cells with low non-radiative recombination loss and low energetic disorder," *Nature Photonics*, vol. 14, pp. 300-305, 2020.
- [92] P. Cheng, G. Li, X. Zhan and Y. Yang, "Next-generation organic photovoltaics based on non-fullerene acceptors," *Natura Photonics*, vol. 12, no. 3, pp. 131-142, 2018.
- [93] M. Gruber, J. Wagner, K. Klein, U. Hörmann, A. Opitz, M. Stutzmann and W. Brütting, "Thermodynamic Efficiency Limit of Molecular Donor-Acceptor Solar Cells and its Application to Diindenoperylene/C60-Based Planar Heterojunction Devices," *Advanced Energy Materials*, vol. 2, no. 9, pp. 1100-1108, 2012.
- [94] J. Yao, T. Kirchartz, M. S. Vezié, M. A. Faist, W. Gong, Z. He, H. Wu, J. Troughton, T. Watson, D. Bryant and J. Nelson, "Quantifying Losses in Open-Circuit Voltage in Solution-Processable Solar Cells," *Physical Review Applied*, vol. 4, p. 014020, 2015.
- [95] S. Novikov, "Bimolecular Recombination of Charge Carriers in Polar Amorphous Organic Semiconductors: Effect of Spatial Correlation of the Random Energy Landscape," *J. Phys. Chem.*, vol. 122, p. 22856, 2018.

- [96] Burwell, O. J. Sandberg, W. Li, P. Meredith, M. Carnie and A. Armin, "Scaling Considerations for Organic Photovoltaics for Indoor Applications," *Solar RRL*, vol. 6, no. 7, p. 2200315, 2022.
- [97] H. Lee, Z. Li, J. Carrant and W. Tsoi, "Is organic photovoltaics promising for indoor applications," *Applied Physics Letters*, vol. 108, 2016.
- [98] A. Hande, T. Polk, W. Walker and D. Bhatia, "Indoor solar energy harvesting for sensor network router nodes," *Microprocess Microsyst*, vol. 31, no. 6, pp. 420-432, 2007.
- [99] A. Weddell, N. Harris and N. White, "An efficient indoor photovoltaic power harvesting system for energy aware wireless sensor nodes," *Pervasive Systems Centre, School of Electronics and Computer Science, University of Southampton, UK*, 2008.
- [100] A. Marszal, "Zero energy building - a review of definitions and calculation methodologies," *J Power Sources*, vol. 159, pp. 971-979, 2006.
- [101] "Energy STAR Building Manual: 10. Facility Type K-12 Schools," *Energy Star and Department of Energy*, 2006.
- [102] M. Muller, J. Wienold, W. Walker and L. Reindl, "Characterization of indoor photovoltaic devices and light," *Photovoltaic specialists conference (PVSC)*, 2009, 34th IEEE, Philadelphia.
- [103] J. Randall and J. Jacot, "Is AM1.5 applicable in practise? Modelling eight photovoltaic materials with respect to lght intensity and two spectra," *Renewable Energy*, vol. 28, no. 12, pp. 1851-1864, 2003.
- [104] M. A. Saeed, S. Cheng, S. Biswas, S. H. Kim, S. Kwon, H. Kim, Y. Kim and J. W. Shim, "Remarkably high performance of organic photovoltaic devices with 3,9-bis (2-methylene-(3-(1,1-dicyanomethylene)-indanone))-5,5,11,11-tetrakis (4-hexyl meta-phenyl)-dithieno[2,3-d:2' dithiophene]- ethylhexyloxy] photoactive acceptor under halogen light," *Journal of Power Sources*, vol. 518, p. 230782, 2022.
- [105] F. De Rossi, T. Pontecorvo and T. Brown, "Characterization of photovoltaic devices for indoor light harvesting and customization of flexible dye solar cells to deliver superior efficiency under artificial lighting," *Applied Energy*, vol. 156, pp. 413-422, 2015.
- [106] L. Ma, Y. Chen, P. C. Y. Chow, G. Zhang, J. Huang, C. Ma, J. Zhang, H. Yin, A. M. H. Cheung, K. S. Wong, S. K. So and H. Yan, "High-Efficiency Indoor Organic Photovoltaics with a Band-Aligned Interlayer," *Joule*, vol. 4, no. 7, pp. 1486-1500, 2020.

- [107] B. Li, B. Hou and G. A. J. Amaratunga, "Indoor photovoltaics, The Next Big Trend in solution-processed solar cells," *InfoMat*, vol. 3, no. 5, pp. 445-459, 2021.
- [108] D. L. Butler and P. M. Biner, "Preferred Lighting Levels: Variability among Settings, Behaviors, and Individuals," *Environment and Behaviour*, vol. 19, no. 6, pp. 695-721, 1987.
- [109] Y.-E. Wu and K.-C. Huang, "Smart Household Environment Illumination Dimming and Control," *Journal of Display Technology*, vol. 11, pp. 997-1004, 2015.
- [110] A.-T. Nedhal, F. S. F. Syed and A. Adel, "Relationship between Window-to-Floor Area Ratio and Single-Point Daylight Factor in Varied Residential Rooms in Malaysia," *Indian Journal of Science and Technology*, vol. 9, no. 33, pp. 1-8, 2016.
- [111] J. Balasus, J. Blank, S. Babilon, T. Hegemann and T. Q. Khanh, "Energy Efficient Lighting in Plant Factories: Addressing Utilance," *Agronomy*, vol. 11, no. 12, p. 2570, 2021.
- [112] C.-G. Yoon and H.-K. Choi, "A Study on the Various Light Source Radiation Conditions and use of LED Illumination for Plant Factory," *Journal of the Korean Institute of Illuminating and Electrical Installation Engineers*, vol. 25, no. 10, 2011.
- [113] J. Boyce, "Modern technologies for improving cleaning and disinfection of environmental surfaces in hospitals," *Antimicrob Resist Infect Control*, vol. 5, no. 10, 2016.
- [114] K. M. Eldaly, N. F. Zaki and L. S. E.-D. El-Gezawy, "Sustainability in the Choice of Architectural Elements Coloring and its Relation to Natural Light Intensity in Internal Spaces of Psychiatric and Neurological Hospitals.," *MEJ. Mansoura Engineering Journal*, vol. 41, no. 2, pp. 1-8, 2016.
- [115] D. Vethe, J. Scott, M. Engstrøm, Ø. Salvesen, T. Sand, A. Olsen, G. Morken, H. S. Heglum, K. Kjørstad, P. M. Faaland, C. L. Vestergaard, K. Langsrud and H. Kallestad, "The evening light environment in hospitals can be designed to produce less disruptive effects on the circadian system and improve sleep," *PMID: 32954412*, vol. 44, no. 3, 2021.
- [116] D. Trotsek, "Incorporation of therapeutic effect of daylight in the architectural design of in-patient rooms to reduce patient length of stay (LoS) in hospitals," *J Chem Inf Model*, vol. 110, no. 9, pp. 1689-1699, 2017.
- [117] H. Dalke, J. Little, E. Niemann, N. Camgoz, G. Steadman, S. Hill and L. Stott, "Colour and lighting in hospital design," *Optics & Laser Technology*, vol. 38, no. 4-6, pp. 343-365, 2006.
- [118] C. A. Reynaud, R. Clerc, P. B. Lechene, M. Hebert, A. Cazier and A. C. Arias, "Evaluation of indoor photovoltaic power production under directional and diffuse lighting conditions," *Solar Energy Materials and Solar Cells*, vol. 200, p. 110010, 2019.

- [119] Y. Cui, L. Hong, T. Zhang, H. Meng, H. Yan, F. Geo and J. Hou, "Accurate photovoltaic measurement of organic cells for indoor applications," *Joule*, vol. 5, no. 5, pp. 1016-1023, 2021.
- [120] E. F. Schubert, *Light-Emitting Diodes*, Cambridge University Press, 2003.
- [121] I. E. Commission, "Nanomanufacturing – Key control characteristics – Part 7-2: Nano-enabled photovoltaics – Device evaluation method for indoor light," International Electrotechnical Commission, 2023.
- [122] S. Biswas and H. Kim, "Solar Cells for Indoor Applications: Progress and Development," *Polymers*, vol. 12, no. 6, p. 1338, 2020.
- [123] J. Kosco, F. Moruzzi, B. Willner and I. McCulloch, "Photocatalysts Based on Organic Semiconductors with Tunable Energy Levels for Solar Fuel Applications," *Advanced Energy Materials*, vol. 10, no. 39, p. 2001935, 2020.
- [124] Y. Wang, F. Silveri, M. K. Bayazit, Q. Ruan, Y. Li, J. Xie, C. R. A. Catlow and J. Tang, "Bandgap Engineering of Organic Semiconductors for Highly Efficient Photocatalytic Water Splitting," *Advanced Energy Materials*, vol. 8, no. 24, p. 1801084, 2018.
- [125] M. Deru, N. Blair and P. Torcellini, "Procedure to Measure Indoor Lighting Energy Performance: NREL/TP-550-38602," National Renewable Energy Laboratory, 2005.
- [126] HSE Books, *Essentials of health and safety at work Guidance (Fourth edition)*, ISBN 978 0 7176 6179 4, 2006.
- [127] Z. Lucheng and S. Hui, "Novel approach for characterizing the specific shunt resistance caused by the penetration of the front contact through the p-n junction in solar cell," *J Semicond*, vol. 30, no. 7, 2009.
- [128] J. Zhao, X. Dai, M. Green and S. Wenham, "Improvements in silicon solar cell performance," *Photovoltaic specialists conference (PVSC), Las Vegas*, 1991.
- [129] J. Russo, W. Ray II and M. S. Litz, "Low light illumination study on commercially available homojunction photovoltaic cells," *Applied Energy*, vol. 191, pp. 10-21, 2017.
- [130] T.-Q. N. Christopher M. Proctor, "Effect of leakage current and shunt resistance on the light intensity dependence of organic solar cells," *Applied Physics Letters*, vol. 106, p. 083301, 2015.
- [131] A. Armin and a. et., "A History and Perspective of Non-Fullerene Electron Acceptors for Organic Solar Cells," *Advanced Energy Materials*, vol. 11, p. 20003570, 2021.

- [132] Ullbrich et al., "Emissive and charge-generating donor–acceptor interfaces for organic optoelectronics with low voltage losses," *Nature Materials*, vol. 18, pp. 459-464, 2019.
- [133] L. H. a. J. H. Yong Cui, "Organic Photovoltaic Cells for Indoor Applications: Opportunities and Challenges," *ACS - Applied Materials and Interfaces*, vol. 12, p. 38815–38828, 2020.
- [134] S. Philipps, F. Ise and W. Warmuth, "Photovoltaics Report," PSE Projects GmbH, 2020.
- [135] W. Zheng, S. Cui and X. Zhang, "The research of CaO/TiO₂ nanocrystalline film for dye-sensitized solar cell," in *2012 7th International Forum on Strategic Technology (IFOST)*, IEEE, 2012, pp. 1-4.
- [136] A. Nasiri, S. A. Zabalawi and G. Mandic, "Indoor Power Harvesting Using Photovoltaic Cells for Low-Power Applications," *EEE TRANSACTIONS ON INDUSTRIAL ELECTRONICS*, vol. 56, no. 11, p. 4502, 2009.
- [137] O, "Organic Photovoltaic Cells for Indoor Applications: Opportunities and Challenges," *ACS Advanced Materials and Interfaces*, vol. 12, no. 35, pp. 38815-38828, 2020.

